Title

Catch bond models may explain how force amplifies TCR signaling and antigen discrimination

Authors

Hyun-Kyu Choi[1,2], Kaitao Li[1,2], Peiwen Cong[1,2], Muaz Nik Rushdi[1,2,†], Chenghao Ge [1,2,‡], Wei Chen[3], Jizhong Lou[4-6], and Cheng Zhu[1,2,7,*]

Affiliations

[1]Wallace H. Coulter Department of Biomedical Engineering, Georgia Institute of Technology and Emory University, Atlanta, Georgia 30332, USA

[2]Parker H. Petit Institute for Bioengineering and Biosciences, Georgia Institute of Technology, Atlanta, Georgia 30332, USA

[3]Department of Cell Biology and Department of Cardiology of the Second Affiliated Hospital, Zhejiang University School of Medicine, Hangzhou 310058, China

[4]National Laboratory of Biomacromolecules, Institute of Biophysics, Chinese Academy of Sciences, Beijing 100101, China

[5]Key Laboratory of RNA Biology, CAS Center for Excellence in Biomacromolecules, Institute of Biophysics, Chinese Academy of Sciences, Beijing 100101, China

[6]University of the Chinese Academy of Sciences, Beijing 100049, China

[7]George W. Woodruff School of Mechanical Engineering, Georgia Institute of Technology, Atlanta, Georgia 30332, USA

[*]Corresponding Author: Cheng Zhu, Email: cheng.zhu@bme.gatech.edu

[†]Present address: Medtronic CO., Minneapolis, MN, USA

[‡]Present address: Amgen Inc., One Amgen Center Dr., Thousand Oaks, CA, USA

Abstract

Central to T cell biology, the T cell receptor (TCR) integrates forces in its triggering process upon interaction with peptide-major histocompatibility complex (pMHC)[1-3]. Phenotypically, forces elicit TCR catch-slip bonds with strong pMHCs but slip-only bonds with weak pMHCs[4-9]. While such correlation is generally observed, the quantitative bond pattern and degree of "catchiness" vary. We developed two models based on the structure, elastic properties, and force-induced conformational changes of the TCR–pMHC-I/II complexes to derive from their bond characteristics more intrinsic parameters that underlie structural mechanisms, predict T cell signaling, and discriminate antigens. Applying the models to all published 50 datasets of 11 TCRs and their mutants interacting with corresponding pMHCs without coreceptor engagement revealed the ability for structural and physical parameters to quantitatively integrate and classify a broad range of bond behaviors and biological activities. Comparing to the generic two-state model for catch-slip bond that also fits the data, our models can distinguish class I from class II MHC systems and their best-fit parameters correlate with the TCR/pMHC potency to trigger T cell activation, which the generic model cannot. The extensive comparisons between theory and experiment provided strong validation of the models and testable hypothesis regarding specific conformational changes that control bond profiles, thereby suggesting structural mechanisms for the inner workings of the TCR mechanosensing machinery and plausible explanation of why and how force amplifies TCR signaling and antigen discrimination.

47 **MAIN TEXT**

48

49 **Introduction**

50 Antigen recognition via TCR–pMHC interactions is essential for T cell activation,
51 differentiation, proliferation, and function[10]. Mechanical forces applied to TCR via engaged pMHC
52 substantially increase antigen sensitivity and amplify antigen discrimination[4-9,11]. As a fundamental
53 force-elicited characteristic, strong cognate pMHCs form catch-slip bonds with TCR where bond
54 lifetimes increase with force until reaching a peak, and decrease as force increases further, whereas
55 weak agonist and antagonist pMHCs form slip-only bonds with TCR where bond lifetimes decrease
56 monotonically with increasing force[4-9]. However, the mechanism underlying the correlation
57 between the force-lifetime pattern and the ability for force on TCR to induce T cell signaling
58 remains unclear.

59 An intuitive hypothesis is that catch bonds prolong interactions, which allow the process of
60 CD3 signal initiation to proceed sufficient number of phosphorylation steps to the threshold for
61 downstream signal propagation, as proposed by the kinetic proofreading model[12]. However, this
62 hypothesis faces two challenges upon scrutiny of multiple TCR–pMHC systems. First, since bond
63 lifetime *vs* force profiles are monotonically decreasing for slip-only bonds but bell-shaped for
64 catch-slip bonds, the type of bonds that would last longer depends on the force range, which may
65 be catch-slip bonds in one force regime but slip-only bonds in another force regime. Second, TCR–
66 pMHC interactions exhibiting catch-slip bonds often have longest lifetimes around 10-20 pN[4-8,13]
67 and it has been reported that upon engaging pMHC, T cells would exert 12-19 pN endogenous
68 forces on the TCR in a signaling-dependent fashion[14]. However, the relevance of this force range
69 to T cell signaling remains incompletely understood. More perplexingly, some signal-inducing
70 pMHCs form catch-slip bonds with TCRs but exhibit shorter lifetime than other pMHCs that do
71 not induce signaling by, and form slip-only bonds with, the same TCRs even in the optimal force
72 range[15]. These observations prompt the questions of what mechanism underlies the association of
73 TCR–pMHC bond type with the T cell signaling capacity and what impact this specific force range

has on TCR mechanotransduction. To answer these questions requires an in-depth analysis of the multiple datasets with mathematical models, which was lacking.

Slip and catch bonds refer to two opposite effects of physical force on biomolecular interactions: increasing or decreasing their off-rate of dissociation, respectively[16,17]. Because force tends to be disruptive and destabilizing, slip bonds are intuitive, whereas catch bonds are counter-intuitive. Since excessive force can rupture even covalent bonds[18], continued force increase will eventually overpower any catch bond, turning it to a slip bond after an "optimal" force where the off-rate is minimal[4-9,17]. Slip bond behavior is commonly modeled by the Bell equation, which assumes the dissociation rate k of a molecular bond along a single pathway in a one-dimensional (1D), single-well energy landscape to be an exponential function of force, $k(F) = k_0 e^{\frac{\delta_0^* F}{k_B T}}$. Here, k_0 is the transition rate at zero force, F is tensile force, δ_0^* is the force-free distance from the bound state at the bottom of the energy well to the top of the energy barrier known as the "transition state", k_B is the Boltzmann constant, and T absolute temperature[19]. Several models have been developed to account for catch-slip bond behavior. Most introduced two dissociation pathways and/or two bound states in a two-dimensional (2D) energy landscape that is tilted by force[20] (Fig. 1a). One noticeable exception is that of Guo et al. where dissociation is modeled to start from a single bound state along a single pathway through a 1D energy landscape based on the physical process of peeling a polymer strand with force until the transition state is reached[21]. A distinct advantage of this model is its ability to relate the force-induced tilting of the energy landscape to the force-induced conformational change of the molecular complex (which all other models lack), thereby connecting parameters of the abstract energy landscape to the structural-elastic properties of the interacting molecules.

Besides binding properties of the TCR–pMHC complex, its structural features and conformational changes have been suggested to be important for TCR triggering. For example, TCR–pMHC docking orientation has been correlated to its ability to trigger T cell signaling[15,22,23].

99 Partial unfolding or allosteric regulation of either the TCR and/or MHC molecules has been inferred
100 from mechanical experiments and steered molecular dynamics (SMD) simulations of pulling single
101 TCR–pMHC bonds[6,8,24,25]. Whereas the extent of these conformational changes has been correlated
102 to the strength of TCR–pMHC catch bonds[6,8,24], the two phenomena have not been integrated into
103 a mathematical model to explore their potential connection.

104 Here we developed two such models, one for each MHC class, to describe both TCR catch-
105 slip and slip-only bonds. The model development follows Kramers' kinetic rate theory and uses
106 polymer physics models to construct a 1D energy landscape for single-state, single-pathway
107 dissociation that incorporates the structures, elastic properties, and force-induced conformational
108 changes of the TCR–pMHC-I/II complexes at the sub-molecular level, which includes domain
109 stretching, hinge rotation, and molecular extension. Incorporating the force-induced conformational
110 changes into the energy landscape formulation allows force to shift the energy barrier up in low
111 forces and down in high forces, thereby giving rise to catch-slop bonds along a single dissociation
112 pathway in a 1D energy landscape (Fig. 1b). Applying the models to analyze all TCR–pMHC bond
113 lifetime *vs* force datasets published to date in 10 papers by four laboratories measured using two
114 different techniques[4-8,13,15,26-29], including 50 datasets of 11 TCRs and their mutants interacting with
115 corresponding panels of both classes of pMHCs without coreceptor engagement, revealed the
116 ability of our models' structural and physical parameters to quantitatively integrate and classify a
117 broad range of catch-slip or slip-only bond behaviors and biological activities. The extensive
118 comparisons between theory and experiment allowed us to rigorously validate the models by
119 systematically testing their assumptions, to identify specific conformational changes that control
120 the bond profiles, to provide mechanistic insights into the inner workings of the TCR–pMHC
121 mechanosensory machinery by constructing the energy landscape and investigating its properties,
122 and to understand how force-elicited catch bond amplifies TCR signaling and antigen

discrimination by examining the correlation of the model parameters with the biological activities of a large number of TCR–pMHC-I/II systems.

Results

Model development

Model goal: Kramers' kinetic rate theory treats bond dissociation as state transition in a 1D energy landscape $\Delta G^*(\delta_1)$ from a free-energy well (bound state) over a barrier (transition state) along the dissociation coordinate δ_1[30]. Following Guo et al.[21] to adapt the linear-cubic model of Dudko et al.[31] but allow force F to tilt the original energy landscape by an amount of $-\delta_1\gamma(F)$, the energy landscape takes the form of

$$\Delta G(\delta_1, F) = \frac{3\Delta G_0^*}{2}\left(\frac{\delta_1}{\delta_0^*} - \frac{1}{2}\right) - 2\Delta G_0^*\left(\frac{\delta_1}{\delta_0^*} - \frac{1}{2}\right)^3 - \delta_1\gamma(F)\ . \qquad (1)$$

where δ_0^* and ΔG_0^* are the differences in dissociation coordinates and free-energy levels, respectively, between the transition state and bound state of the original force-free energy landscape. The corresponding force-dependent kinetic rate is

$$k(F) = k_0\sqrt{1 - \frac{2\delta_0^*\gamma(F)}{3\Delta G_0^*}}\exp\left(\frac{\Delta G_0^*}{k_\mathrm{B}T}\left(1 - \left(1 - \frac{2\delta_0^*\gamma(F)}{3\Delta G_0^*}\right)^{3/2}\right)\right) \qquad (2)$$

where k_0 is the dissociation rate at zero force[21]. Letting $\gamma \sim F$ recovers from Eq. **2** the Dudko-Hummer-Szabo (DHS) model[31], and further assuming $|2\delta_0^*\gamma(F)/(3\Delta G_0^*)| \ll 1$ reduces it to the Bell model[19]. The condition for k to be able to model catch-slip bond is the derivative $k'(F_0) = 0$ where $F_0 > 0$. This translates to two conditions: the barrier height $\Delta G^* = \Delta G_0^*\left(1 - \frac{2\delta_0^*\gamma(F_0)}{3\Delta G_0^*}\right)^{3/2} = k_BT/3$ or $\gamma'(F_0) = 0$. The first condition requires the energy change $-\delta_1\gamma$ induced by F_0 to lower the energy barrier height to $k_\mathrm{B}T/3$ located at $\delta_0^*\left(\frac{k_BT}{2\Delta G_0^*}\right)^{1/3}$. The second condition requires γ to be a biphasic function of F. This excludes the Bell model and the DHS model because both of their γ functions depend on F monotonically. Our goal is to construct a biphasic $\gamma(F)$ with appropriate structural-elastic dependency to account for TCR–pMHC conformational changes from the bound

145 state to the transition state, as analyzed by the biomembrane force probe (BFP) experiments where
146 a tensile force is applied to its two ends to modulate bond dissociation[4-9].

147 *Key model assumptions*: Following the reasoning of Guo et al.[21], $\delta_l\gamma(F) = \int_0^F \delta_z(f)df$
148 where the integrand $\delta_z(f) = z(f) - z_0(f)$ is the projection on the force direction of the change
149 induced by force f of the TCR–pMHC extension at the transition state relative to its extension at
150 the bound state. For γ to depend on F biphasically as required for describing catch-slip bonds, δ_z
151 should be a biphasic function of f as discussed later. Therefore, dissociation occurs because the
152 system moves in the energy landscape along the dissociation coordinate δ_l from the bound state to
153 the transition state by a distance $\delta^* = \delta_0^*\left(1 - \frac{2\delta_0^*\gamma(F)}{3\Delta G_0^*}\right)^{1/2}$ [21]. We assume that the differential
154 contour length along the force transmission path across the TCR–pMHC structure (*i.e.*, summing
155 up all contour lengths of various domains connected at nodes of force action, as depicted in red
156 lines in Fig. 2a, for MHC-I) at the transition state l and bound state l_0 can serve as a dissociation
157 coordinate, i.e., $\delta_l = l - l_0$. δ_z is the projection of δ_l on the z axis – the direction of the pulling
158 force (Fig. 2a). When only contour lengths are considered, $\delta_l = \delta_0^*$, which serves as a criterion for
159 finding the best-fit parameters (Fig. 2a, *left* and Supplementary Model Derivations, Eq. S7).

160 Suggested by single-molecule optical tweezers[6], BFP[8] and magnetic tweezers[8] experiments
161 as well as steered MD (SMD) simulations[8], we assume that force-induced TCR–pMHC dissociation
162 is accompanied by conformational changes in both the TCR and MHC molecules. Specifically, we
163 assume that at the bound state, force induces elastic extension of the TCR–pMHC structure as a
164 whole (Fig. 2a, *left*); but as the system moves toward the transition state for dissociation,
165 conformational changes may occur, which may include disruption of intramolecular interfaces,
166 hinge rotation, and partial unfolding of interdomain joints (Fig. 2a, *right*). To include appropriate
167 details of these proposed conformational changes at the sub-molecular level into the expression of
168 δ_z, we model the TCR–pMHC structure as a system of semi-rigid bodies representing the whole
169 complex as well as various globular domains connected by semi-flexible polymers that allow

170 extension and hinge rotation under mechanical loads (Fig. 2a, *right*). Specifically, we assume that,
171 as the system moves along the dissociation pathway from the bound state toward the transition state,
172 force may induce disruption of the MHC $\alpha_1\alpha_2$–β_{2m} interdomain bond, thereby shifting the
173 mechanical load originally borne by this bond to the $\alpha_1\alpha_2$–α_3 joint to induce its partial unfolding,
174 as observed in SMD simulations[8]. As such, the MHC α_3 domain would change its length and rotate
175 about its C-terminus (Fig. 2b). Since the TCRβ subunit has also been proposed to undergo FG-
176 loop-regulated conformational change[6,24,25], we assume that disruption of the $\alpha_1\alpha_2$–β_{2m} joint would
177 also result in tilting of the TCR–pMHC bonding interface and shifting of the mechanical load from
178 the TCR Vβ–Cβ joint to the Vα–Cα joint, leading to partial unfolding of the Vα–Cα joint (Fig.
179 2b). This increased stretching of the Vα–Cα joint relative to the Vβ–Cβ joint is assumed to result
180 from strengthening of the Vβ–Cβ joint by the FG-loop[11]. At the transition state, therefore, we treat
181 the MHC α_3 domain ($d_{\alpha 3}$), the MHC $\alpha_1\alpha_2$ domains bound to the TCR Vαβ domains ($d_{\mathrm{B.I}}$), and the
182 TCR Cαβ domains ($d_{\mathrm{C}\alpha\beta}$) as three semi-rigid bodies connected by two unfolded peptide chains of
183 the MHC $\alpha_1\alpha_2$–α_3 joint ($d_{\mathrm{p,MHC}}$) and the TCR Vα–Cα joint ($d_{\mathrm{p,TCR}}$) (Fig. 2b, *right*). At the bound
184 state, neither disruption of intramolecular bonds nor partial unfolding of interdomain joints occurs,
185 as mentioned earlier, allowing the whole TCR–pMHC ectodomain complex to be modeled as one
186 semi-rigid body (d_{N}).

187 *Force-induced energy change:* To derive an expression for the last term on the right-hand
188 side of Eq. 1, we model the semi-rigid bodies d_{i} (i = N, α_3, B.I., and Cαβ to denote the whole TCR–
189 pMHC ectodomain structure as well as its indicated domains) as three-dimensional freely-jointed
190 chains (FJC) and employ polymer physics to obtain their force-extended length $d_{\mathrm{i}}(f)$ from their
191 force-free length $d_{\mathrm{i,c}}$[32] (Supplementary Model Derivations, Eq. S1).

192 The assumed partial unfolding of the $\alpha_1\alpha_2$–α_3 joint and the Vα–Cα joint is based on
193 suggestions from single-molecule optical tweezers[6], BFP[8] and magnetic tweezers[8] experiments as

194 well as SMD simulations[8]. We model these unstructured polypeptides as extensible worm-like
195 chains (eWLC) and employ polymer physics to obtain their force-induced extension $d_{\mathrm{p,i}}(f)$ (i =
196 MHC and TCR) from their force-free, folded state, which has zero length[33] (Supplementary Model
197 Derivations, Eq. S3).

198 Upon projecting the various force-induced extensions described above onto the force axis,
199 we obtain z components of five contributions to the TCR–pMHC length increase at the transition
200 state: extension of the MHC α_3 domain ($z_{\alpha 3}$), unfolding of the MHC $\alpha_1\alpha_2$–α_3 interdomain joint
201 ($z_{\mathrm{p,MHC}}$), extension of bonding interface that includes the MHC $\alpha_1\alpha_2$ domains bound to the TCR
202 Vαβ domains ($z_{\mathrm{B.I}}$), unfolding of the Vα–Cα joint ($z_{\mathrm{p,TCR}}$), and extension of the TCR Cαβ domains
203 ($z_{\mathrm{C\alpha\beta}}$) (Fig. 2b). Finally, we obtain:

$$\delta_{\mathrm{l}}\gamma(F) = \int_0^F \left[z_{\alpha 3}(f) + z_{\mathrm{p,MHC}}(f) + z_{\mathrm{B.I}}(f) + z_{\mathrm{p,TCR}}(f) + z_{\mathrm{C\alpha\beta}}(f) - z_{\mathrm{N}}(f)\right]df \qquad (3)$$

204 **Model characterization**

205 *Model constants and parameters:* The FJC model constants for the 1st, 3rd, 5th, and 6th terms
206 in the integrand on the right-hand side of Eq. 3 include the force-free lengths $d_{\mathrm{i,c}}$ and the elastic
207 modulus of the folded globular domain E_{c}, all of which are available from the literature. The 2nd
208 and 4th terms are proportional the respective numbers of amino acids in the polypeptides of the
209 partially unfolded MHC $\alpha_1\alpha_2$–α_3 joint ($n_{\mathrm{p,MHC}}$) and TCR Vα–Cα joint ($n_{\mathrm{p,TCR}}$), which can be
210 combined as the product of the total unfolded amino acid number $n^* = n_{\mathrm{p,MHC}} + n_{\mathrm{p,TCR}}$, the
211 average contour length per unfolded amino acid l_{c}, and the extension per unit contour length $z_{\mathrm{u,p}}(f)$.
212 The eWLC model constants for $z_{\mathrm{u,p}}(f)$ include the average persistence length per unfolded amino
213 acid l_{p} and the elastic modulus of polypeptides E_{p} (Supplementary Table 1).

214 After applying model constraints and the approximating $\Delta G_0^* \sim \ln(k_w/k_0)$ where k_w ~10^6 s^{-1}
215 is known as the prefactor (Supplementary Model Derivations), the model parameters are reduced
216 to 5: 3 structural parameters ($d_{\alpha 3}, \theta, n^*$) and 2 biophysical parameters (k_0, δ_0^*), for describing

217 dissociation of TCR–pMHC-I bonds. We will determine these parameters by comparing the model
218 predictions with experimental measurements, and by doing so, illustrate the ability of our model to
219 use a relatively low number of parameters to capture the coarse-grained structure and
220 conformational changes at the sub-molecular level during TCR–pMHC-I dissociation.

221 *Model features and properties:* To explore the general features and properties of the model,
222 we plotted δ_z vs F for two n^* values and a range of θ values as well as two θ values and a range of
223 n^* values (Fig. 2c). Conceptually, force-heightened energy barrier generates catch bonds and force-
224 lowered energy barrier produces slip bonds (Fig. 2d, *top left* and *right* panels). Since $-\delta_1\gamma$
225 represents the energy input by force F to the original energy landscape, a biphasic $\delta_1\gamma$ is required
226 to create catch-slip bonds (Fig. 2d, *top middle* panel); correspondingly, δ_z is required to have a root
227 at positive F where catch bond transitions to slip bond (Fig. 2c). The parameter domains capable
228 of generating catch, catch-slip, and slip bonds are mapped on an n^*-θ phase diagram (Fig. 2d),
229 showing that our model can describe catch-slop bond if and only if $n^* > 0$, $\theta > 0$, and $\delta_1\gamma(\infty) >$
230 0 (Fig. 2d, *top middle* panel). In other words, catch-slip bonds require partial unfolding of the MHC
231 $\alpha_1\alpha_2$–α_3 and/or TCR Vα–Cα joints and tilting of the TCR–pMHC bonding interface, a prediction
232 consistent with previous results of SMD simulations and single-molecule experiments[8].

233 For single-bond dissociation from a single bound state along a single pathway, the reciprocal
234 dissociation rate should equal to the average bond lifetime. Regardless of the bond type, the
235 reciprocal zero-force off-rate controls the *y*-intercept of the bond lifetime *vs* force curves. We
236 plotted the theoretical bond lifetime (normalized by its zero-force value) k_0/k *vs* force F for a
237 range of n^*, θ, and δ_0^* to examine how the model parameters control the bond lifetime *vs* force
238 profile (Fig. 2e). Consistent with Fig. 2c-d, only if $n^* > 0$ and $\theta > 0$ can our model describe catch-
239 slip bond. Increasing the tilting angle θ results in more pronounced catch-slip bonds with longer
240 lifetimes that peak at higher forces (Fig. 2e, *upper panel*). By comparison, increasing δ_0^* changes
241 the level of slip-only bonds if $n^* = 0$ and $\theta = 0$, but prolongs lifetime of catch-slip bonds (until

242 cross-over at a higher force) without changing the force where lifetime peaks if $n^* > 0$ and $\theta > 0$
243 (Fig. 2e, *lower panel*).

244 To understand physically how our model describes catch-slip bonds, we plotted the energy
245 landscape using Eq. 1 (Fig. 2f). Setting $\theta = 0$ in the upper panel generates a family of ΔG *vs* δ_1
246 curves where the energy barrier is suppressed monotonically with increasing force, indicating a
247 slip-only bond (Fig. 2f, *upper panel*). By comparison, setting $\theta > 0$ results in a family of ΔG *vs* δ_1
248 curves where the energy barrier height is initially raised, then lowered, by increasing force,
249 indicating a catch-slip bond (Fig. 2f, *lower panel*, also see Fig. 1b). We also examine how the
250 transition state location (Fig. 2g, *upper row*) and energy barrier height (Fig. 2g, *lower row*) change
251 with force for a range of θ and δ_0^* values that give rise to slip-only bonds and catch-slip bonds.
252 Noticeably, at fixed θ values, both rates by which the transition state location and the energy barrier
253 height change with force are accelerated by increasing δ_0^* (Fig. 2g, *right column*), suggesting that
254 this parameter can be used as a measure for force sensitivity. Interestingly, increasing θ slows the
255 decrease in both the transition state location and energy barrier height with force at higher values,
256 suggesting that the tilting angle controls the range at which force sensitivity can last (Fig. 2g, *left*
257 *column*).

258 **Model validation**

259 *Model's capability to fit data:* To test our model's validity, we used it to reanalyze data of
260 various TCRs forming catch-slip bonds and slip-only bonds with their respective panels of pMHCs.
261 These include three datasets published by us: 1) murine OT1 TCR expressed on either primary
262 naïve $CD8^+$ T cells or $CD4^+CD8^+$ thymocytes, which interacted with peptides presented by a mutant
263 (MT) MHC (H2-K^bα3A2) that abolished CD8 co-engagement[4,13] (Fig. 3a and Supplementary Fig.
264 1a); 2) wild-type (WT) or MT murine 2C TCRs either expressed on primary naïve $CD8^+$ T cells or
265 re-expressed on $CD8^-$ hybridoma cells, which interacted with peptides presented by H2-K^bα3A2
266 (for $CD8^+$ primary T cells) or H2-K^b (for $CD8^-$ hybridoma cells) to ensure no CD8 contribution

either way, or by H2-L^d(m31), a different MHC allele from H2-K^b (Fig. 3b, Supplementary Fig. 1b-c)[8]; and 3) WT and three MT human 1G4 TCRs were re-expressed on hybridoma cells, which interacted with the melanoma peptide NY-ESO-1 bound to HLA-A2 (Supplementary Fig. 1d)[8]. In addition, we fitted our model to two datasets published by other labs: 1) soluble mouse N15 TCRαβ interacted with VSV and two MT peptides bound to H2-K^b (Supplementary Fig. 1e)[6] and 2) four mouse TCRs expressed on hybridomas interacted with NP_{366} bound to the D227K mutant of H-2D^b to prevent CD8 binding[15] (Supplementary Fig. 1f). Gratifyingly, the theoretical reciprocal force-dependent off-rate $1/k(F)$ fits all 39 experimental bond lifetime *vs* force curves well (Fig. 3a-b, Supplementary Fig. 1, and Supplementary Table 2 and 3), demonstrating our model's capability to describe a wide range of data.

Characterization of force-lifetime relationship: Previous work reported qualitative correlations between the TCR bond type, *i.e.*, catch-slip bond *vs* slip-only bond, with the biological activity of the peptide to induce T cell activation, *i.e.*, pMHC potency[4,7-9,13]. To reduce data representation and extract more information quantitatively from the bond lifetime *vs* force data, we defined several metrics from their model fit for each TCR–pMHC system and examined their correlation with T cell activation induced by a given interaction, using the OT1 system as an example because the quantitative ligand potency data are available[4,34]. We measured the peak bond lifetime, t_{peak}, and the change, Δt, from t_{peak} to the force-free bond lifetime, $t_0 = 1/k_0$ (Fig. 3a, *left panel*). We found the relative metric Δt more suitable for comparison across different TCR systems, and better correlates with ligand potency, than the absolute counterpart t_{peak} (Fig. 3c). Although the force where catch-slip bond lifetime peaks, F_{opt}, occurs in a narrow range (10-20 pN), the force increment, ΔF, from F_{opt} to the level where bond lifetime returns to t_0 defines the force span of a catch-slip bond (Fig. 3a, *left panel*). One scaled parameter, $L = \Delta t/t_{\text{peak}}$ (relative length of lifetime), does (Fig. 3d, *left panel*), but the other, $B = \Delta F/F_{\text{opt}}$ (relative breadth of lifetime), does not (Supplementary Fig. 2a), correlate with ligand potency well. Remarkably, the combined

292 scaled parameter termed the catch bond intensity or catchiness, $I = L/(1 + B)$, correlates best with
293 the ligand potency across different TCR systems (Fig. 3d, *right panel* and 3e), supporting its
294 usefulness and reasonableness as a metric of reduced data representation for catch and slip bonds.

295 *Model parameters' correlation to ligand potency:* It seems reasonable to test the validity of
296 our model by examining the possible correlation of (or the lack thereof) the model parameters with
297 features of the biological system, e.g., the ligand potency. The rationale is that if its parameters are
298 capable of capturing and predicting such biological features, then the model would be more
299 meaningful and useful than merely a curve fitting tool. Therefore, we plotted the tilted angle of the
300 bonding interface θ, the number of the unfolded amino acids n^*, and the width of the zero-force
301 free-energy well δ_0^* that best-fit the force-lifetime curves of OT1, 2C, N15, TRBV TCRs interacting
302 with their corresponding panels of pMHCs (Fig. 3f). Gratifyingly, we observed good correlation
303 between each model parameter and the peptide potency for all published data of TCR–pMHC-I
304 catch-slip bonds and slip-only bonds from four independent laboratories[4,6,8,13,15].

305 In a previous study, we mutated residues in the 2C or 1G4 TCR and/or their corresponding
306 pMHCs to alter bond profiles as predicted by SMD simulations, which was confirmed by
307 experiment[8]. We therefore fitted our model to the force-lifetime curves of these mutant TCR–
308 pMHC bonds, which evaluated the best-fit model parameters, δ_0^* , θ , and n^* (Fig. 4a,
309 Supplementary Fig. 2b-c). In the absence of other functional data, we took an indirect approach to
310 examine their correlations with the catch bond intensity I of these bond lifetime *vs* force curve (Fig.
311 4b) since I and all three model parameters correlate with the peptide potency (Fig. 3e and f). Results
312 are exemplified by the δ_0^*, θ, and n^* *vs* I plots, which are graphed together with the data without
313 TCR and MHC mutations that already showed functional correlates. For the WT OT1, 2C, N15,
314 and TRBV TCRs interacting with their corresponding panels of pMHCs, δ_0^* (Fig. 4c), and to a lesser
315 extent, θ (Supplementary Fig. 2d) and n^* (Supplementary Fig. 2e), correlate with I that predicts
316 peptide potency (blue-open symbols). Remarkably, for the 2C and 1G4 TCRs specifically mutated

317 to alter bond profiles with the corresponding WT or mutant MHCs presenting the same agonist
318 peptide, their best-fit δ_0^*, and to a lesser extent, θ and n^*, also correlate well with I (Fig. 4c and
319 Supplementary Fig. 2d-e, green-closed symbols). Interestingly, $1/k_0$ shows a negative correlation
320 with I (Supplementary Fig. 2*f*), consistent with reports that zero-force bond lifetime does not
321 correspond to ligand potency in these cases[4,8,34].

322 It is worth pointing out that the above results not only support our model's validity but they
323 also suggest that our model is more than a mere analytical framework to organize experimental
324 data. Rather, the model parameters may be used to discriminate antigen and predict the force-
325 amplified discriminative power. For example, the correlations of θ and δ_0^* with peptide potency
326 (Figs. 3f and 4c) indicate that the more potent the peptide, the higher the force sensitivity of its
327 TCR–pMHC interaction, and the narrower the force range over which the TCR–pMHC interaction
328 is sensitive to force (Fig. 2g).

329 *Comparison between coarse-grained and all-atom models:* Bonding interface tilting has
330 been observed to be associated with changes in the number of hydrogen bonds bridging the TCR
331 and pMHC molecules as they were forced to unbind in SMD simulations[8]. Therefore, we
332 investigated whether, and if so, how well the tilting angle would correlate with the change of
333 hydrogen bonds between TCR and MHC. Remarkably, θ was found to be proportional to the net
334 change in the total number of hydrogen bonds at the bonding interface (Fig. 4d and Supplementary
335 Fig. 3). This finding is intuitive and supports the validity of our coarse-grained model because it is
336 able to recapitulate the results of all-atom SMD simulations[8].

337 *Classification of bond types by clustering analysis on phase diagrams:* In Fig. 2e-g we have
338 explored the model parameter space to identify regions that correspond to slip-only bonds and
339 catch-slip bonds. Here we examined whether, and if so, how parameters that best-fit different
340 experimental bond types map onto different regions of the parameter space. Since the model has
341 four parameters, θ, δ_0^*, $d_{\alpha 3}$, and n^* (k_0 is not considered because if its lack of correlation with catch

342 bond intensity), we analyzed their clustering and projected their values in the 4D parameter space
343 onto three phase diagrams spanning the θ-δ_0^* (Fig. 4e), θ-$d_{\alpha 3}$ (Figs. 4f and Supplementary Fig. 4),
344 and δ_0^*-n^* (Fig. 4g) 2D space. Clustering analysis of the model parameters that best-fit 36 published
345 TCR–pMHC bond lifetime *vs* force curves (Supplementary Fig. 5) shows three distinct clusters in
346 the δ_0^* *vs* θ and θ *vs* $d_{\alpha 3}$ plots as well as δ_0^* and θ *vs* n^* plots (Fig. 4e-g), which classify the TCR–
347 pMHC interactions into slip-only (SO), weak catch-slip (WC) and strong catch-slip (SC) bonds,
348 which correspond to weak, intermediate, and strong potencies for pathogenic peptides and their
349 variants. Whereas transition in bond type from SO to WC and SC requires monotonical increase in
350 θ and n^* (Fig. 4f, g), the corresponding change in δ_0^* is non-monotonic (Fig. 4e-g). SO bonds show
351 small n^*, δ_0^*, and θ values. WC and SC bonds observed from published experiments are best-fitted
352 by similar n^* (5 for WC and 7 for SC) but oppositely ranked δ_0^* and θ values. To change from WC
353 to SC bonds requires decreasing δ_0^* (from 2.7 to 1.9 nm) but increasing θ (from 14 to 32 °) (Fig.
354 4g). We also performed principal component analysis and calculated the Mahalanobis distances of
355 the principal axes for the three bond types[35], which are statistically separated in the catch bond
356 intensity *vs* Mahalanobis distance plot (Fig. 4h). Interestingly, WC and SC bonds show distinct
357 conformational changes despite their similar *I* values measured from the force-lifetime curves. The
358 corresponding structural features of these three types of bonds are depicted in Fig 4i, which have
359 been observed in our previous SMD studies[8]. Of note, model parameters visualized by SMD
360 simulations are usually larger than their best-fit values, which may have two explanations: First, to
361 enable dissociation to be observed in the affordable computational time, much higher forces were
362 used in simulations than experiments to accelerate the biophysical process, which likely induced
363 much larger conformational changes. Secondly, our model describes the average conformational

364 change during the entire dissociation process, which is smaller than the maximum conformational
365 changes likely to occur right before unbinding and to be captured by SMD.

366 *Our structure-based model is superior to the generic two-pathway model:* It seems that
367 other published catch bond models should also be able to fit the experimental force-lifetime profiles
368 analyzed here, given their relative simple shapes. As an example, we examined the two-pathway
369 model below[36]:

$$k(F) = k_{0,p1}e^{\delta^*_{0,p1}F/k_BT} + k_{0,p2}e^{\delta^*_{0,p2}F/k_BT} \quad (4)$$

370 where $k_{0,p1}$ and $k_{0,p2}$ are the respective zero-force off-rates of the first and second pathway, $\delta^*_{0,p1}$
371 and $\delta^*_{0,p2}$ are the respective distances from the bound state to the transition states along the first and
372 second pathway (Fig. 1a). Thus, the off-rate for each pathway takes the form of the Bell model, but
373 the catch pathway parameter $\delta^*_{0,p1}$ has a negative value[36] (Supplementary Table 4). This model is
374 generic as it has previously been applied to TCR–pMHC catch-slip bonds without considering the
375 specific conformational changes[6].

376 As expected, Eq. 4 also fitted our experimental data with goodness-of-fit measures
377 statistically indistinguishable to Eq. 2 (Supplementary Figs. 1 and 10a-b). However, the fitting
378 parameters correlate with neither the TCR/pMHC-I potency to induce T cell function nor the
379 intensity of catch bond (Supplementary Fig. 6, see the negative or zero correlation and the poor R^2
380 values), hence have no biological relevance. This comparison indicates that the model developed
381 herein is superior to the previous two-pathway model.

382 **Model for TCR catch bonds with class II pMHC**

383 MHC class II differs from class I in three main aspects (comparing Fig. 2a and Fig. 5a): (1)
384 MHC-I has three α domains and a β_{2m} domain whereas MHC-II has two α and two β domains. (2)
385 MHC-1 anchors to the T cell membrane through a single linker to the α_3 domain. The β_{2m} domain
386 attaches to the α_3 domain instead of anchoring to the T cell membrane directly. By comparison,
387 MHC-II anchors to the membrane through two linkers, one to the α_2 domain and the other to the β_2

388 domain. (3) The peptide is presented by the α_1-α_2 domains of MHC-I but the α_1-β_1 domains of
389 MHC-II. These structural differences alter how forces are supported by and transmitted through,
390 and induce conformational changes in, the TCR complexes with pMHC-I *vs* pMHC-II. Thus, it is
391 necessary to modify the previous model in order for it to describe TCR catch and slip bonds with
392 MHC-II, which is done by using a different $\delta_1\gamma(F)$ expression than Eq. 3 (Supplementary Model
393 Derivations, Section B). This modification assumes force-induced partial unfolding and stretching
394 of the TCR Vα-Cα joint and the MHC α_1-α_2 and β_1-β_2 joints during dissociation, which results in
395 tilting of the bonding interface (Fig. 5a, b).

396 In the class II model, the same parameters δ_0^*, n^*, and θ are used but the MHC contribution
397 to n^*, $i.e.$, $n_{\mathrm{p,MHC}}$, represents the average number of amino acids in the polypeptides of the partially
398 unfolded MHC-II α_1-α_2 and β_1-β_2 joints instead of the MHC-I $\alpha_1\alpha_2$–α_3 joint, and the relationships
399 between θ to other structural parameters are also different from the class I model (Fig. 5b and
400 Supplementary Model Derivation, Section B). Like the class I model, the k_0/k *vs* F plots for a
401 range of n^*, θ, and δ_0^* in Fig. 5c show similar features to Fig. 2e and meet our objective of being
402 capable of describing catch-slip bonds if and only if $n^* > 0$ and $\theta \geq 0$. Unlike the class I model, a
403 much smaller θ value (< 10°) is seen in the class II model (compared Fig. 5c and Supplementary
404 Fig. 7 with Fig. 2e-g), indicating the main conformational change responsible for TCR–pMHC-II
405 catch-slip bond is unfolding rather than tilting. The validity of this model is supported by its
406 excellent fitting to our published data of mouse WT or MT TCRs on naïve T cells (3.L2) or
407 hybridomas (2B4) interacting with their respective p:I-E^k ligands[5,28] (Fig. 5d, Supplementary Table
408 5 and 6). The four metrics of the TCR–pMHC-II bond lifetime *vs* force curves Δt, L, I, and t_{peak}
409 correlate well with the published peptide potency[37,38] (Fig. 5e and Supplementary Fig. 8). Since
410 mutations on the 2B4 TCR were designed to perturb its Cαβ interaction with the CD3 subunits,
411 their effect on the bond profile and T cell function might be weaker than the effects of the altered

412 peptide ligands for the 3.L2 TCR[5,28]. Nevertheless, the correlations between ligand potency and the
413 three model parameters θ, n^*, and δ_0^* for the 2B4 system are comparable to those for the 3.L2
414 system (Fig. 5f), supporting the ability of the metrics of the bond profile and the model parameters
415 to recognize the change in the TCR-CD3 ectodomain interaction in addition to the ability to
416 discriminate antigen. These properties are desirable, intuitive, and are consistent with the parallel
417 properties found in the class I model. Similar to the class I model parameters, δ_0^* correlates well
418 with the catch bond intensity for the pooled results from all published class II data (Fig. 5g, *left*),
419 but θ and n^* correlate less well with I (Fig. 5g, *middle and right*). Thus, the validity of the class II
420 model is further supported by the faithful mapping of the relationship between biophysical
421 measurements of catch and slip bonds and biological activities of the TCR–pMHC-II interactions
422 onto a relationship between model parameters and biological function.

423 As expected, Eq. 4 also fitted our experimental data with goodness-of-fit measures
424 statistically indistinguishable to Eq. 2 (Fig. 5d and Supplementary Fig. 10c-d). Similar to the case
425 of class I system, the fitting parameters correlate with neither the TCR/pMHC-II potency to induce
426 T cell function nor the intensity of catch bond (Supplementary Fig. 6, see the negative or zero
427 correlation and the poor R^2 values), hence have no biological relevance. This comparison again
428 indicates that the model developed herein is superior to the previous two-pathway model.

429 **Cross-examination of class I model against class II data and *vice versa***

430 Upon examining the catch-slip and slip-only bond lifetime *vs* force curves in Figs. 3a, 3b,
431 5d and Supplementary Fig. 1, it became apparent that the data seem very similar regardless of
432 whether they are for class I or class II pMHC. Indeed, applying the class I model to the class II data
433 and *vice versa* reveals that both models are capable of fitting both datasets well (Supplementary
434 Fig. 9) and produce statistically indistinguishable goodness-of-fit measures (Supplementary Fig.
435 10). This is not surprising because both models have five fitting parameters and the bond lifetime
436 *vs* force curves have relatively simple shapes. Nevertheless, fitting the same data by different

437 models returns different parameter values depending on the model used, because the two models
438 are constructed based on different structures and force-induced conformational changes of the
439 TCR–pMHC complexes. Therefore, we asked whether the best-fit model parameters were capable
440 of distinguishing data from the two classes of pMHCs and of telling whether a correct model was
441 used to analyze data of matched MHC class. To answer these questions, we plotted δ_0^* *vs* I (Fig. 6a,
442 b) and δ_0^* *vs* n^* (Fig. 6d, e) using values of the two models that best-fit the data of OT1, 2C, 1G4,
443 N15, and TRBV TCRs interacting with their respective panels pMHC-I ligands (Fig. 6a, d) as well
444 as 3.L2, 2B4, and E8 TCRs interacting with their respective panels of pMHC-II ligands (Fig. 6b,
445 e). Surprisingly, the dependency of δ_0^* on I is 2~3-fold stronger (i.e., steeper slope) (Fig. 6c),
446 indicating a greater discriminative power of ligand potency, for the matched than the mismatched
447 cases. Furthermore, it is well-known that the average contour length per a single amino acid l_c is ~
448 0.4 nm[21,39,40], which sets the biophysical limit for the slope of δ_0^* *vs* n^* plots. Indeed, we found that
449 the slopes of the δ_0^* *vs* n^* plots are within this limit for both model fits of the class I data (Fig. 6f).
450 For the class II data, the slope of the δ_0^* *vs* n^* plot reaches this limit for the matched case but exceeds
451 this limit for the mismatched case (Fig. 6f). Moreover, the goodness-of-fit (R^2) values of the linear
452 fit to the δ_0^* *vs* I (Fig. 6c) and δ_0^* *vs* n^* (Fig. 6f) data are much greater for the matched than the
453 mismatched cases, indicating more appropriate models for the data in the matched than the
454 mismatched cases. Indeed, the R^2 value for fitting the class I data by the class II model is too small
455 to be statistically reasonable, therefore telling the mismatch between the model and the data. These
456 results indicate that the model parameters are capable of distinguishing data from the two classes
457 of pMHCs.
458
459 **Discussion**

460 With the exception of a recent paper that observed T cell pulling on TCR by ~2 pN forces
461 using spider silk peptide-based force probe[41], five publications from two laboratories demonstrated
462 that TCR experienced endogenous forces of 12-19 pN using DNA-based force probes[13,14,42-44].

463 Also, except for a single paper that failed to observe catch bonds in the 1G4 TCRαβ ectodomain
464 using a flow chamber[45], extensive data in 10 papers from four laboratories have demonstrated catch
465 bonds in 11 membrane TCRs (including 1G4) using biomembrane force probe and optical
466 tweezers[4-8,13,15,26-28]. These experiments prompted us to develop two mathematical models for TCR
467 catch bonds, one with class I and the other with class II pMHC, based on Kramer's kinetic theory
468 and accounted for the 3D coarse-grained structures, molecular elasticity, and conformational
469 changes of the TCR–pMHC-I/II complexes. Previously, several models have been developed to
470 describe catch-slip bonds of selectins–ligands[36,46-48], integrins–ligands[49,50], platelet glycoprotein
471 Ibα–von Willebrand factor[51] cadherin–catenin[52], vinculin–actin[53], talin–actin[54] interactions. Except
472 for the sliding-rebinding model, which is based on force-induced conformational changes in P-
473 selectin–ligand observed from SMD simulations[48], none of these models have included any specific
474 structural considerations of the interacting molecules. Instead, these models are based on a generic
475 physical picture of dissociation along two pathways from either one or two bound states in a 2D
476 energy landscape that is tilted by force[20,55]. Except for the two-pathway model tested here, which
477 has 4 parameters[36], all other models have 5-10 parameters; therefore, over-fitting is a concern for
478 applying them to some of the datasets analyzed here. Although the two-pathway model is capable
479 of fitting the TCR–pMHC catch-slip bond data well, as shown previously[6] and tested more
480 extensively by much larger datasets here (Supplementary Fig. 1 and Fig. 5d), the four best-fit model
481 parameters correlate with neither T cell effector function nor the catch bond intensity for either
482 class I or class II system (Supplementary Fig. 6), hence informing no biological insights.
483 Consequently, it cannot distinguish the class I and class II systems because the parameters of the
484 generic two-pathway model have nothing to do with the differential structures of the class I and II
485 systems. This comparison highlights the utility and usefulness of our models.

486 Force-induced conformational changes of TCR–pMHC-I complexes have been observed or
487 suggested by single-molecule experiments and SMD simulations[6,8]. Parameterizing these

488 conformational changes by the number of unfolded amino acids n^* and the bonding interface titling
489 angle θ in the class I model allows us to explain mechanistically and quantitatively the TCR–
490 pMHC-I catch-slip and slip-only bonds. Indeed, the criteria for catch-slip bond are $n^* > 0$ and $\theta >$
491 0; the greater their values the more pronounced the catch bond. Importantly, the validity of the class
492 I model has been supported by its capability to fit all force-lifetime data published to date and by
493 the correlation between the best-fit model parameters and the available biological activity data
494 induced by the TCR–pMHC-I interactions.

495 By comparison, the respective ranges of n^* and θ for the class II model are smaller,
496 consistent with the sturdier structure of the pMHC-II molecule[23]. Neither experimental nor
497 simulation data have been reported to suggest force-induced conformational changes in the TCR–
498 pMHC-II structure. Our class II model has also been tested by all published data and their best-fit
499 parameters also correlate well with the biological activities induced by the TCR–pMHC-II
500 interactions. Furthermore, the validity of models of both classes has been supported by the findings
501 that the best-fit model parameter δ_0^* correlates with the catch bond intensity I and that the δ_0^* *vs* I
502 and δ_0^* *vs* n^* plots have more appropriate slopes and R^2 values when the model matches than
503 mismatches the data.

504 We should note that since TCR–pMHC unbinding is assumed to be a spatially continuous
505 and temporally instantaneous process, all structural parameters determined here represent mean
506 field values, and they were evaluated by fitting the mean bond lifetime *vs* force data. However,
507 individual bond dissociation events are inherently stochastic; and as such, need not be
508 deterministically mapped onto any specific conformational changes in a one-on-one fashion.
509 Instead, any particular bond type and parameter sets are related on the average sense. Future studies
510 are required to extend the current framework to relate more detailed structural changes and bond
511 lifetime distributions, *e.g.*, to account for more sequential partial unfolding events prior to transition
512 state as suggested by experiments[6,11,29].

513 A strength of our agent-based models lies in their ability to incorporate many different ideas
514 and knowledge into a simple 1D formulation. This simplicity facilitates model application to both
515 class I and II experimental systems, enables quantitative interpretation of TCR–pMHC bond
516 lifetime *vs* force profiles, expresses biological functions by biophysical measurements, and suggests
517 structural mechanisms of how the TCR mechanotransduction machinery might work. However, the
518 1D simplification is also a weakness because theoretically these models can only describe single-
519 step dissociation by entropic conformational fluctuation in the low-force regime from a single-state
520 along a single-dissociation path, implicitly assuming that there is only a single energy barrier.
521 Although some catch-slip and slip-only bonds can be described by such simple models[5], more
522 complicated TCR–pMHC bonds has been reported. These are evidenced by the multi-exponential
523 bond lifetime distributions at constant forces, which have been fitted by data-driven multi-state,
524 multi-pathway models[27,28]. To address this weakness, future studies may extend the present 1D
525 model to 2D, e.g., by combining Eqs. 2 and 4, to enable proper description of multi-exponential
526 bond survival probabilities.

527 We introduced the catch-bond intensity I as a dimensionless scaled metric for the bond
528 lifetime *vs* force curve and generated four model parameters that describe the curve's geometric
529 features. Upon analyzing all catch-slip and slip-only bond profiles (a total of 50 curves) published
530 to date by four independent laboratories[4-8,13,15,26-28], we found that these quantities do a better job to
531 predict TCR function than any other quantities. This finding may explain how force amplifies TCR
532 signaling and antigen discrimination, because I is defined by a force curve and n^* and θ only
533 predict signaling when they assume none-zero values at $F > 0$.

534 A recent study showed surprising features of reversed-polarity of TRBV TCRs such that
535 interactions of NP_{366}:H-2D^{bD227K} to TCRs B13.C1 and B17.C1 induced T cell signaling, whereas
536 interactions of the same pMHC to B17.R1 and B17.R2 TCRs did not[15]. Despite that the former two
537 TCRs formed catch-slip bonds with NP_{366}:H-2D^{bD227K} and the latter two TCRs formed slip-only

538 bonds, the authors suggested that the signaling capability of the B13.C1 and B17.C1 TCRs could
539 not be attributed to their force-prolonged bond lifetimes because the B17.C1 TCR–H-2D^{bD227K} bond
540 was shorter-lived than the B17.R2 TCR–NP$_{366}$:H-2D^{bD227K} bond across the entire force range
541 tested. Even at 9.4 pN, which was F_{opt} for the former with a t_{peak} = 0.61 s, the latter lived 2.48 s
542 on average, and the longest lifetime of the latter was t_0 = 2.83 s occurred at zero force[15]. The authors
543 hypothesized that the TCR–pMHC docking orientation, which was "canonical' for the B13.C1 and
544 B17.C1 TCRs but "reversed" for the B17.R1 and B17.R2 TCRs, underlain the signaling outcomes
545 by directing the position of Lck relative to the CD3. However, we suggest that even without
546 knowing the docking orientation, our model parameters are capable of determining the signaling
547 outcomes. Indeed, our analysis correctly maps the data of the B13.C1 and B17.C1 TCRs onto the
548 high peptide potency region and the data of the B17.R1 and B17.R2 TCRs onto the low peptide
549 potency region of the δ_0^* *vs* I (Fig. 4c), δ_0^* *vs* θ (Fig. 4e), and θ *vs* $d_{\alpha 3}$ (Fig. 4f) phase diagrams.
550 Thus, by mechanistically modeling the effect of force on bond dissociation, TCR signaling and
551 antigen discrimination can be predicted by the model parameters.

552 The success in our model applications indicate that the conformational changes assumed in
553 the models may be important to the TCR triggering, thereby suggesting testable hypotheses for
554 future studies designed to investigate the inner workings of the TCR mechanotransduction
555 machinery, *e.g.*, to extend and/or revise models regarding how TCR signaling is triggered. One of
556 the TCR triggering models involves conformational changes and catch bond formation[1,2,56]. Our
557 structure-based models relate catch and slip bonds to TCR–pMHC conformational changes. For the
558 class I model, the parameterized structural changes include force-induced disruption of the MHC
559 $\alpha_1\alpha_2$–β_{2m} interdomain bond, partial unfolding of the $\alpha_1\alpha_2$–α_3 joint, tilting of the TCR–pMHC
560 bonding interface, and partial unfolding of the Vα-Cα and Vβ-Cβ joints. For the class II model,
561 these are primarily limited to the force-induced partial unfolding of the MHC-II α_1-α_2 and β_1-β_2
562 joints as well as the Vα-Cα and Vβ-Cβ joints. Besides these, one additional conformational change

observed in the SMD simulations of TCRαβ–pMHC dissociation is unfolding of the connecting peptides between the TCRαβ ectodomain and transmembrane domain[8]. We chose not to include this conformational change in our models because such unfolding would likely be prevented by the interaction of the Cαβ with the CD3 subunits[28]. Consistent with this assumption, the experimental data used for model fitting to evaluate conformational change parameters (n^* and θ) are those of pMHC bonds with TCR-CD3 complexes on the cell membrane that includes the TCRαβ ligand binding subunits and the CD3 signaling subunits (except for the N15 TCRαβ case which is soluble ectodomain only). Indeed, our previous work found that catch bonds of purified TCRαβ were altered from those of cell surface TCR interacting with the same pMHCs[26,27], which is reflected by their changed model parameters (Supplementary Fig. 11). As such, the TCRαβ conformational changes predicted by our models provide a constraint for possible CD3 conformational changes in the TCR-CD3 complex to be considered in future TCR triggering models.

Another constraint to be considered by future studies is that imposed by the coreceptor CD4 and CD8, as the co-ligation of the coreceptor prolongs bond lifetimes, amplifies catch bonds, and may even changes slip-only bonds to catch-slip bonds[7,13,27]. Future studies should also consider how to extend the current models to pre-TCR catch and slip bonds with a broad range of ligands[29,57]. Instead of the TCRα, the pre-TCR uses the TCRβ chain to dimerize with a common pre-Tα chain, which lacks the variable domain (hence no Vα-Cα hinge). Without extension, even if our models are still able to fit the data of pre-TCR–ligand bonds or data of TCR–pMHC bonds where the TCRβ F-G loop was deleted or bound by an anti-TCR antibody[6], the best-fit model parameters may not correspond to the conformational changes of these bonds which are likely different from the conformational changes in the TCR–pMHC bonds with intact F-G loop.

An objective of the present work is to explore the extent to which 1D models can describe experimental data with a minimal set of meaningful parameters. Our parameters consider coarse-grained structural features and relate catch and slip bonds to specific force-induced conformational

588 changes of the TCR–pMHC complex. This approach should be extendable to the modeling of other
589 receptor–ligand systems of different structural features yet also form catch and slip bonds, such as
590 selectins[17,58,59], integrins[49,50,60-63], cadherin[64], Fcγ receptor[65], notch receptor[66], platelet glycoprotein
591 Ibα[51,67], FimH[68], actin with myosin[69], actin with actin[70,71], cadherin-catenin complex with
592 actin[52], vinculin with F-actin[53], and microtubule with kinetochore particle[72].

593 Our models allow us to develop working hypotheses regarding how T cell function is
594 regulated through structural modulations of catch and slip bonds. For example, our class I model
595 predicts that strengthening of the $\alpha_1\alpha_2$–β_{2m} interdomain bond would weaken the TCR–pMHC catch
596 bond, which would in turn reduce T cell activation. This prediction has been supported by our
597 published data that somatic mutations in HLA-A2 found in some cancer patients impair TCR–
598 pHLA-A2 catch bonds, which may explain the suppressed anti-tumor T cell immunity[8]. More
599 interestingly, our models pave the way for engineering of TCR function for tumor immunotherapy
600 by modulating the TCR catch and slip bonds through alteration of its structures. For example,
601 mutations that weaken the Vα-Cα joint are predicted to strengthen TCR catch bonds and enhance
602 T cell effector function, which suggests a strategy that may be more advantageous compared to
603 mutations at the pMHC docking interface because mutations at the Vα-Cα joint would alter
604 function for any TCR specificity so it may be effective to many tumor antigens. By comparison,
605 mutations at the TCR binding interface may be applicable to a specific pMHC only, and may be
606 riskier in terms of cross-reactivity to self-pMHCs. Thus, rational design guided by catch bond
607 models may provide new TCR engineering strategies that warrant future studies.

608 **Methods**

609 The model developments, characterization, and validation are described in the main text
610 with more details in the Supplementary Model Derivations. Model fitting to experimental data was
611 done by nonlinear curve-fitting in the least-squares sense using the Levenberg-Marquardt algorithm,
612 as detailed in Supplementary Model Derivation, A.4. Model applications, curve-fitting strategies,
613 and biological relevance. Statistical and clustering analyses were done using Bayesian statistics and
614 Lloyd's algorithm, respectively. All analyses were done using MATLAB. All experimental data of
615 force *vs* bond lifetime were measured at room temperature as reported in Refs.[4-8,13,15,26-28] and the
616 TCR–pMHC constructs used were described in the footnotes of Supplementary Tables 3, 4 and 6.

617

618 **Data availability**

619 Source data are provided with this paper through main text and Supplementary Information.
620 Previously published bond lifetime data[4-8,13,15,26-28] re-analyzed for model fitting are summarized
621 and deposited in Github (https://github.com/Chengzhulab/NCOMMS-22-20167).

622

623 **Code availability**

624 All code for three models used in this study are summarized and deposited in Github
625 (https://github.com/Chengzhulab/NCOMMS-22-20167).

626

627 **References**

628 1 Feng, Y., Reinherz, E. L. & Lang, M. J. alphabeta T Cell Receptor Mechanosensing Forces out
629 Serial Engagement. *Trends Immunol* **39**, 596-609, (2018).
630 2 Zhu, C., Chen, W., Lou, J., Rittase, W. & Li, K. Mechanosensing through immunoreceptors.
631 *Nature Immunology* **20**, 1269-1278, (2019).
632 3 Liu, B., Kolawole, E. M. & Evavold, B. D. Mechanobiology of T Cell Activation: To Catch a
633 Bond. *Annu Rev Cell Dev Biol* **37**, 65-87, (2021).
634 4 Liu, B., Chen, W., Evavold, B. D. & Zhu, C. Accumulation of dynamic catch bonds between
635 TCR and agonist peptide-MHC triggers T cell signaling. *Cell* **157**, 357-368, (2014).

636 5 Hong, J., Persaud, S. P., Horvath, S., Allen, P. M., Evavold, B. D. & Zhu, C. Force-regulated
637 In situ TCR-peptide-bound MHC class II kinetics determine functions of CD4+ T cells. *Journal*
638 *of immunology* **195**, 3557-3564, (2015).
639 6 Das, D. K., Feng, Y., Mallis, R. J., Li, X., Keskin, D. B., Hussey, R. E., Brady, S. K., Wang, J.
640 H., Wagner, G., Reinherz, E. L. & Lang, M. J. Force-dependent transition in the T-cell receptor
641 beta-subunit allosterically regulates peptide discrimination and pMHC bond lifetime.
642 *Proceedings of the National Academy of Sciences of the United States of America* **112**, 1517-
643 1522, (2015).
644 7 Sibener, L. V., Fernandes, R. A., Kolawole, E. M., Carbone, C. B., Liu, F., McAffee, D.,
645 Birnbaum, M. E., Yang, X., Su, L. F., Yu, W., Dong, S., Gee, M. H., Jude, K. M., Davis, M.
646 M., Groves, J. T., Goddard, W. A., 3rd, Heath, J. R., Evavold, B. D., Vale, R. D. & Garcia, K.
647 C. Isolation of a Structural Mechanism for Uncoupling T Cell Receptor Signaling from Peptide-
648 MHC Binding. *Cell* **174**, 672-687 e627, (2018).
649 8 Wu, P., Zhang, T., Liu, B., Fei, P., Cui, L., Qin, R., Zhu, H., Yao, D., Martinez, R. J., Hu, W.,
650 An, C., Zhang, Y., Liu, J., Shi, J., Fan, J., Yin, W., Sun, J., Zhou, C., Zeng, X., Xu, C., Wang,
651 J., Evavold, B. D., Zhu, C., Chen, W. & Lou, J. Mechano-regulation of Peptide-MHC Class I
652 Conformations Determines TCR Antigen Recognition. *Mol Cell* **73**, 1015-1027 e1017, (2019).
653 9 Zhao, X., Kolawole, E. M., Chan, W., Feng, Y., Yang, X., Gee, M. H., Jude, K. M., Sibener, L.
654 V., Fordyce, P. M., Germain, R. N., Evavold, B. D. & Garcia, K. C. Tuning T cell receptor
655 sensitivity through catch bond engineering. *Science* **376**, eabl5282, (2022).
656 10 Courtney, A. H., Lo, W. L. & Weiss, A. TCR Signaling: Mechanisms of Initiation and
657 Propagation. *Trends Biochem Sci* **43**, 108-123, (2018).
658 11 Feng, Y., Brazin, K. N., Kobayashi, E., Mallis, R. J., Reinherz, E. L. & Lang, M. J.
659 Mechanosensing drives acuity of alphabeta T-cell recognition. *Proceedings of the National*
660 *Academy of Sciences of the United States of America* **114**, E8204-E8213, (2017).
661 12 McKeithan, T. W. Kinetic proofreading in T-cell receptor signal transduction. *Proceedings of*
662 *the National Academy of Sciences of the United States of America* **92**, 5042-5046, (1995).
663 13 Hong, J., Ge, C., Jothikumar, P., Yuan, Z., Liu, B., Bai, K., Li, K., Rittase, W., Shinzawa, M.,
664 Zhang, Y., Palin, A., Love, P., Yu, X., Salaita, K., Evavold, B. D., Singer, A. & Zhu, C. A TCR
665 mechanotransduction signaling loop induces negative selection in the thymus. *Nat Immunol* **19**,
666 1379-1390, (2018).
667 14 Liu, Y., Blanchfield, L., Ma, V. P., Andargachew, R., Galior, K., Liu, Z., Evavold, B. & Salaita,
668 K. DNA-based nanoparticle tension sensors reveal that T-cell receptors transmit defined pN
669 forces to their antigens for enhanced fidelity. *Proceedings of the National Academy of Sciences*
670 *of the United States of America* **113**, 5610-5615, (2016).
671 15 Zareie, P., Szeto, C., Farenc, C., Gunasinghe, S. D., Kolawole, E. M., Nguyen, A., Blyth, C.,
672 Sng, X. Y. X., Li, J., Jones, C. M., Fulcher, A. J., Jacobs, J. R., Wei, Q., Wojciech, L., Petersen,
673 J., Gascoigne, N. R. J., Evavold, B. D., Gaus, K., Gras, S., Rossjohn, J. & La Gruta, N. L.
674 Canonical T cell receptor docking on peptide-MHC is essential for T cell signaling. *Science*
675 **372**, (2021).
676 16 Dembo, M., Torney, D. C., Saxman, K. & Hammer, D. The reaction-limited kinetics of
677 membrane-to-surface adhesion and detachment. *Proc. R. Soc. Lond. B Biol. Sci.* **234**, 55-83,
678 (1988).
679 17 Marshall, B. T., Long, M., Piper, J. W., Yago, T., McEver, R. P. & Zhu, C. Direct observation
680 of catch bonds involving cell-adhesion molecules. *Nature* **423**, 190-193, (2003).
681 18 Grandbois, M., Beyer, M., Rief, M., Clausen-Schaumann, H. & Gaub, H. E. How strong is a
682 covalent bond? *Science* **283**, 1727-1730, (1999).
683 19 Bell, G. Models for the specific adhesion of cells to cells. *Science* **200**, 618-627, (1978).
684 20 Liu, B., Chen, W. & Zhu, C. Molecular force spectroscopy on cells. *Annu. Rev. Phys. Chem.*
685 **66**, 427-451, (2014).

686 21 Guo, S., Efremov, A. K. & Yan, J. Understanding the catch-bond kinetics of biomolecules on a
687 one-dimensional energy landscape. *Communications Chemistry* **2**, 30, (2019).
688 22 Adams, Jarrett J., Narayanan, S., Liu, B., Birnbaum, Michael E., Kruse, Andrew C., Bowerman,
689 Natalie A., Chen, W., Levin, Aron M., Connolly, Janet M., Zhu, C., Kranz, David M. & Garcia,
690 K. C. T cell receptor signaling is limited by docking geometry to peptide-major
691 histocompatibility complex. *Immunity* **35**, 681-693, (2011).
692 23 Rossjohn, J., Gras, S., Miles, J. J., Turner, S. J., Godfrey, D. I. & McCluskey, J. T cell antigen
693 receptor recognition of antigen-presenting molecules. *Annual review of immunology* **33**, 169-
694 200, (2015).
695 24 Banik, D., Hamidinia, M., Brzostek, J., Wu, L., Stephens, H. M., MacAry, P. A., Reinherz, E.
696 L., Gascoigne, N. R. J. & Lang, M. J. Single Molecule Force Spectroscopy Reveals Distinctions
697 in Key Biophysical Parameters of alphabeta T-Cell Receptors Compared with Chimeric
698 Antigen Receptors Directed at the Same Ligand. *J Phys Chem Lett* **12**, 7566-7573, (2021).
699 25 Hwang, W., Mallis, R. J., Lang, M. J. & Reinherz, E. L. The alphabetaTCR mechanosensor
700 exploits dynamic ectodomain allostery to optimize its ligand recognition site. *Proceedings of*
701 *the National Academy of Sciences of the United States of America* **117**, 21336-21345, (2020).
702 26 Liu, B., Chen, W., Natarajan, K., Li, Z., Margulies, D. H. & Zhu, C. The cellular environment
703 regulates in situ kinetics of T-cell receptor interaction with peptide major histocompatibility
704 complex. *European journal of immunology* **45**, 2099-2110, (2015).
705 27 Rushdi, M. N., Pan, V., Li, K., Travaglino, S., Choi, H.-K., Hong, J., Griffitts, F., Agnihotri, P.,
706 Mariuzza, R. A., Ke, Y. & Zhu, C. Cooperative binding of TCR and CD4 to pMHC enhances
707 TCR sensitivity. *Nature Communications*, in press.
708 28 Yuan, Z., Cong, P., Natarajan, Ge, C., Travaglino, S., Beesam, S., Grazette, D., Krogsgaard, M.
709 & Zhu, C. Cooperative ectodomain interaction among TCRαβ, CD3γε, and CD3δε enhances
710 TCR mechanotransduction. *bioRxiv*,
711 https://www.biorxiv.org/content/10.1101/2022.1104.1114.488403v488401, (2022).
712 29 Das, D. K., Mallis, R. J., Duke-Cohan, J. S., Hussey, R. E., Tetteh, P. W., Hilton, M., Wagner,
713 G., Lang, M. J. & Reinherz, E. L. Pre-T Cell Receptors (Pre-TCRs) Leverage Vbeta
714 Complementarity Determining Regions (CDRs) and Hydrophobic Patch in Mechanosensing
715 Thymic Self-ligands. *The Journal of biological chemistry* **291**, 25292-25305, (2016).
716 30 Kramers, H. A. Brownian motion in a field of force and the diffusion model of chemical
717 reactions. *Physica* **7**, 284–304, (1940).
718 31 Dudko, O. K., Hummer, G. & Szabo, A. Intrinsic rates and activation free energies from single-
719 molecule pulling experiments. *Physical review letters* **96**, 108101, (2006).
720 32 Smith, S. B., Finzi, L. & Bustamante, C. Direct mechanical measurements of the elasticity of
721 single DNA molecules by using magnetic beads. *Science* **258**, 1122-1126, (1992).
722 33 Bouchiat, C., Wang, M. D., Allemand, J., Strick, T., Block, S. M. & Croquette, V. Estimating
723 the persistence length of a worm-like chain molecule from force-extension measurements.
724 *Biophysical journal* **76**, 409-413, (1999).
725 34 Huang, J., Zarnitsyna, V. I., Liu, B., Edwards, L. J., Jiang, N., Evavold, B. D. & Zhu, C. The
726 kinetics of two-dimensional TCR and pMHC interactions determine T-cell responsiveness.
727 *Nature* **464**, 932-936, (2010).
728 35 Xiang, S., Nie, F. & Zhang, C. Learning a Mahalanobis distance metric for data clustering and
729 classification. *Pattern Recognition* **41**, 3600-3612, (2008).
730 36 Pereverzev, Y. V., Prezhdo, O. V., Forero, M., Sokurenko, E. V. & Thomas, W. E. The two-
731 pathway model for the catch-slip transition in biological adhesion. *Biophysical journal* **89**,
732 1446-1454, (2005).
733 37 Kersh, G. J. & Allen, P. M. Structural basis for T cell recognition of altered peptide ligands: a
734 single T cell receptor can productively recognize a large continuum of related ligands. *J Exp*
735 *Med* **184**, 1259-1268, (1996).

38 Natarajan, A., Nadarajah, V., Felsovalyi, K., Wang, W., Jeyachandran, V. R., Wasson, R. A., Cardozo, T., Bracken, C. & Krogsgaard, M. Structural Model of the Extracellular Assembly of the TCR-CD3 Complex. *Cell Rep* **14**, 2833-2845, (2016).
39 Lapidus, L. J., Steinbach, P. J., Eaton, W. A., Szabo, A. & Hofrichter, J. Effects of Chain Stiffness on the Dynamics of Loop Formation in Polypeptides. Appendix: Testing a 1-Dimensional Diffusion Model for Peptide Dynamics. *J. Phys. Chem. B* **106**, 11628-11640, (2002).
40 Gebhardt, J. C., Bornschlogl, T. & Rief, M. Full distance-resolved folding energy landscape of one single protein molecule. *Proceedings of the National Academy of Sciences of the United States of America* **107**, 2013-2018, (2010).
41 Gohring, J., Kellner, F., Schrangl, L., Platzer, R., Klotzsch, E., Stockinger, H., Huppa, J. B. & Schutz, G. J. Temporal analysis of T-cell receptor-imposed forces via quantitative single molecule FRET measurements. *Nature communications* **12**, 2502, (2021).
42 Ma, R., Kellner, A. V., Ma, V. P., Su, H., Deal, B. R., Brockman, J. M. & Salaita, K. DNA probes that store mechanical information reveal transient piconewton forces applied by T cells. *Proceedings of the National Academy of Sciences of the United States of America* **116**, 16949-16954, (2019).
43 Ma, V. P., Liu, Y., Blanchfield, L., Su, H., Evavold, B. D. & Salaita, K. Ratiometric Tension Probes for Mapping Receptor Forces and Clustering at Intermembrane Junctions. *Nano letters* **16**, 4552-4559, (2016).
44 Wang, M. S., Hu, Y., Sanchez, E. E., Xie, X., Roy, N. H., de Jesus, M., Winer, B. Y., Zale, E. A., Jin, W., Sachar, C., Lee, J. H., Hong, Y., Kim, M., Kam, L. C., Salaita, K. & Huse, M. Mechanically active integrins target lytic secretion at the immune synapse to facilitate cellular cytotoxicity. *Nature communications* **13**, 3222, (2022).
45 Limozin, L., Bridge, M., Bongrand, P., Dushek, O., van der Merwe, P. A. & Robert, P. TCR-pMHC kinetics under force in a cell-free system show no intrinsic catch bond, but a minimal encounter duration before binding. *Proceedings of the National Academy of Sciences of the United States of America* **116**, 16943-16948, (2019).
46 Barsegov, V. & Thirumalai, D. Dynamics of unbinding of cell adhesion molecules: transition from catch to slip bonds. *Proceedings of the National Academy of Sciences of the United States of America* **102**, 1835-1839, (2005).
47 Evans, E., Leung, A., Heinrich, V. & Zhu, C. Mechanical switching and coupling between two dissociation pathways in a P-selectin adhesion bond. *Proceedings of the National Academy of Sciences of the United States of America* **101**, 11281-11286, (2004).
48 Lou, J. & Zhu, C. A structure-based sliding-rebinding mechanism for catch bonds. *Biophys. J.* **92**, 1471-1485, (2007).
49 Chen, W., Lou, J. & Zhu, C. Forcing switch from short- to intermediate- and long-lived states of the alphaA domain generates LFA-1/ICAM-1 catch bonds. *J. Biol. Chem.* **285**, 35967-35978, (2010).
50 Kong, F., Garcia, A. J., Mould, A. P., Humphries, M. J. & Zhu, C. Demonstration of catch bonds between an integrin and its ligand. *J Cell Biol* **185**, 1275-1284, (2009).
51 Ju, L., Dong, J. F., Cruz, M. A. & Zhu, C. The N-terminal flanking region of the A1 domain regulates the force-dependent binding of von Willebrand factor to platelet glycoprotein Ibalpha. *The Journal of biological chemistry* **288**, 32289-32301, (2013).
52 Buckley, C. D., Tan, J., Anderson, K. L., Hanein, D., Volkmann, N., Weis, W. I., Nelson, W. J. & Dunn, A. R. Cell adhesion. The minimal cadherin-catenin complex binds to actin filaments under force. *Science* **346**, 1254211, (2014).
53 Huang, D. L., Bax, N. A., Buckley, C. D., Weis, W. I. & Dunn, A. R. Vinculin forms a directionally asymmetric catch bond with F-actin. *Science* **357**, 703-706, (2017).

785 54 Owen, L. M., Bax, N. A., Weis, W. I. & Dunn, A. R. The C-terminal actin-binding domain of
786 talin forms an asymmetric catch bond with F-actin. *Proceedings of the National Academy of*
787 *Sciences of the United States of America* **119**, e2109329119, (2022).
788 55 Thomas, W. Catch bonds in adhesion. *Annu Rev Biomed Eng* **10**, 39-57, (2008).
789 56 Mariuzza, R. A., Agnihotri, P. & Orban, J. The structural basis of T-cell receptor (TCR)
790 activation: An enduring enigma. *The Journal of biological chemistry* **295**, 914-925, (2020).
791 57 Mallis, R. J., Bai, K., Arthanari, H., Hussey, R. E., Handley, M., Li, Z., Chingozha, L., Duke-
792 Cohan, J. S., Lu, H., Wang, J. H., Zhu, C., Wagner, G. & Reinherz, E. L. Pre-TCR ligand
793 binding impacts thymocyte development before alphabetaTCR expression. *Proceedings of the*
794 *National Academy of Sciences of the United States of America* **112**, 8373-8378, (2015).
795 58 Sarangapani, K. K., Yago, T., Klopocki, A. G., Lawrence, M. B., Fieger, C. B., Rosen, S. D.,
796 McEver, R. P. & Zhu, C. Low force decelerates L-selectin dissociation from P-selectin
797 glycoprotein ligand-1 and endoglycan. *J. Biol. Chem.* **279**, 2291-2298, (2004).
798 59 Wayman, A. M., Chen, W., McEver, R. P. & Zhu, C. Triphasic force dependence of E-
799 selectin/ligand dissociation governs cell rolling under flow. *Biophys. J.* **99**, 1166-1174, (2010).
800 60 Choi, Y. I., Duke-Cohan, J. S., Chen, W., Liu, B., Rossy, J., Tabarin, T., Ju, L., Gui, J., Gaus,
801 K., Zhu, C. & Reinherz, E. L. Dynamic control of beta1 integrin adhesion by the plexinD1-
802 sema3E axis. *Proc. Natl. Acad. Sci. U.S.A.* **111**, 379-384, (2014).
803 61 Rosetti, F., Chen, Y., Sen, M., Thayer, E., Azcutia, V., Herter, J. M., Luscinskas, F. W., Cullere,
804 X., Zhu, C. & Mayadas, T. N. A Lupus-Associated Mac-1 Variant Has Defects in Integrin
805 Allostery and Interaction with Ligands under Force. *Cell Rep* **10**, 1655-1664, (2015).
806 62 Chen, Y., Lee, H., Tong, H., Schwartz, M. & Zhu, C. Force regulated conformational change
807 of integrin alphaVbeta3. *Matrix Biol* **60-61**, 70-85, (2017).
808 63 Chen, Y., Ju, L. A., Zhou, F., Liao, J., Xue, L., Su, Q. P., Jin, D., Yuan, Y., Lu, H., Jackson, S.
809 P. & Zhu, C. An integrin alphaIIbbeta3 intermediate affinity state mediates biomechanical
810 platelet aggregation. *Nat Mater* **18**, 760-769, (2019).
811 64 Manibog, K., Li, H., Rakshit, S. & Sivasankar, S. Resolving the molecular mechanism of
812 cadherin catch bond formation. *Nature communications* **5**, 3941, (2014).
813 65 Nishi, H., Furuhashi, K., Cullere, X., Saggu, G., Miller, M. J., Chen, Y., Rosetti, F., Hamilton,
814 S. L., Yang, L., Pittman, S. P., Liao, J., Herter, J. M., Berry, J. C., DeAngelo, D. J., Zhu, C.,
815 Tsokos, G. C. & Mayadas, T. N. Neutrophil FcgammaRIIA promotes IgG-mediated glomerular
816 neutrophil capture via Abl/Src kinases. *The Journal of clinical investigation* **127**, 3810-3826,
817 (2017).
818 66 Luca, V. C., Choul Kim, B., Ge, C., Kakuda, S., Roein-Peikar, M., Haltiwanger, R. S., Zhu, C.,
819 Ha, T. & Garcia, K. C. Notch-Jagged complex structure implicates mechanical force in ligand
820 discrimination. *Science* **355**, 1320-1324, (2017).
821 67 Yago, T., Lou, J., Wu, T., Yang, J., Miner, J. J., Coburn, L., Lopez, J. A., Cruz, M. A., Dong,
822 J. F., McIntire, L. V., McEver, R. P. & Zhu, C. Platelet glycoprotein Ibalpha forms catch bonds
823 with human WT vWF but not with type 2B von Willebrand disease vWF. *J. Clin. Invest.* **118**,
824 3195-3207, (2008).
825 68 Yakovenko, O., Sharma, S., Forero, M., Tchesnokova, V., Aprikian, P., Kidd, B., Mach, A.,
826 Vogel, V., Sokurenko, E. & Thomas, W. E. FimH forms catch bonds that are enhanced by
827 mechanical force due to allosteric regulation. *The Journal of biological chemistry* **283**, 11596-
828 11605, (2008).
829 69 Guo, B. & Guilford, W. H. Mechanics of actomyosin bonds in different nucleotide states are
830 tuned to muscle contraction. *Proceedings of the National Academy of Sciences of the United*
831 *States of America* **103**, 9844-9849, (2006).
832 70 Lee, C. Y., Lou, J. Z., Wen, K. K., McKane, M., Eskin, S. G., Ono, S., Chien, S., Rubenstein,
833 P. A., Zhu, C. & McIntire, L. V. Actin depolymerization under force is governed by lysine

113:glutamic acid 195-mediated catch-slip bonds. *Proc. Natl. Acad. Sci. U.S.A.* **110**, 5022-5027, (2013).

71 Lee, C. Y., Lou, J., Wen, K. K., McKane, M., Eskin, S. G., Rubenstein, P. A., Chien, S., Ono, S., Zhu, C. & McIntire, L. V. Regulation of actin catch-slip bonds with a RhoA-formin module. *Sci Rep* **6**, 35058, (2016).

72 Akiyoshi, B., Sarangapani, K. K., Powers, A. F., Nelson, C. R., Reichow, S. L., Arellano-Santoyo, H., Gonen, T., Ranish, J. A., Asbury, C. L. & Biggins, S. Tension directly stabilizes reconstituted kinetochore-microtubule attachments. *Nature* **468**, 576-579, (2010).

Acknowledgments

We thank Baoyu Liu, Jinsung Hong, Peng Wu, Tongtong Zhang, Aswin Natarajan, and Michelle Krogsgaard for sharing their published BFP experimental data for re-analysis and model fitting. This work was supported by a Postdoctoral Fellowship from the National Research Foundation of South Korea (2021R1A6A3A03038382 to H.-K.C.), by a National Natural Science Foundation of China grant (31971237 to W.C.), and by a National Natural Science Foundation of China grant (32090044 to J.L.). This work was also supported by National Institutes of Health grants (U01CA214354, U01CA250040, R01CA243486, and R01GM061126 to C.Z.).

Author contributions

H.-K.C. and C.Z. conceived the project and developed the models. H.-K.C., K.L., P.C., M.N.R., and C.G. provided data prior to their publication. H.-K.C. performed model analysis and data fitting. H.-K.C., K.L. and C.Z. made key observations and conclusions from analyses. H.-K.C., K.L., and C.Z. prepared the manuscript with input from other authors.

Competing interests

No authors have competing interests to declare.

Figures

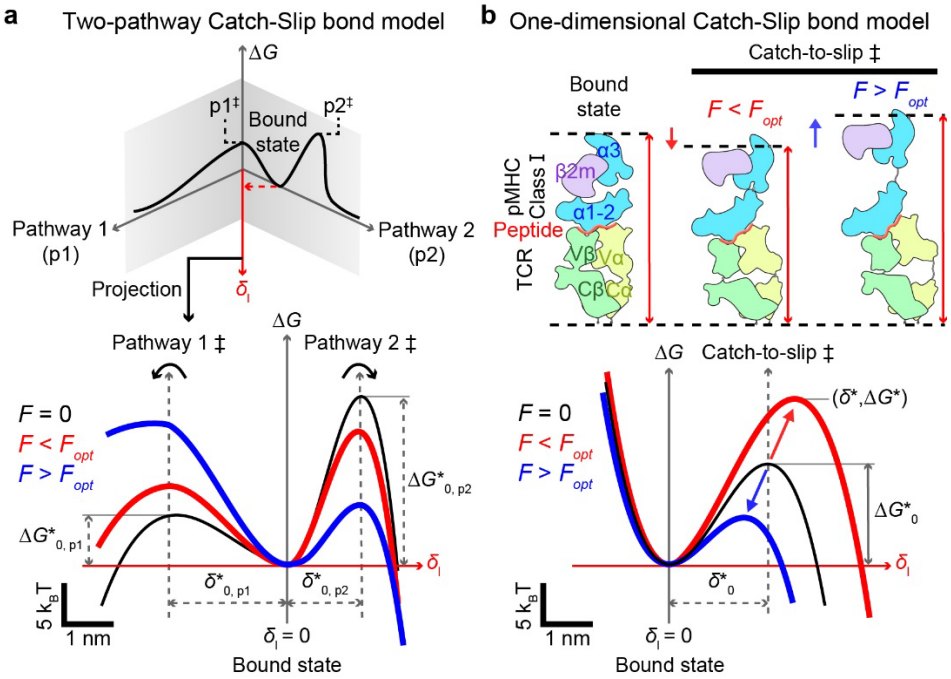

Figure 1 | Comparison between the two-pathway model and the TCR–pMHC-I model for catch bond. **a** *Upper*: The 2D energy landscape of the two-pathway model where the bond is trapped in the bound-state energy well by two energy barriers that resist dissociation along two pathways, p1 and p2, with two distinct transition states, p1‡ and p2‡. The application of force projects the energy landscape towards a dissociation pathway along force (δ_l). *Lower*: Force also tilts the energy-landscape, raising the energy barrier of the first pathway and lowering the energy barrier of the second pathway on the energy landscape projection (*red* and *blue*) relative to their positions in the absence of force (*black*). **b** *Lower*: The proposed 1D energy landscape of TCR–pMHC-I model with a single transition state δ^*. Below an optimal value (F_{opt}), force raises the energy barrier (*red*) relative to the zero-force conformation (*black*) by contraction of flexible regions due to entropic fluctuation. Above F_{opt}, force lowers the energy barrier (*blue*) by stretching the molecular complex. Together, these two mechanisms give rise to a catch-slip bond. *Upper*: Schematics of the TCR–pMHC-I structure (*left*) and its conformational changes that correspond to low (*middle*) and high (*right*) forces.

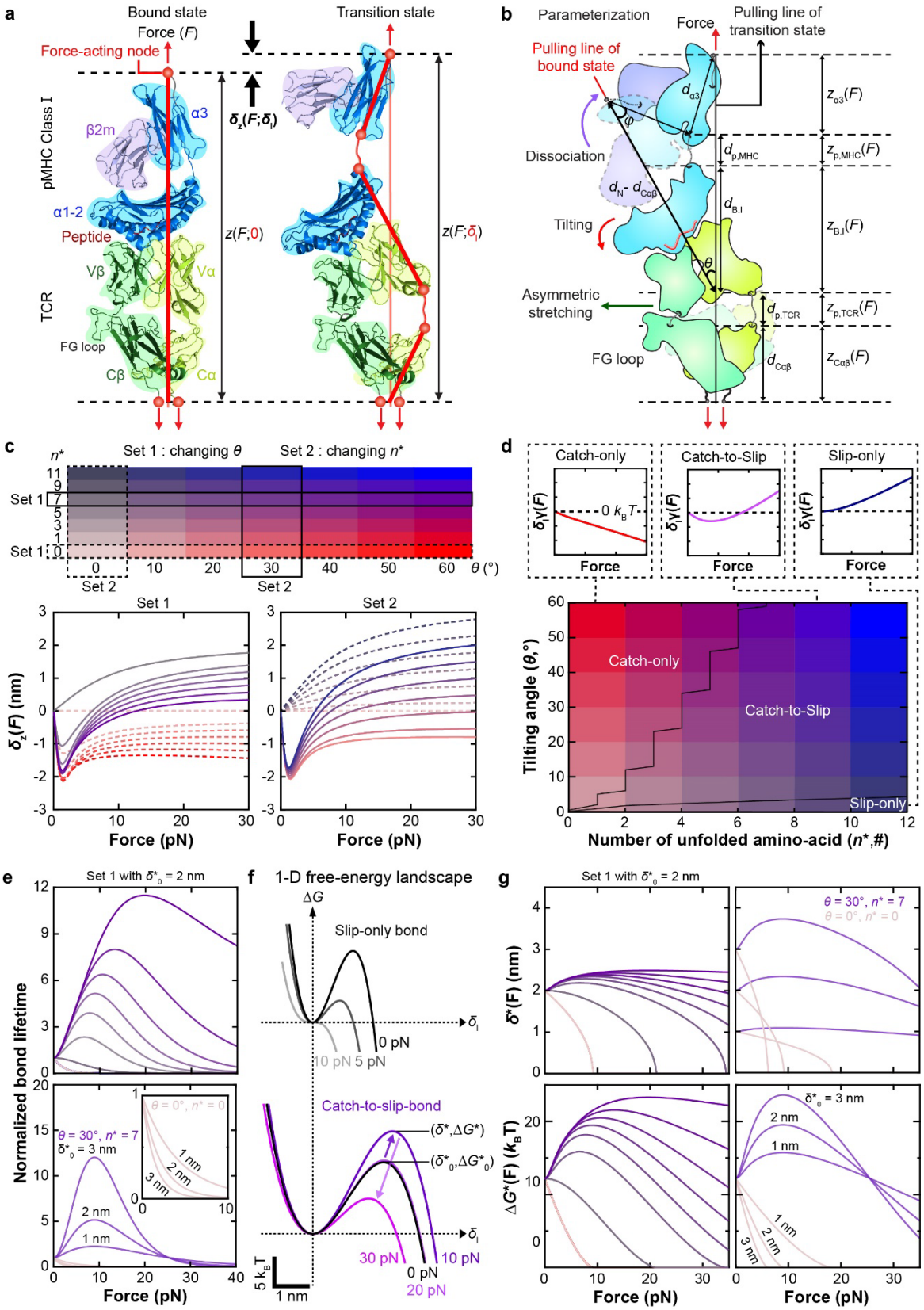

Figure 2 | Structure, mechanics, and characteristics of the TCR–pMHC-I catch bond model.

a Force-induced conformational changes of a TCR–pMHC-I complex as it traverses from the bound state (*left*) to the transition state (*right*). The diagrams of the 2C TCR α (*yellow*) β (*green*) subunits

882 and the DEVA peptide (*red*) bound to the H2-K^b (various domains indicated) are based on snapshots
883 from SMD simulations performed on the complex structure (2CKB) at the initial time (bound state)
884 and a later time (transition state)[8]. The force-transmission path is shown as red lines connecting the
885 force-acting nodes. **b** Various contributions to the total extension projected on the force axis:
886 rotation of the α_3- β_{2m} domains about the MHC C-terminus upon dissociation of the β_{2m}–$\alpha_1\alpha_2$
887 interdomain bond ($z_{\alpha 3}$), relative rotation between α_3 and $\alpha_1\alpha_2$ about their stretched interdomain
888 hinge ($z_{\mathrm{p,MHC}}$), tilting of the MHC $\alpha_1\alpha_2$ complexed with TCR Vαβ ($z_{\mathrm{B.I}}$), rotation about and
889 extension of the Vα–Cα interdomain hinge ($z_{\mathrm{p,TCR}}$), and extension of the Cαβ and rotation about
890 their C-termini ($z_{\mathrm{C}\alpha\beta}$). Two α_3-β_{2m} structures are shown: before (light colors) and after (dark colors)
891 β_{2m} dissociation from $\alpha_1\alpha_2$., with two parameters describing their contributions to the total
892 extension: $d_{\alpha 3}$ = the distance between the α3 C- and N-termini excluding the $\alpha_1\alpha_2$–α3 hinge and θ
893 = the angle between the normal direction of the TCR–pMHC bonding interface at the bound state
894 (cf. (**a**), *left*) and the tilted direction at the transition state (cf. (**a**), *right*). **c** Extension change *vs*
895 force curves (*lower*) for the color-matched n^* and θ values (*upper*). The left panel (set 1 in *upper*
896 table) shows the effect of changing θ with (n^* = 7) and without (n^* = 0) partial unfolding. The right
897 panel (set 2) shows the effect of changing n^* with (θ = 30°) and without (θ = 0°) tilting. **d** n^*-θ
898 phase diagram showing three parameter domains: slip-only, catch-slip, and catch-only respectively
899 colored by red-purple, purple-blue, and blue-black. Upper insets indicate corresponding energy
900 change $\delta_l\gamma$ *vs* force curves for each bond type. **e** Theoretical normalized bond lifetime *vs* force
901 curves for indicated parameters. The upper and lower panels show the respective effects of changing
902 θ and δ_0^* from the set 1 parameters defined in (**c**). **f** Energy landscapes expressed as families ΔG *vs*
903 δ_l curves for a range of forces for slip-only (*upper*) and catch-slip (*lower*) bonds. The bound state
904 is located at the origin ΔG = 0 and δ_l = 0. The transition state has an energy of ΔG^* located at δ^*
905 when F > 0 and ΔG_0^* located at δ_0^* when F = 0. **g** Plots of transition state location δ^* (*upper*) and

height of energy barrier ΔG^* (*lower*) *vs* force F for changing θ while keeping δ_0^* constant (*left*) or changing δ_0^* while keeping θ constant (*right*) for the indicated values from parameter table in (**c**).

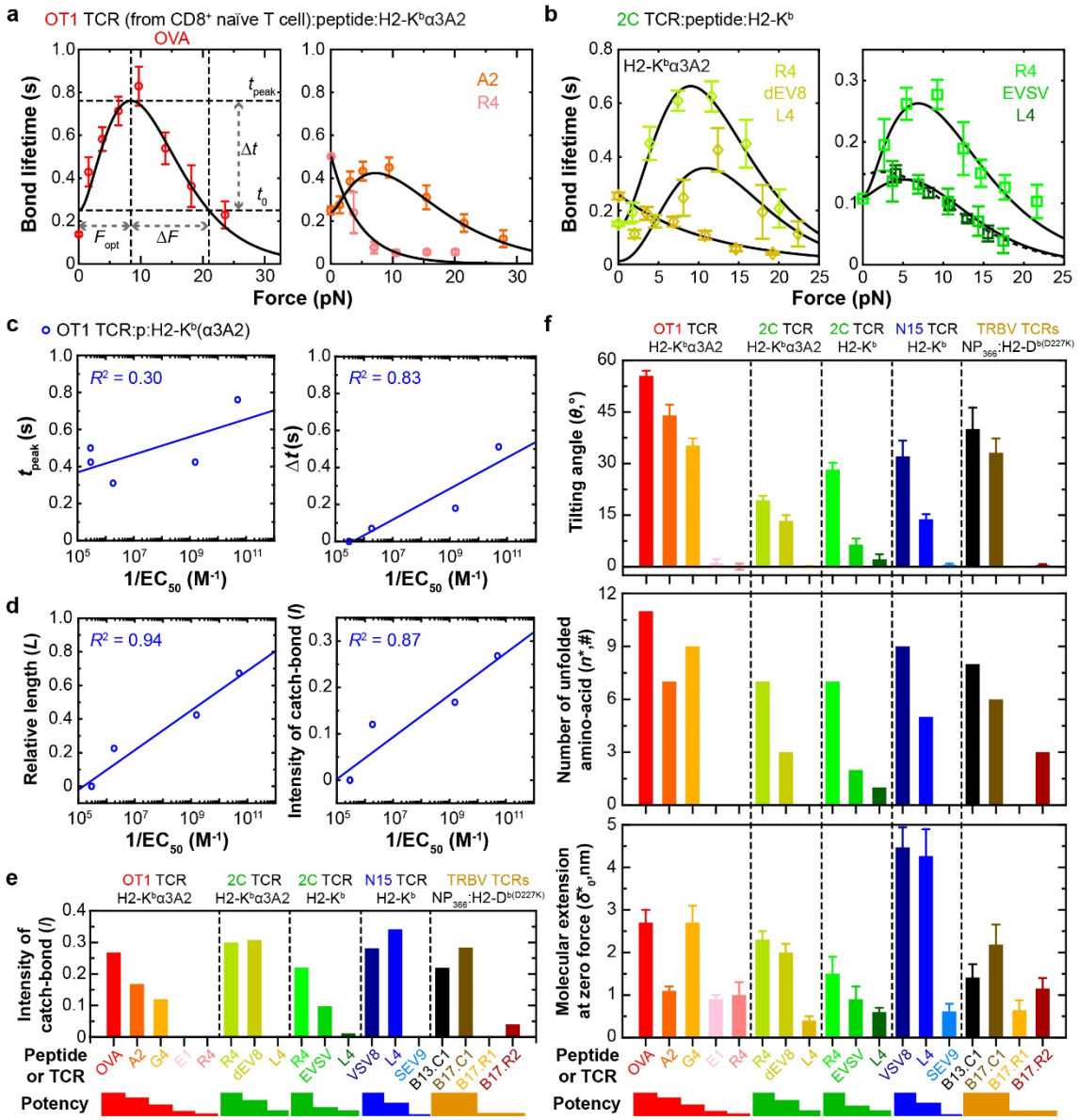

Figure 3 | TCR bond type characterization and correlation with pMHC-I biological activity. **a-b** Fitting of theoretical $1/k(F)$ curves to experimental bond lifetime *vs* force data (*points*, mean ± sem, re-analyzed from Refs. [4,8]) of OT1 (**a**) or 2C (**b**) TCR expressed on CD8$^+$ naïve T cells interacting with indicated p:H2-K^{b}α3A2 ((**a**) and (**b**) *left*) or on CD8$^-$ 2C hybridomas interacting with indicated p:H2-K^b ((**b**) *right*). Several metrics are defined to characterize the force-lifetime curve as indicated in the left panel of (**a**): F_{opt} is the "optimal force" where lifetime peaks (t_{peak}), Δt is the lifetime increase from the zero-force value t_0 to t_{peak}, and ΔF is the force increase from F_{opt} to the force where lifetime returns to t_0. **c-d** Two dimensional metrics, t_{peak} and Δt (**c**), and

917 two dimensionless metrics, $L = \Delta t/t_{\text{peak}}$ and $I = L/(1+B)$ where $B = \Delta F/F_{\text{opt}}$ (**d**), are plotted
918 *vs* the logarithm of the reciprocal peptide concentration required to stimulate half-maximal T cell
919 proliferation ($1/EC_{50}$) and fitted by a linear function. **e** Intensity of catch bond, I, calculated using
920 the fitted force-lifetime curves of OT1, 2C TCR on primary T cells, 2C TCR on hybridomas,
921 purified N15 TCRαβ, or TRBV TCRs (B13.C1/B17.C1 and B17.R1/B17.R2) expressed on
922 hybridomas interacting with their corresponding pMHCs are plotted according to the ranked-order
923 of peptide potencies (*bottom*). **f** Best-fit model parameters θ (the tilted angle of the bonding
924 interface, *upper*), n^* (the number of unfolded amino acids, *middle*), and δ_0^* (the width of zero-force
925 free-energy well, *lower*) are plotted according to the ranked order of the peptide potencies (*bottom*).
926 All error bars in 1st and 2nd rows are fitting error (Supplementary Table 3).
927

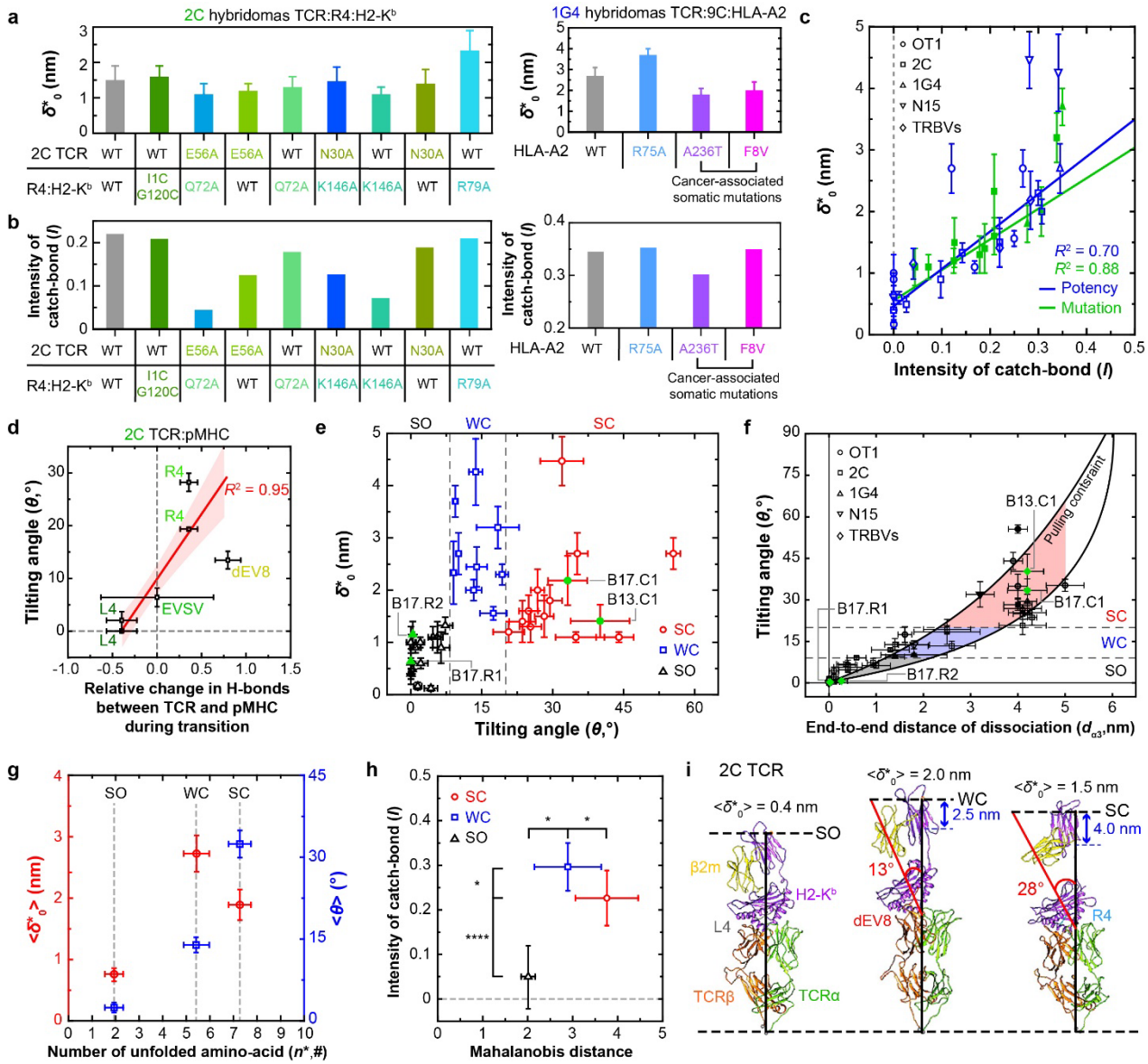

Figure 4 | Properties and biological relevance of class I model parameters. **a-b** The width of zero-force energy well δ_0^* (**a**) and the intensity of catch bond I (**b**) calculated from WT or mutant 2C TCRs (*left*) and WT 1G4 TCR (*right*) interacting with their corresponding WT or MT pMHCs. The MT 2C TCRs and H2-K^{b}s were designed to destabilize the TCR–pMHC interaction. The MT p:HLA-A2s were designed to either destabilize the TCR–pMHC interaction (R75A) or stabilize the MHC intramolecular interaction (A236T and F8V). **c** Data from **Fig. 3e** and **f** (3rd row) are re-graphed as δ_0^* *vs* I plot to show their correlation (*blue*). Additional δ_0^* *vs* I data from MT TCRs and/or MT pMHCs without functional data also show strong correlation (*green*). Different TCR systems are indicated by different symbols. The two datasets were separately fitted by two straight

938 lines with the goodness-of-fit indicated by R^2. **d** Tilting angle of the bonding interface (θ) *vs*
939 normalized net gain of hydrogen bonds at the interface between 2C TCR and the indicated pMHCs
940 is plotted (*points*) and fitted (*line*) with 95% confident interval shown as shaded area (errors in x-
941 and y-axis represent propagation uncertainty from Supplementary Fig. 3 and fitting error,
942 respectively). **e** Clustering analysis reveals three clusters in the δ_0^*-θ phase diagram: slip-only (SO,
943 *black*), weak catch-slip (WC, *blue*), and strong catch-slip (SC, *red*) bonds. Closed-symbols
944 represent bonds of the WT TCR with WT agonist peptides. **f** Tilting angle (θ) *vs* end-to-end distance
945 of dissociated α3 domain ($d_{\alpha 3}$). The three types of bonds, SO, WC, and SC, are also clustered in
946 this phase diagram, which are separated by the dotted lines that predicted from the pulling
947 constraints of the model. The two pairs of TRBV TCRs are indicated in e and f by green dots. **g**
948 The average molecular extensions at zero force ($\langle\delta_0^*\rangle$, *left ordinate*) and the average rotation angle
949 ($\langle\theta\rangle$, *right ordinate*) (mean ± sem) are plotted *vs* the total number of unfolded amino acids (n^*,
950 *abscissa*) to show three clusters. Each bond type is indicated by a dotted line (n = 14, 9, and 16;
951 number of data related to SO, WC, and SC, respectively, individual data of each cluster are shown
952 in (**e-f**)). **h** Catch bond intensity *vs* Mahalanobis distance plot, again showing three clusters.
953 Principal component analysis was used to find principal axes. Mahalanobis distances for each
954 cluster were calculated using common principal axes from total dataset (number of data is same as
955 (**g**)). **i** Structural models illustrating the conformations of three bond types based on their model
956 parameters based on the previous SMD simulation of the 2C TCR system[8]. Two structural
957 parameters (θ, *red*; $d_{\alpha 3}$, *blue*) are indicated to show the differences between bond types. Unless
958 otherwise described, all errors shown in (**a-f**) are fitting errors (Supplementary Table 3).
959
960

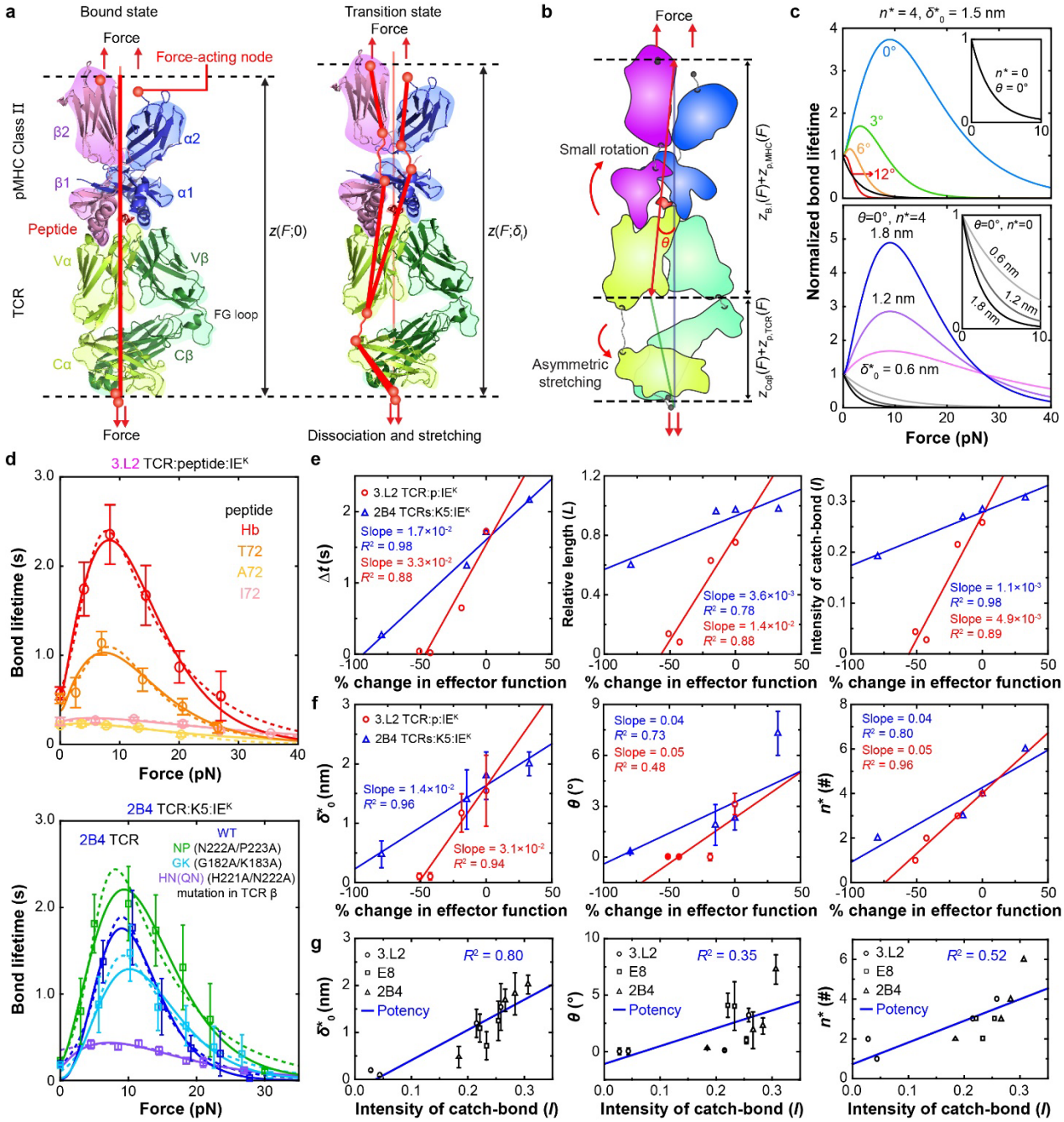

Figure 5 | The TCR–pMHC-II model. a Force-induced conformational changes of a TCR–pMHC-II complex as it traverses from the bound state (*left*) to the transition state (*right*). The diagrams are based on the published co-crystal structure (2IAM) of the E8 TCR α (*yellow*) β (*green*) subunits and the TPI peptide (*red*) bound to the HLA-DR1 α (*blue*) β (*pink*) subunits with various domains indicated. The force-transmission paths are shown as red lines connecting the force-acting nodes. **b** Various contributions to the total extension projected on the force axis: stretching of the TCR Cα and Cβ domains ($z_{C\alpha\beta}$), asymmetric partial unfolding of the TCR Vα-Cα and Vβ-Cβ

interdomain hinges ($z_{\mathrm{p,TCR}}$), asymmetric partial unfolding of the MHC α1-α2 and β1-β2 interdomain hinges ($z_{\mathrm{p,MHC}}$), and rotation between the α1-β1 and α2-β2 domain hinges and tilting of the bonding interface between the MHC α1-β1 and the TCR Vα-Vβ by an angle θ ($z_{\mathrm{B.I}}$). **c** Theoretical normalized bond lifetime *vs* force curves. The effects of changing θ and δ_0^* are shown in the upper and lower panels, respectively, for the indicated parameter values. **d** Fitting of predicted $1/k(F)$ curves (*dashed lines* by two-pathway model and *solid lines* by TCR–pMHC-Ⅱ model) to experimental bond lifetime *vs* force data (*points*, mean ± sem) of 3.L2 TCR on $CD4^-CD8^+$ naive T cells interacting with indicated p:I-E^k's [5] (*upper*) or WT and indicated mutant 2B4 TCRs on hybridomas interacting with K5:I-E^k [28]. **e** Dimensional metrics, Δt (*left*), scaled relative length of bond lifetime L (*middle*), and intensity of catch bond I (*right*) *vs* reciprocal % change (relative to WT) of effector function, i.e., the peptide dose required for 3.L2 T cells to generate 40% B cell apoptosis ($1/EC_{40}$)[37] (*red*) or the area under the dose response curve (AUC) of the 2B4 hybridoma IL-2 production[38] (*blue*) plots. **f** Best-fit model parameters δ_0^* (*left*), θ (*middle*), and n^* (*right*) are plotted *vs* reciprocal relative % change of effector function. **g** The three model parameters in f for both the 3.L2 and 2B4 TCR systems are plotted *vs* the catch-bond intensity I and fitted by a straight line. We also added to each panel an additional point obtained from data and model fit of E8 TCR–TPI:HLA-DR1 interactions[27]. All error bars in **f-g** are fitting error (Supplementary Table 6).

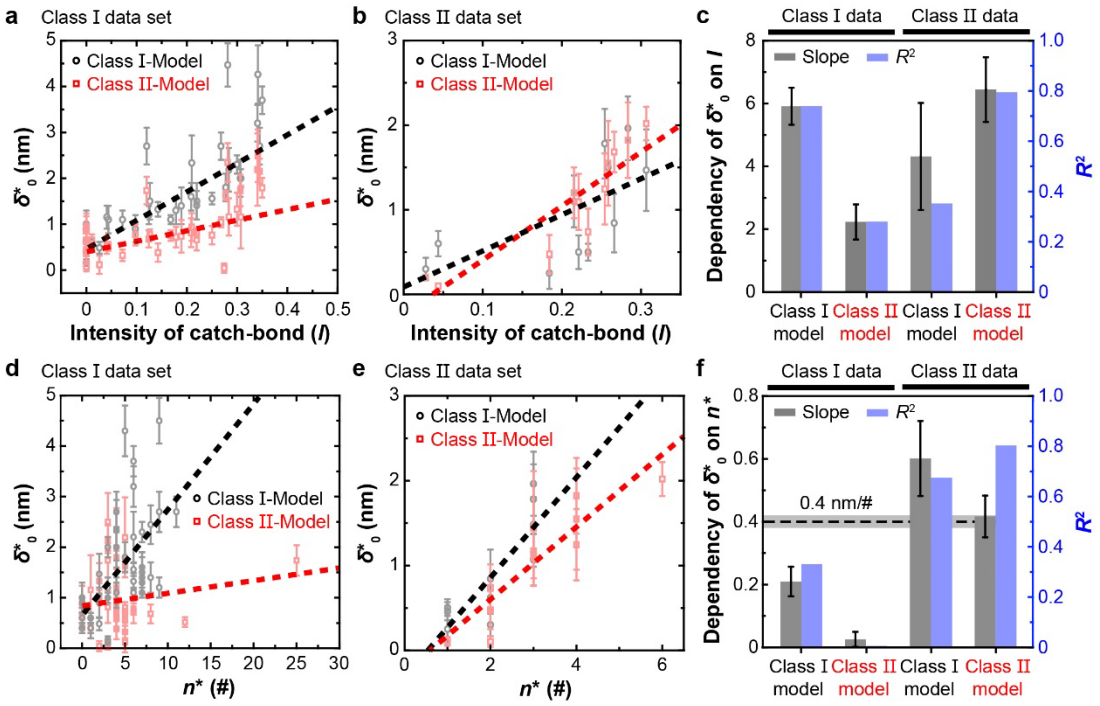

Figure 6 | Cross-examination of class I and II models against class I and II data. a-b δ_0^* *vs I* plots obtained using class I (*black*) or class II (*red*) model to fit force-lifetime data of TCR interacting with pMHC-I (**a**) or pMHC-II (**b**) molecules. In each panel, two sets of parameter values were returned from fitting depending on whether class I (*black*) or class II (*red*) model was used because they are based on different structures and conformational changes of the TCR–pMHC complexes. **c** The slopes (*gray*, the level of correlation between δ_0^* and I) and goodness-of-fit (R^2) (*blue*, the degree of appropriateness of the model for the data) of the linear fit in (**a**) and (**b**) are shown in the matched (1st and 4th groups) and mismatched (2nd and 3rd groups) cases. **d-e** δ_0^* *vs* n^* plots obtained using class I (*black*) or class II (*red*) model to fit force-lifetime data of TCR interacting with pMHC-I (**d**) or pMHC-II (**e**) molecules. **f** The slopes and goodness-of-fit of the linear fit in (**d**) and (**e**) are shown in the matched (1st and 4th groups) and mismatched (2nd and 3rd groups) cases. The slopes indicate the average unfolding extension per amino acid (nm/a.a.) from each model, which are compared to the maximum average contour length per amino acid of ~0.4 nm/a.a. (biophysical limit, black dashed line with considerable deviation)[21,39,40]. All error bars are fitting error (Supplementary Table 6).

Supplementary Information

Catch bond models may explain how force amplifies TCR signaling and antigen discrimination

Hyun-Kyu Choi et al.

*Corresponding author. Email: cheng.zhu@bme.gatech.edu

This PDF file includes:

Supplementary Model Derivations
Supplementary Figures. 1 to 11
Supplementary Tables 1 to 6
References (73 to 79)

Supplementary Methods

Supplementary Model Derivations

A. Kinetic model for TCR–pMHC-I bonds
   A.1. Derivation of the force-induced energy change $\delta_1\gamma(F)$
   A.2. Simplifying assumptions and reducing parameters
   A.3. Defining the dissociation coordinate
   A.4. Model applications, curve-fitting strategies, and biological relevance
   A.5. Class I model constraints
B. Kinetic model for TCR–pMHC-II bonds
   B.1. Development, validation, and characterization
   B.2. Class II model constraints
C. A general biophysical limit of model parameters

Supplementary Figures

Supplementary Fig. 1 | Fitting class I model to data of TCR–pMHC-I bond lifetime *vs* force
Supplementary Fig. 2 | Correlation of class I model parameters with biological activity and TCR bond type
Supplementary Fig. 3 | Hydrogen (H) bond distributions at the TCR–pMHC-I bonding interface
Supplementary Fig. 4 | Pulling and tilting constraints of class I model
Supplementary Fig. 5 | Determining the number of clusters in parameter space
Supplementary Fig. 6 | Lack of correlations between best-fit parameters of the two-pathway model and T cell function
Supplementary Fig. 7 | Characterization of the energy landscape of TCR–pMHC-II dissociation
Supplementary Fig. 8 | Correlation of metrics of TCR–pMHC-II bond lifetime *vs* force curves with T cell biological activity
Supplementary Fig. 9 | Comparing fitting curves of class I and class II models for the same data
Supplementary Fig. 10 | Relative goodness-of-fit of the class I and II models and the two-pathway model to class I and class II data
Supplementary Fig. 11 | Comparison of pMHC interactions with cell surface and purified TCRs

Supplementary Tables

Supplementary Table. 1 | Summary of model constants
Supplementary Table. 2 | Finding the best-fit parameters for OT1 TCR–OVA:H2-K^ba3A2 bond
Supplementary Table. 3 | TCR–pMHC-I bond summary and their best-fitting parameters.
Supplementary Table. 4 | Two-pathway model summary and their best-fitting parameters
Supplementary Table. 5 | Finding the best-fit parameters for the 3.L2 TCR–Hb:I-E^k bond.
Supplementary Table. 6 | TCR–pMHC-II bond summary and their best-fit parameters.

Supplementary References

1068 **Supplementary Model Derivations**

1069 **A. Kinetic model for TCR–pMHC-I bonds**

1070 ***A.1. Derivation of the force-induced energy change $\delta_1\gamma(F)$***

1071 The purpose of this subsection is to provide detailed derivation of the force-induced change
1072 in the energy landscape, or the work done by force as the TCR–pMHC complex is stretched at the
1073 two ends from the bound state to the transition state until dissociation (Fig. 2a, b). Mathematically,
1074 $\delta_1\gamma(F)$ is an integral over a force range $0 \leq f \leq F$, where F is the level of force under which the
1075 kinetic rate is being evaluated (Eq. 2). The integrand $\delta_z(f)$ is the projection on the force direction
1076 of the length change of the TCR–pMHC structure relative to its bound state during dissociation.
1077 Subtraction of this work from the interaction free energy tilts the energy landscape that governs the
1078 off-rate (Eq. 1, Fig. 1b). To calculate molecular stretch, we assume the TCR–pMHC complex to
1079 behave as a system of semi-rigid bodies of globular domains connected by semi-flexible polymers
1080 (Fig. 2b). As such, the total length change includes three components: 1) extension of individual
1081 globular domains, 2) various domain rotations about hinges, and 3) unfolding of secondary
1082 structures at specific regions.

1083 For a globular domain without unfolding, the force-extension relationship is described by
1084 the three-dimensional freely-jointed chain model[1]:

$$d_{\mathrm{i}}(f) = d_{\mathrm{i,c}}\left\{\coth\left[f d_{\mathrm{i,c}}/k_{\mathrm{B}}T\right] - \frac{k_{\mathrm{B}}T}{f d_{\mathrm{i,c}}}\right\}\left(1 + \frac{f}{E_{\mathrm{d}}}\right), \qquad \textbf{[S1]}$$

1085 where d_{i} is end-to-end distance of the ith-domain, k_{B} is the Boltzmann constant, T is absolute
1086 temperature, f is force, and E_{d} ~ 100 pN is the elastic modulus of the folded globular domain[2]. The
1087 present work considers domain extension of the whole TCR–pMHC-I complex (d_{N}) and three of
1088 its parts: the MHC α_3 domain ($d_{\alpha 3}$), bonding interface that includes the MHC $\alpha_1\alpha_2$ domains bound
1089 to the TCR Vαβ domains ($d_{\mathrm{B.I}}$), and the TCR Cαβ domains ($d_{\mathrm{C}\alpha\beta}$). Their contour lengths, $d_{\mathrm{i,c}}$,
1090 have well-defined values depending on the TCR–pMHC complex in question, which are
1091 summarized in Supplementary Table 1. For example, $d_{\mathrm{N,c}}$ = 12.7 and 10.9 nm for 2C TCR

complexed with H2-K^b (PDB codes 2CKB, 1MWA, and 1G6R) and H2-L^{d}m31 (2E7L), respectively, and 12.3 nm for 1G4 TCR complexed with HLA-A2 (2BNR and 2BNQ). 12.5 nm for NP1-B17 TCR complexed with H2-D^b. We also choose 11.6 nm as a reasonable guess value for the N15 TCR/OT1 TCR –p:H2-K^b complex (because average $d_{\mathrm{N,c}}$ across 33 structures of TCR-pMHC class I complexes is 11.6 ± 1 nm (mean ± sd)[3]).

To calculate the work $\delta_1\gamma(F)$, we project the above domain extensions onto the direction of force, which is taken as the z direction (Fig. 2b) using two angles between the z axis and: 1) the normal direction of the bonding interface (θ) and 2) the line connecting the C- and N-termini of the MHC-I α_3 domain excluding any unfolded residues (φ):

$$z_{\mathrm{N}}(f) = d_{\mathrm{N}}(f) \qquad \textbf{[S2a]}$$

$$z_{\alpha 3}(f) = \sqrt{d_{\alpha 3}^2(f) - \left\{\left[d_{\mathrm{N}}(f) - d_{\mathrm{C}\alpha\beta}(f)\right]\sin\theta - d_{\alpha 3}(f)\sin(\varphi+\theta)\right\}^2}\,, \qquad \textbf{[S2b]}$$

$$z_{\mathrm{B.I}}(f) = d_{\mathrm{B.I}}(f) \equiv \left[d_{\mathrm{N}}(f) - d_{\mathrm{C}\alpha\beta}(f)\right]\cos\theta - d_{\alpha 3}(f)\cos(\varphi+\theta)\,, \qquad \textbf{[S2c]}$$

$$z_{\mathrm{C}\alpha\beta}(f) = d_{\mathrm{C}\alpha\beta}(f)\,. \qquad \textbf{[S2d]}$$

Note that θ is a model parameter as it describes the tilting of the bonding interface as part of the force-induced conformational change, whereas φ is a model constant is measured from the crystal structure (Supplementary Table 1, see A.2 below).

We assume that partial unfolding in the molecular complex may occur at connecting regions of globular domains, in particular, the $\alpha_1\alpha_2$–α_3 joint of the MHC-I and the Vα-Cα interdomain joint of the TCR (Fig. 2a). The former may be caused by dissociation of the noncovalent $\alpha_1\alpha_2$–β_{2m} interdomain bond, which shifts the mechanical load originally borne by this bond to the $\alpha_1\alpha_2$–α_3 hinge, resulting in its partial unfolding, as observed in SMD simulations[4] (Fig. 2a). Similarly, $\alpha_1\alpha_2$–β_{2m} dissociation results in tilting of the bonding interface and load shifting from the Vβ-Cβ joint to the Vα–Cα joint, leading to partial unfolding of the latter joint (Fig. 2a). The unfolded polypeptides

1111 are flexible and can bear only tension but not moment, ensuring that their extension is along the
1112 direction of force, i.e., the z axis.

1113 The force-extension relationship of the unfolded polypeptides can be described by an
1114 extensible worm-like chain (eWLC) model[5]:

$$\frac{f l_{\mathrm{p}}}{k_{\mathrm{B}} T} = \frac{1}{4\left(1 - z_{\mathrm{p}}/(n l_{\mathrm{c}})\right)} - \frac{1}{4} + \frac{z_{\mathrm{p}}}{n l_{\mathrm{c}}} - \frac{f}{K_{\mathrm{p}}} + \sum_{\mathrm{j}=1}^{\mathrm{j}\leq 7} a_{\mathrm{j}} \left(\frac{z_{\mathrm{p}}}{n l_{\mathrm{c}}} - \frac{f}{E_{\mathrm{p}}}\right)^{\mathrm{j}}, \qquad \textbf{[S3]}$$

1115 where z_{p} is the extension of the unfolded coil under force with the subscript p indicating
1116 unstructured polypeptide, $l_{\mathrm{c}} = 0.36$ nm and $l_{\mathrm{p}} = 0.39$ nm are the average contour length and
1117 persistence length per unfolded amino acid, respectively[6,7,8], $E_{\mathrm{p}} \sim 50$ μN is the elastic modulus of
1118 polypeptides[8], a_{j} are polynomial coefficients for the improved approximation, and n is the number
1119 of constituent amino acids in the unfolded polypeptide. In particular, we denote the respective
1120 numbers of amino acids in the unfolded MHC-I $\alpha_1\alpha_2$–α_3 and TCR Vα-Cα joints to be $n_{\mathrm{p,MHC}}$ and
1121 $n_{\mathrm{p,TCR}}$. Eq. S3 defines z_{p} as a function of *f*, which can be solved numerically to express in an
1122 explicit form: $z_{\mathrm{p}}/n l_{\mathrm{c}} = z_{\mathrm{u,p}}(f)$ = the extension per unit contour length for the polypeptide under
1123 force *f*.

1124 Thus, the length of the TCR–pMHC complex at the transition state is (Fig. 2b):

$$z(f) = z_{\alpha 3}(f) + n_{\mathrm{p,MHC}} l_{\mathrm{c}} z_{\mathrm{u,p}}(f) + z_{\mathrm{B.I}}(f) + n_{\mathrm{p,TCR}} l_{\mathrm{c}} z_{\mathrm{u,p}}(f) + z_{\mathrm{C}\alpha\beta}(f) \qquad \textbf{[S4]}$$

1125 Since we do not have prior knowledge about either number of unfolded amino acids, we will
1126 evaluate their sum $n^* = n_{\mathrm{p,TCR}} + n_{\mathrm{p,MHC}}$ from curve-fitting of our model to the experimental data
1127 (see below). Since $d_{\mathrm{N}}(f)$ is the length of the TCR–pMHC complex at the bound state (Fig. 2b), we
1128 have $z(f; 0) = d_{\mathrm{N}}(f)$. Finally, the integrand on the right-hand side of Eq. 3 can be written as

$$\delta_{\mathrm{z}}(f) = z_{\alpha 3}(f) + z_{\mathrm{B.I}}(f) + z_{\mathrm{C}\alpha\beta}(f) + n^* l_{\mathrm{c}} z_{\mathrm{u,p}}(f) - d_{\mathrm{N}}(f). \qquad \textbf{[S5]}$$

1129 ***A.2. Simplifying assumptions and reducing parameters***

1130 The purpose of this subsection is to provide the details omitted in the main text of how the
1131 model parameters are reduced to the smallest possible set and the underlying simplifying

1132 assumptions. To begin, we take the φ values from PDB for the specific TCR–pMHC interactions
1133 in question (Supplementary Table 1). Due to their small range ($5° \leq \varphi \leq 23.5°$), we assume that
1134 the φ value remains constant during forced dissociation (*e.g.*, φ = 12.7° and 5° for 2C TCR
1135 complexed with H2-K^b (PDB codes 2CKB, 1MWA, and 1G6R) and H2-L^{d}m31 (2E7L),
1136 respectively, and 13.3° for 1G4 TCR complexed with HLA-A2 (2BNR and 2BNQ). 15° for NP1-
1137 B17 TCR complexed with H2-D^b. We also choose 23.5° as a reasonable guess value for the N15
1138 TCR/OT1 TCR –p:H2-K^b complex). Additionally, due to the semi-rigid approximation, the
1139 thickness of the constant domain of TCR α- and β-subunit ($d_{C\alpha\beta}$) is also treated as constant for each
1140 construct (Supplementary Table 1). This leaves only two structural parameters ($d_{\alpha 3}$, θ) in our
1141 model to be evaluated by curve-fitting to data. Noting that the structure-based force function
1142 $\gamma(F;\delta_l)$ scales with the characteristic extension change per unit change of molecular length such
1143 that $\delta_l\gamma(F) = \int_0^F \delta_z(f)df$, the dissociation rate of TCR–pMHC-I bond can be written as:

$$k(F) = k_0\sqrt{1-\frac{2\int_0^F \delta_z(f)df}{3\Delta G_0^*}}\, e^{\frac{\Delta G_0^*}{k_B T}\left(1-\left(1-\frac{2\int_0^F \delta_z(f)df}{3\Delta G_0^*}\right)^{3/2}\right)}, \qquad \textbf{[S6]}$$

1144 where $\delta_z(f)$ is given by Eq. S5.

1145 To further reduce model parameters, we make additional assumptions as discussed in the
1146 main text. It is well-known that the fractions of free-energy change in biological interactions in
1147 liquid, such as unfolding and refolding of proteins, unbinding and rebinding of receptor–ligand
1148 bonds, and unzipping and rezipping of RNA or DNA, are small because of their limited dynamic
1149 transition time[9-12]. Such a rate limit results from the nature of biological interactions, *e.g.*,
1150 polar/non-polar interactions, hydrophobic interactions, and charged interactions, which typically
1151 yield finite range of transition kinetics. This enables to roughly estimate the free-energy barrier as
1152 $\Delta G_0^* \sim \ln(k_w/k_0)$ where $k_w \sim 10^6$ s^{-1} known as the prefactor[9-12].

1153 ***A.3. Defining the dissociation coordinate***

The purpose of this subsection is to derive an operational way to determine the dissociation coordinate variable δ_l used in the main text. We note that the total number of unfolded amino acids n^* is zero at the bound state before unfolding occurs, increases monotonically during progressive unfolding along the dissociation path, and reaches maximum at the dissociation point. Because n^* is not known *a priori*, it must be treated as a fitting parameter similar to $d_{\alpha 3}$, θ, and δ_0^*. Since δ_l is the contour length change along the dissociation path, we wish that δ_l approaches its upper bound δ_0^* and depends on force implicitly through the model parameters n^*, $d_{\alpha 3}$, and θ, as given below:

$$\delta_l = n^* l_c + \Delta(d_{\alpha 3}, \theta) \rightarrow \delta_0^*, \qquad \textbf{[S7]}$$

where $\Delta(d_{\alpha 3}, \theta)$ is the difference of the contour lengths except for the partially unfolded regions. Thus, Eq. S7 provides a constraint for δ_l instead of introducing another model parameter. $d_{\alpha 3}$ and θ are determined for each n^* during the model fitting that searches for parameters to enable $\delta_l \rightarrow \delta_0^*$. Small errors, which may occur for the various contributions to Δ (red lines in Fig. 2a labeled as force transmission lines), can be identified using a pair of $(d_{\alpha 3}, \theta)$ values and the crystal structure for each complex. Specifically, average differences $\langle\Delta\rangle$ are - 0.9 nm for the strong catch bond (SC) group ($d_{\alpha 3} > 3$ nm, $\theta > 20°$), 0.4 nm for the weak catch bond (WC) group (1 nm $< d_{\alpha 3} <$ 3 nm, 5°$< \theta <$ 20°), and 0 nm for slip-only bond (SO) group ($d_{\alpha 3} <$ 1 nm, $\theta <$ 5°), respectively (see Fig. 4e-i and associated text for the definitions of SC, WC, and SO groups). It has been well established that the contour length of a single amino acid is $\sim 0.4 \pm 0.02$ nm/a.a[6,13,14], implying that the model has a resolution of 3 amino acids. We further note that, even without conformational change, it is possible for the slip-only bond group to have 3 unfolded amino acids due to the limited resolution of the model. Finally, the best-fit model parameters can be determined by finding the subset of best-fit parameters among possible n^* values that match the contour length change δ_l to the free-energy well width at zero-force δ_0^*, *i.e.*, finding n^* such that $\delta_l(n^*, d_{\alpha 3}, \theta) \rightarrow \delta_0^*$ (see Supplementary Table 2). Under this condition, $\int_0^F \delta_z(f)df = \delta_l \gamma(F) \rightarrow \delta_0^* \gamma(F)$ and Eq. S6 becomes identical to Eq. 2.

A.4. Model applications, curve-fitting strategies, and biological relevance

The purpose of this subsection is to outline the procedures of applying our model to experiments. Our procedures include four steps: 1) examine how the model parameters control the model behaviors, 2) fit the model-predicted reciprocal off-rate (Eq. S6) to the experimental bond lifetime *vs* force data, 3) construct the energy landscape and investigate its properties based on the parameters evaluated in part 2, 4) elucidate the biological relevance of the model parameters.

To examine how the model parameters control the model behaviors, we varied one parameter while keeping others constant. For example, to investigate the effect of varying the titling angle θ, we kept the other parameters constants (*i.e.*, $n^* = 7$, and $\delta_0^* = 2$ nm, $k_0 = 3$ s^{-1} and $\Delta G_0^* = 12.7\ k_{\mathrm{B}}T$), Also kept constant were several structural constants ($\varphi = 15°$, $d_N = 12$ nm and $d_{\mathrm{C\alpha\beta}} = 3.5$ nm) introduced in section A.1. Of note, $d_{\alpha 3}$ varies as θ changes because of a pulling constraint (see section B.1). With a fixed θ (*i.e.*, 30°) the effect of molecular extension at zero force was investigated by varying extension from 0.5-3.5 nm. These were selected by the average values of actual fitting results, which had been tested and confirmed as reasonable.

The free-energy landscape can be constructed by substituting the best-fit model parameters into the following equations[13]:

$$\Delta G^*(F) = \Delta G_0^* \left(1 - \frac{2\delta_0^* \gamma(F)}{3\Delta G_0^*}\right)^{3/2},$$

$$\delta^*(F) = \delta_0^* \left(1 - \frac{2\delta_0^* \gamma(F)}{3\Delta G_0^*}\right)^{1/2}, \qquad \textbf{[S8a,b]}$$

Thus, by using model parameters, the dissociation state coordinates relative to the bound state coordinates in the free-energy *vs* dissociation coordinate space can be defined as functions of force. Note that this force-induced change of the barrier height should be under the condition of small perturbation such that $|-\delta_0^* \gamma(F)| < \Delta G_0^*$. Since our fitting results show that the average free-energy barrier height at zero force is ~12 $k_{\mathrm{B}}T$ ($\langle \Delta G_0^* \rangle$), the force range corresponding to a change of the barrier height of <10 $k_{\mathrm{B}}T$ is reasonable for each dataset, *i.e.,* force range corresponding to energy barrier heights in the range of 2 $k_{\mathrm{B}}T < \Delta G_0^* < 22\ k_{\mathrm{B}}T$.

1200 Firstly, to fit the model-predicted reciprocal off-rate (Eq. S6) to the experimental bond
1201 lifetime *vs* force data, all four parameters were changed simultaneously to search for the minimum
1202 of the chi squared error. Second, every fitting curve was then determined by the parameter set that
1203 has the closest δ_{l} value to δ_0^* (described as Eq. S7 in section A.3 and Supplementary Table 2).
1204 Fitting error of the best fit parameters could be calculated using standard error of mean of bond
1205 lifetime. Of the 50 datasets analyzed, only one has 4 data points and this dataset shows slip bond;
1206 as such, is governed by two fitting parameters because the other two parameters are nearly zero.
1207 All other datasets have 6-10 data points; therefore, over-fitting is not a problem.

1208 To elucidate the biological relevance of the model parameters θ, n^*, $d_{\mathrm{C\alpha\beta}}$, δ_0^*, and ΔG_0^*, we
1209 examine their changes with varying bond lifetime *vs* force data obtained from different TCR and
1210 pMHC interactions that induce a wide range of biological responses. Finding correspondence
1211 between a group of model parameters individually and/or collectively with the biological response
1212 would be considered as support for the biological relevance of the model, because such
1213 correspondence suggests that the model can discriminate different TCR–pMHC interactions that
1214 result in differential T cell functions.

1215 ***A.5. Class I model constraints***

1216 The purpose of this subsection is to check whether the model parameters obtained from data
1217 fitting are consistent with the constraints to which the model is subjected. Our experiments applied
1218 tensile force through the two ends of the TCR–pMHC complex, such that the force direction would
1219 always align with the line connecting the C-termini of the respective TCR and MHC molecules
1220 during dissociation, giving rise to the so-called pulling constraint. To formulate this pulling
1221 constraint in our model, we note that the pulling line is maintained so that the coordinate
1222 perpendicular to the force direction is invariant. As depicted in Supplementary Fig. 4a, several angle
1223 and length variables can be related using model parameters and structural constants by:

$$\left(d_N - d_{\mathrm{C\alpha\beta}} - d_{\alpha 3}\frac{\cos(\varphi+\theta)}{\cos\theta}\right)\sin\theta = d_{\alpha 3}\left(\frac{\sin\varphi}{\cos\theta} + \cos\left(2\psi + \varphi + \theta - \frac{\pi}{2}\right)\right), \qquad \textbf{[S9a]}$$

where ψ is the angle in an isosceles triangle constructed by rotating the α3 domain. By assuming that the α3 domain would be aligned with force, we estimate that the angle in the last term is near 90°, *i.e.*, $2\psi + \varphi + \theta - \frac{\pi}{2} \approx \frac{\pi}{2} - \delta$ where $\delta \ll \frac{\pi}{2}$. Under this small angle assumption, Eq. S9a can be approximated by:

$$d_{\alpha 3} \approx \frac{d_N - d_{\mathrm{C\alpha\beta}}}{\cot\theta\sin\varphi + \cos\varphi + \sin\delta/\sin\theta}. \qquad \textbf{[S9b]}$$

Upon inversing Eq. S9b, we found that the tilting angle θ is a function of the end-to-end distance of the α3 domain, *i.e.,* $\theta = f(d_{\alpha 3})$. Setting $\delta = 25°$, which seems reasonable as it approximates the maximum value of φ, the structural parameters obtained by fitting are scattered in-between two black curves on the $d_{\alpha 3} - \theta$ plane marked as pulling constraint: [d_N = 12.5 nm, $d_{\mathrm{C\alpha\beta}}$ = 3.62 nm, $\varphi = 0°$] and [d_N = 11.5 nm, $d_{\mathrm{C\alpha\beta}}$ = 3.42 nm, $\varphi = 25°$]) (Fig. 4f).

Another constraint is the tilting constraint resulted from the asymmetric unfolding and stretching of the interdomain links between the TCR constant and variable domains. This constraint is introduced in the model to account for the potential regulatory effect of the FG-loop on catch bond. Notwithstanding the total number of unfolded amino acids n^* can be determined by the validation procedure demonstrated in A.2, its breakdown into the number of unfolded amino acids for MHC ($n_{\mathrm{p,MHC}}$) and TCR ($n_{\mathrm{p,TCR}}$) remains undetermined. To do this, known structures from *PDB* were used to determine $n_{\mathrm{p,MHC}}$ first. Briefly, by matching $d_{\alpha 3}$ (Supplementary Fig. 4b, c) with the end-to-end distance between C-terminal end of α3 domain and certain point following known *PDB* structure, the exact starting position of partial unfolding in MHC can be found following additional assumption that unfolding starts from C-terminal end of α2 domain towards α3 domain (Supplementary Fig. 4b). Thus, $n_{\mathrm{p,TCR}}$ can be simply calculated as $n_{\mathrm{p,TCR}} = n^* - n_{\mathrm{p,MHC}}$. Upon combining all information, the tilting angle (θ_{TCR}) of variable domains of TCR can be described by simple trigonometrical function:

$$\theta_{\mathrm{TCR}} \approx \tan^{-1}\left(\frac{n_{\mathrm{p,TCR}} l_{\mathrm{c}}}{W_{\mathrm{TCR}}}\right), \quad \textbf{[S10]}$$

where W_{TCR} is width of two interdomain hinges of the TCR α- and β-subunits measured from the crystal structures (Supplementary Fig. 4a, tilting constraint). In this work we use $W_{\mathrm{TCR}} = 3.7 \pm 0.3$ nm as a representative width due to structure-to-structure variations. Thus, by comparing the tilting angle of the bonding interface θ (model parameter) to the tilting angle of the TCR θ_{TCR} (derived from another model parameter $n_{\mathrm{p,TCR}}$ and structural constants W_{TCR} and l_{c}), we can check the validity of tilting constraint using linear regression in the θ *vs* θ_{TCR} plot (Supplementary Fig. 4d).

B. Kinetic model for TCR–pMHC-II bonds

B.1. Development, validation, and characterization

The purpose of this subsection is to present details of the development, validation, and characterization of the TCR–pMHC-II catch bond model omitted in the main text for simplicity, in a similar fashion as the TCR–pMHC-I catch bond model described in Section A. The two models share exact the same framework but have different detailed form of the characteristic extension change $\delta_{\mathrm{z}}(f)$ (Eq. S5). Comparing to the TCR–pMHC-I complex, the TCR–pMHC-II complex has different docking domains and pulling geometries (one *vs* two transmembrane domains on both TCR and MHC). For this reason, we assume that the force-induced bonding interface tilting angle (θ) would be much smaller in the TCR–pMHC-II than TCR–pMHC-I complex. The extension at the bound state can be defined as the end-to-end distance between both end-points identified by crystal structures (E8: 2IAM, 2IAN and 2B4 (as the substitution of 3.L2): 6BGA, 3QIB):

$$z(f;0) = d_{\mathrm{N}}(f) + d_{\mathrm{linker}}(f), \quad \textbf{[S11]}$$

where d_{N} is set to be 12.3 nm based on the crystal structures and $d_{\mathrm{linker}} \approx 9.4$ nm represents the linker (*e.g.*, a leucine zipper) engineered at the C-termini of soluble pMHC-II constructs to stabilize both the MHC α- and β-subunits, which is often used in experiments for measuring TCR–pMHC-II catch bonds. To account for domain rotation resulted from partial unfolding inside the TCR–

1270 pMHC-II complex, we introduce one more variable, φ, as the tilting angle of the TCR constant
1271 domains. Using the tilting constraint similarly to that used in the class I model, this angle can be
1272 approximately described by structural parameters ($d_{\mathrm{B.I}}$, θ) and model constants (see subsection B.2).
1273 In short, each component in the right-hand side of Eq. S11 can be expressed by the model
1274 parameters ($d_{\mathrm{B.I}}$, θ, n^*), and model constants as follows.

$$z_{\mathrm{B.I}}(f) = \left(d_{\mathrm{B.I}}(f) + z_{\mathrm{p,MHC}}(f)\right)\cos\theta\ , \qquad \textbf{[S12a]}$$

$$z_{\mathrm{C\alpha\beta}}(f) = \left(d_{\mathrm{C\alpha\beta}}(f) + z_{\mathrm{p,TCR}}(f)\right)\cos\varphi\ , \qquad \textbf{[S12b]}$$

$$z_{\mathrm{linker}}(f) = d_{\mathrm{linker}}(f)\cos\theta\ , \qquad \textbf{[S12c]}$$

1275 where $z_{\mathrm{p,MHC}}(f)$ and $z_{\mathrm{p,TCR}}(f)$ are respective extensions of unfolded polypeptides given by
1276 $n_{\mathrm{p,MHC}} l_{\mathrm{c}} z_{u,p}(f)$ and $n_{\mathrm{p,TCR}} l_{\mathrm{c}} z_{u,p}(f)$, respectively, $d_{\mathrm{B.I}}$ is the length of structure consisting of the
1277 MHC and the TCR variable domains, and other parameters defined previously. Finally, the rate
1278 coefficient of the TCR–pMHC-II dissociation can be developed by employing the same framework
1279 (see Eq. S6). However, when applying the model to experimental data, we can use the constraints
1280 of the TCR–pMHC-II interaction to make the model much simpler (see section B.2).

1281 Validation of the class II model follows exactly the same procedure as that used in the
1282 validation of the pMHC I model, which is done by checking self-consistent through the definition
1283 of the reaction coordinate. By varying the $n_{\mathrm{p,MHC}}$ from 0 to 10 (see details explained in section B.2),
1284 the molecular extension at zero force (δ_0^*) can be estimated by using the contour length-change (δ_{l})
1285 along the dissociation coordinate:

$$\delta_{\mathrm{l}} = n_{\mathrm{p,MHC}} l_{\mathrm{c}} + \Delta \rightarrow \delta_0^* \qquad \textbf{[S13]}$$

1286 where $\Delta(d_{\mathrm{B.I}}, \theta) < 0.2$ nm because $\theta < 10°$. The best-fit model parameters can be determined by
1287 finding a subset of best-fit parameters among possible $n_{\mathrm{p,MHC}}$ values that match the contour length-

1288 change along the dissociation coordinate (δ_1) to the width of the free-energy well at zero force (δ_0^*),
1289 *i.e.*, finding $n_{\mathrm{p,MHC}}$ such that $\delta_1(n_{\mathrm{p,MHC}}) \to \delta_0^*$ (see Supplementary Table 5).

1290 To characterize the class II model, we examine the model predictions by varying the model
1291 parameters one by one while fixing the others as constants. For example, to investigate force-
1292 induced bonding interface titling, we fixed the other model parameters (*i.e.*, $n^* = 4$, $\delta_0^* = 1.2$ nm,
1293 $k_0 = 10$ s^{-1}, and $\Delta G_0^* = 11.5\ k_{\mathrm{B}}T$) and structural constants ($d_{\mathrm{N}} = 12$ nm, $d_{\mathrm{B.I}} = 12.3$ nm, and
1294 $d_{\mathrm{linker}} = 9.4$ nm for pMHC-II constructs that have linkers). As another example, we fixed $\theta = 0°$
1295 or 3° and examined the effect of the molecular extension at zero force by varying δ_0^* from 0.3-1.8
1296 nm. The constants used for model characterization were selected by their averages from the
1297 corresponding values used to fit actual experiments. The parameters for free-energy landscape
1298 construction, the energy barrier height (ΔG^*) and energy well width (δ^*) as functions of force, are
1299 given by Eq. S8, exactly the same as the pMHC I model.

1300 Fitting of class II model to experimental data and examination of the biological relevance
1301 of the best-fit parameters were done the same way as the class I model.

1302 ***B.2. Class II model constraints***

1303 The purpose of this subsection is to describe the constraints of the class II model, which
1304 share similar ideas to those of the class I model (*e.g.*, pulling and tilting constraints) but differ in
1305 their specific expressions. To formulate the pulling constraint, we again used the fact that the pulling
1306 force direction must aligns with the line connecting to the C-termini of the TCR and pMHC
1307 molecules so that the coordinate perpendicular to the force direction is invariant. Using model
1308 parameters and structural constants, this pulling constraint can be written as:

$$\left(d_{\mathrm{B.I}} + z_{\mathrm{p,MHC}} + d_{\mathrm{linker}}\right)\sin\theta = \left(d_{\mathrm{C\alpha\beta}} + z_{\mathrm{p,TCR}}\right)\sin\varphi\ , \qquad \textbf{[S14a]}$$

1309 which can be solved for $z_{\mathrm{p,TCR}}$ explicitly:

$$z_{\mathrm{p,TCR}} = \left(d_{\mathrm{B.I}} + z_{\mathrm{p,MHC}} + d_{\mathrm{linker}}\right)\frac{\sin\theta}{\sin\varphi} - d_{\mathrm{C\alpha\beta}} \ . \qquad \textbf{[S14b]}$$

By combining Eq. S12 and S14, the total extension (z) can be calculated as the sum of all component extensions ($\sum_i z_i$) at dissociation ($\delta_l > 0$):

$$z(f;\delta_l) = \left(d_{\mathrm{B.I}}(f) + z_{\mathrm{p,MHC}}(f) + d_{\mathrm{linker}}(f)\right)(\cos\theta + \sin\theta\cot\varphi) \ . \qquad \textbf{[S15]}$$

This equation states that only the number of unfolded amino acids in MHC ($n_{\mathrm{p,MHC}}$) affects extension change during transition. The total number of unfolded amino acids from both TCR and MHC can be estimated by Eq. S14b:

$$n^* \approx \left|\frac{(d_{\mathrm{B.I}}+d_{\mathrm{linker}})\frac{\sin\theta}{\sin\varphi} - d_{\mathrm{C\alpha\beta}}}{l_{\mathrm{c}}} + \left(1 + \frac{\sin\theta}{\sin\varphi}\right)n_{\mathrm{p,MHC}}\right| \ . \qquad \textbf{[S16]}$$

which can be approximately calculated using contour lengths of length components at force-free state.

By assuming small angle perturbation, which seems reasonable, we further reduce the number of model parameters after relating the tilting angle of the TCR constant domain (φ) and the titling angle of the bonding interface by the following equation:

$$\cot\varphi \approx \frac{d_{\mathrm{N}} - d_{\mathrm{B.I}}}{d_{\mathrm{B.I}} + d_{\mathrm{linker}}}\cot\theta \ . \qquad \textbf{[S17]}$$

Thus, all terms including φ can be re-expressed by using Eq. S17.

Additionally, the tilting constraint can be expressed as follows:

$$\frac{\tan^{-1}\left(\frac{n_{\mathrm{p,TCR}} l_{\mathrm{c}}}{W_{\mathrm{TCR}}}\right)}{\theta+\varphi} \approx 1 \ . \qquad \textbf{[S18]}$$

Thus, by using Eq. S15 and S17, only 4 fitting parameters, two structural parameters ($d_{\mathrm{B.I}}$, θ) and two biophysical parameters (k_0, δ_0^*), were used to fit the class II model to data.

C. A general biophysical limit of model parameters

The purpose of this section is to describe a general biophysical limit that constrains the fitted model parameters, which is used in Fig. 6 to accept the correct model application to data of matched MHC class and reject incorrect model application to data of mismatched MHC class. The idea is

that, even if the model is capable of fitting experimental data and the parameters are self-consistent with one another within the model, their values should be within known limits. A prototypical example of such a biophysical limit involves the molecular extension per unfolded amino acids. It follows from Eqs. S7 and S13 that the average molecular extension at zero force over all data ($\langle\delta_0\rangle$) should be a linear function of n^* such that $\langle\delta_0\rangle = an^* + b$. The y-axis intercept b can be determined from the slip bond data because slip bonds are not expected to have unfolded amino acids (i.e., $n^* = 0$) but still have a nonzero extension. The slope a is constrained by the fact that the contour length of a single amino acid has a small range (~0.4 ± 0.02 nm/a.a.)[6,13,14]; thus, the average molecular extension ($\langle\delta_0\rangle$) per unfolded amino acid should be bounded by:

$$0 < a < 0.4\ . \qquad \textbf{[S19]}$$

Imposing this range limit of $\langle\delta_0\rangle$/a.a. would enable us to rule out inappropriate application of the model even if such application could achieve reasonable level of goodness-of-fit. An exceedingly large value of a ($>$ 0.4 ± 0.02 nm/a.a.) estimated by the model would mean that the model is inappropriate for the data.

Conversely, a nearly zero estimate of a would indicate that the model is inappropriate for catch-slip bond data because, for the model to fit catch-slip bonds, it requires $n^* > 0$ (see Figs. 2c-g and 3f, *middle row*). A parameter estimation of $a \approx 0$ indicates the lack of dependence of the model behavior on n^*, which abolishes the model's ability to predict TCR signaling and antigen discrimination, making the model irrelevant to biology.

The sturdier class II than class I pMHC structure also precludes large rotation during conformational change at transition state, leaving only unfolding and stretching along the force. Thus, the average molecular extension per amino acid should be close to 0.4 nm/a.a. On the other hand, $a \approx 0$ is expected from fitting the slip-only data because such data correspond to the $n^* = 0$ case, which makes it difficult to robustly estimate the correct a value. Thus, the average molecular extension per amino acid should be well-correlated with each other (high level of goodness-of-fit

as measured by R^2) and in the range between 0 to 0.4 nm/a.a. In Fig. 6, we used these criteria to test the appropriateness of cross-applying the class I model to class II data and *vice versa*, showing that it is appropriate to use either model to fit matched data but inappropriate to use either model to fit mismatch data.

1358 **Supplementary Figures**

1359

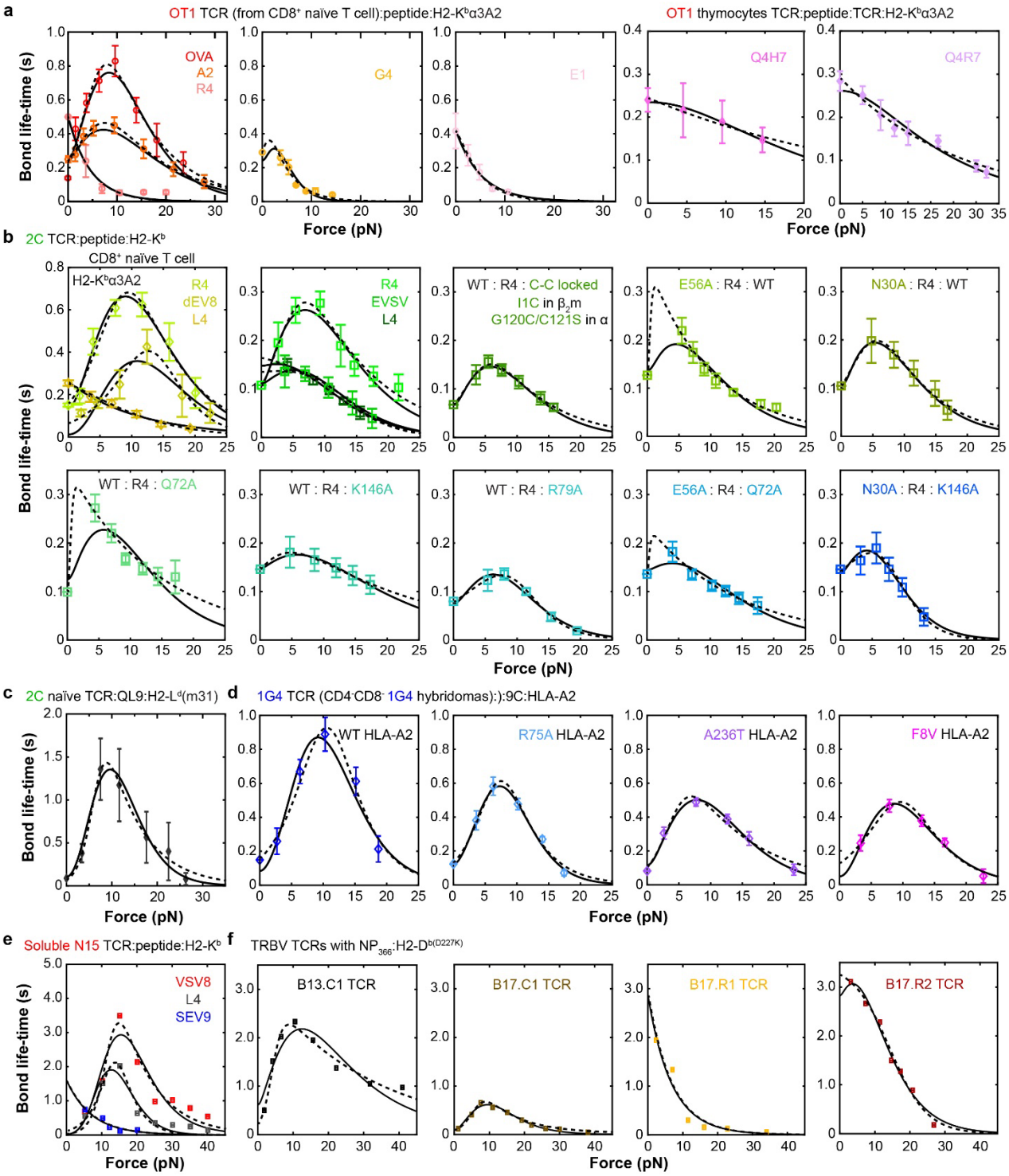

1360

1361 **Supplementary Figure 1 | Fitting class I model and two-pathway model to data of TCR–**

1362 **pMHC-I bond lifetime *vs* force. a-f** Fitting of theoretical $1/k(F)$ curves of the class I model

1363 (solid curves) and the two-pathway model (dashed curves) to experimental bond lifetime *vs* force

1364 data (*points*, mean ± sem) of 5 TCRs and their mutants interacting with different pMHCs as

1365 described below (re-analyzed from Refs.[4,15,16,17,18]). (**a**) OT1 TCR expressed on $CD8^+$ naïve T
1366 cells (first three panels) or $CD4^+CD8^+$ thymocytes (last two panels) interacting with indicated
1367 p:H2-K^bα3A2. (**b**) 2C TCR expressed on $CD8^+$ naïve T cells interacting with indicated p:H2-
1368 K^bα3A2 (*top*, 1st panel) or on $CD8^-$ hybridomas interacting with indicated peptides presented by
1369 WT (*top*, 2nd panel) or disulfate-locked MT (*top*, 3rd panel) H2-K^b, 2C TCR with indicated point
1370 mutations expressed on $CD8^-$ hybridomas interacting with R4:H2-K^b (*top*, 4th and 5th panels), 2C
1371 TCR expressed on $CD8^-$ hybridomas interacting with R4 peptide presented by H2-K^b with
1372 indicated point mutations (*bottom*, 1st-3rd panels), or 2C TCR with indicated point mutations
1373 expressed on $CD8^-$ hybridomas interacting with R4 peptide presented by H2-K^b with indicated
1374 point mutations (*bottom*, 4th and 5th panels). (**c**) 2C TCR expressed on $CD8^+$ naïve T cells
1375 interacting with indicated p:H2-L^d(m31) with truncated α3 domain. (**d**) 1G4 TCR expressed on
1376 $CD8^-$ hybridomas interacting with indicated p:HLA-A2. The first panel of a and the first two top
1377 panels of b are replotted from **Fig. 3a** and **b** for completeness. (**e**) Purified N15 TCRαβ
1378 interacting with indicated p:H2-K^b. f, TRBV TCRs of canonical (B13.C1 and B17.C1) and
1379 reverse (B17.R1 and B17.R2) pMHC-I docking orientation expressed on hybridomas interacting
1380 with NP_{366}:H2-D^{bD227K}. See Supplementary Table 3 for a list of the interacting molecules.
1381

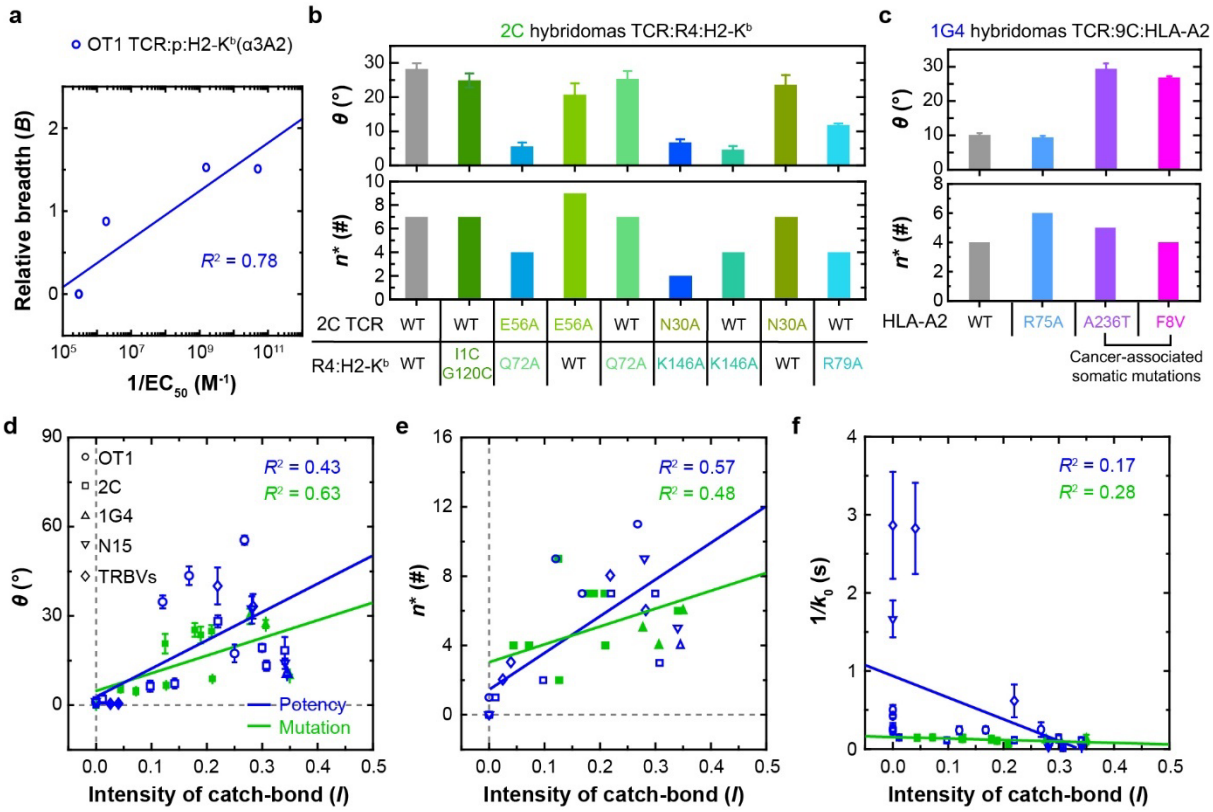

Supplementary Figure 2 | Correlation of model parameters with pMHC-I biological activity and TCR bond type. a Relative breadth *vs* the reciprocal peptide dose required to stimulate half maximal of OT1 T cell proliferation. **b-c** Model parameters $\boldsymbol{\theta}$ (the tilted angle of the bonding interface, *upper*) and $\boldsymbol{n}^*$ (the number of unfolded amino acids, *lower*) that best-fit the data in Supplementary **Fig. 1b** and **d** are plotted *vs* the indicated WT and mutant 2C (**b**) and 1G4 (**c**) TCRs with their indicated pMHCs. **d-f** Scattergrams of $\boldsymbol{\theta}$ (**d**), $\boldsymbol{n}^*$ (**e**), and $\mathbf{1}/\boldsymbol{k_0}$ (**f**) *vs* $\boldsymbol{I} = \boldsymbol{L}/(\mathbf{1}+\boldsymbol{B})$ (catch bond intensity) are plotted using the data from **Figs. 3e** & **3f**, **4b**, and **Supplementary Figs. 2b** & **2c** to examine correlation. Blue-open symbols indicate data of known T cell biological activities (ligand potencies) induced by the corresponding TCR–pMHC-I interactions that correlate to catch bond intensity. Green-closed symbols indicate data of known effects on catch bond metrics by targeted mutations on the TCR, MHC, or both. See Supplementary Table 3 for a list of the interacting molecules.

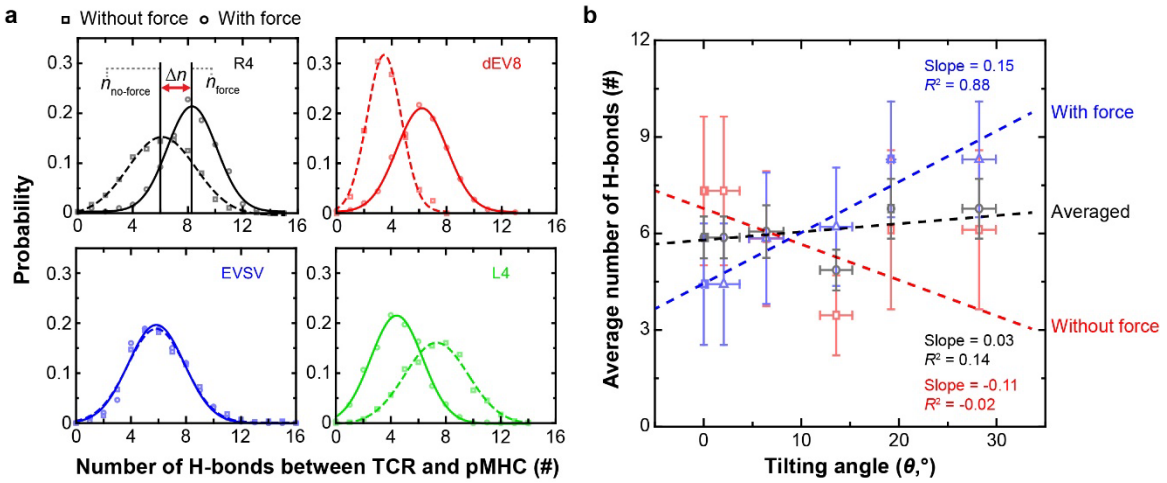

Supplementary Figure 3 | Correlation of force-induced TCR–pMHC-I hydrogen (H) bonds with bonding interface tilting angle. a H-bond distributions at bonding interface between 2C TCR and the indicated pMHCs (R4, dEV8, EVSV, or L4) in the presence (*solid curves*) or absence (*dotted curves*) of the force (obtained by re-analysis of SMD simulation results from Ref. [4] and fitted by Gaussian functions). **b** Plots of average number of H-bonds (mean ± sd) with respect to fitted tilting angle (with fitting error) of bonding interface in the absence (*red*) and presence (*blue*) of force as well as their average (*gray*). Average numbers of H-bonds were determined as mean value for each Gaussian distribution at each titling angle. All colored dashed lines are linear fits.

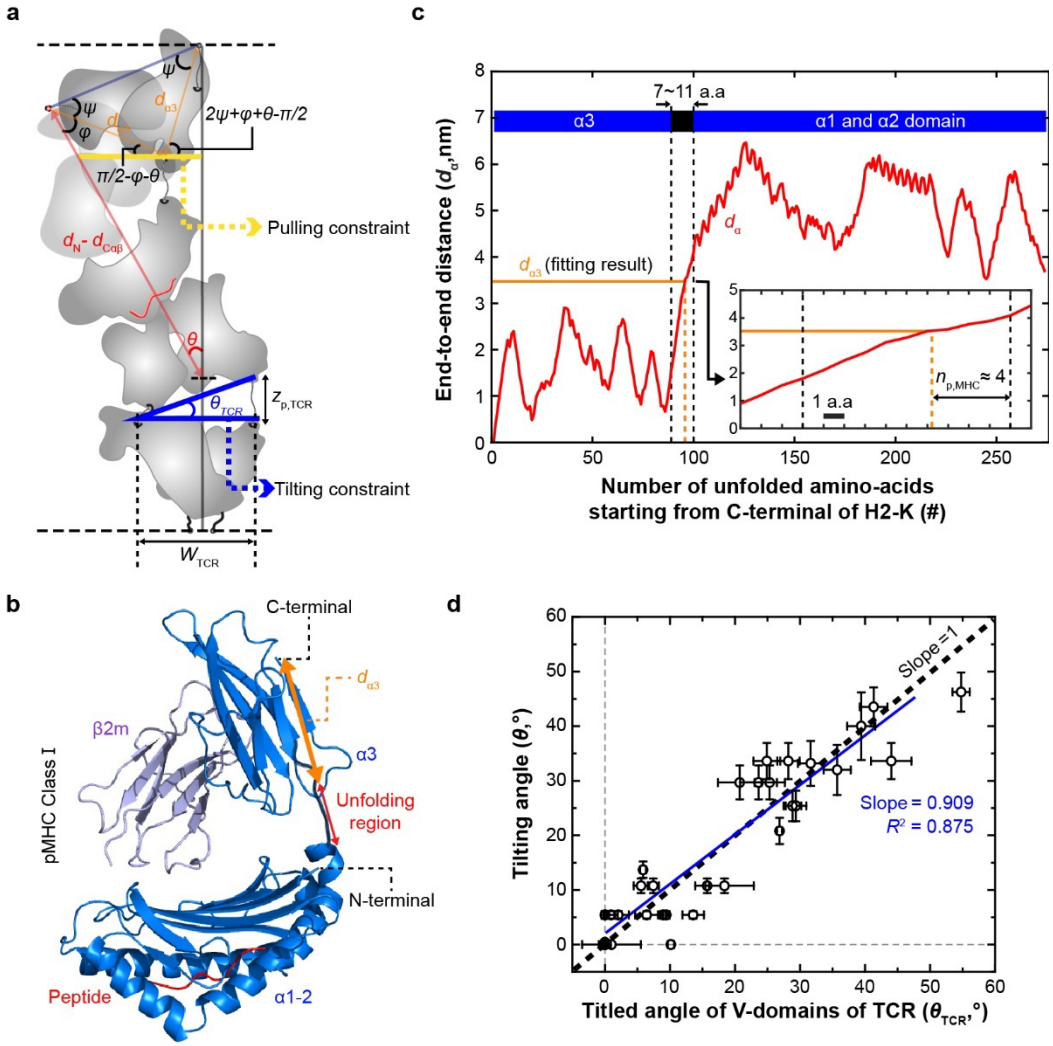

Supplementary Figure 4 | Pulling and tilting constraints of class I model. a An illustration of both pulling and tilting constraints. Length of yellow line was used to set up the equation of the pulling constraint between $\boldsymbol{d_{\alpha 3}}$ and $\boldsymbol{\theta}$. The tilted angle from the blue lines was used to check asymmetric stretching of TCR. **b** A pMHC-I structure based on PDB code 2CKB. Partial unfolding of MHC is assumed to start from the end of the α1-α2 domain towards the α3 domain as suggested by SMD simulation[4]. **c** Representative end-to-end distance of $\boldsymbol{d_{\alpha 3}}$ *vs* the number of unfolded amino acids. The distance is calculated from C-terminal end of the **α3** domain based on the structure shown in (**b**). Distance is calculated using the PBD structure for each construct. $\boldsymbol{d_{\alpha 3}}$ distance obtained from fitting the model to data is converted to $\boldsymbol{n_{\mathrm{p,MHC}}}$ (*inset*). **d** Tilted angle of the TCR variable domains ($\boldsymbol{\theta_{\mathrm{TCR}}}$) *vs* the titled angle of bonding interface ($\boldsymbol{\theta}$) as one of the fitting

parameters. The validity of asymmetric stretching of TCR was checked by the linear relationship between the two angles. All errors in (**d**) represent fitting errors.

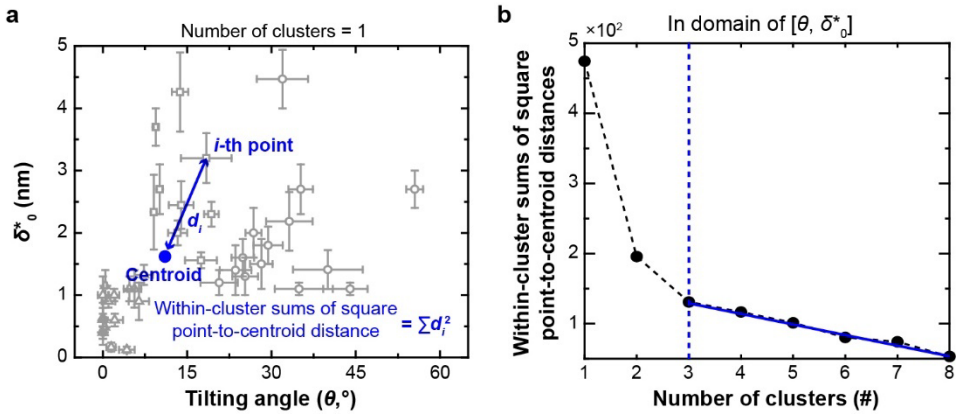

Supplementary Figure 5 | Determining the number of clusters in parameter space. a Definitions of the *i*-th point-to-centroid Euclidean distance (blue line) and of the within-cluster sums of square point-to-centroid distance when the number of clusters is 1. Scatters were replotted from **Fig. 4e**. **b** Sum of all squared Euclidean distances *vs* number of possible clusters. Point of abrupt reduction of steepness of slope leading to a straight line (*blue solid-line*) was identified a number of clusters (*blue dotted-line*).

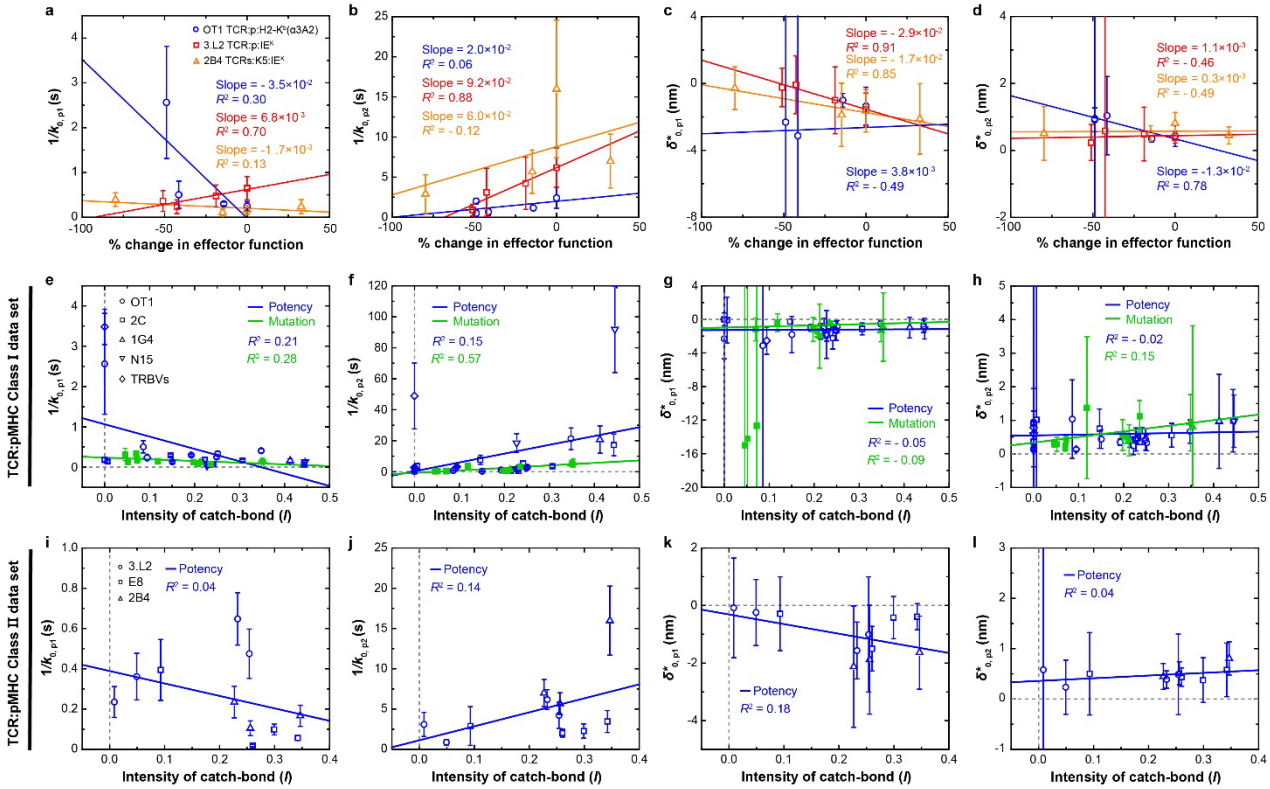

Supplementary Figure 6 | Lack of correlations between best-fit parameters of the two-pathway model and T cell function. a-d Correlation plots of $\mathbf{1/k_{0,p1}}$ (**a**), $\mathbf{1/k_{0,p2}}$ (**b**), $\boldsymbol{\delta^*_{0,p1}}$ (**c**), and $\boldsymbol{\delta^*_{0,p2}}$ (**d**) *vs* % changes in effector function. T cell effector function was defined by the peptide dose required to achieve half-maximal proliferation ($1/EC_{50}$) of OT1 T cells (*blue*) or to generate 40% B cell apoptosis ($1/EC_{40}$)[19] for 3.L2 T cells (*red*), or the area under the dose response curve (AUC) of 2B4 hybridoma IL-2 production[20] (*orange*). Color-matched solid lines are linear fits for the indicated TCR–pMHC systems. Also indicated are the slopes and R^2 values. **e-l** Correlation plots of $\mathbf{1/k_{0,p1}}$ (**e**, **i**) $\mathbf{1/k_{0,p2}}$ (**f**, **j**), $\boldsymbol{\delta^*_{0,p1}}$ (**g**, **k**), and $\boldsymbol{\delta^*_{0,p2}}$ (**h**, **l**) *vs* the intensity of catch bond evaluated from the indicated class I (**e-h**) or class II (**i-l**) datasets. Solid lines are linear fits, which are color-matched to indicate the 'potency-' or 'mutation-' related datasets for the class I system. All error bars are fitting error (Supplementary Table 4).

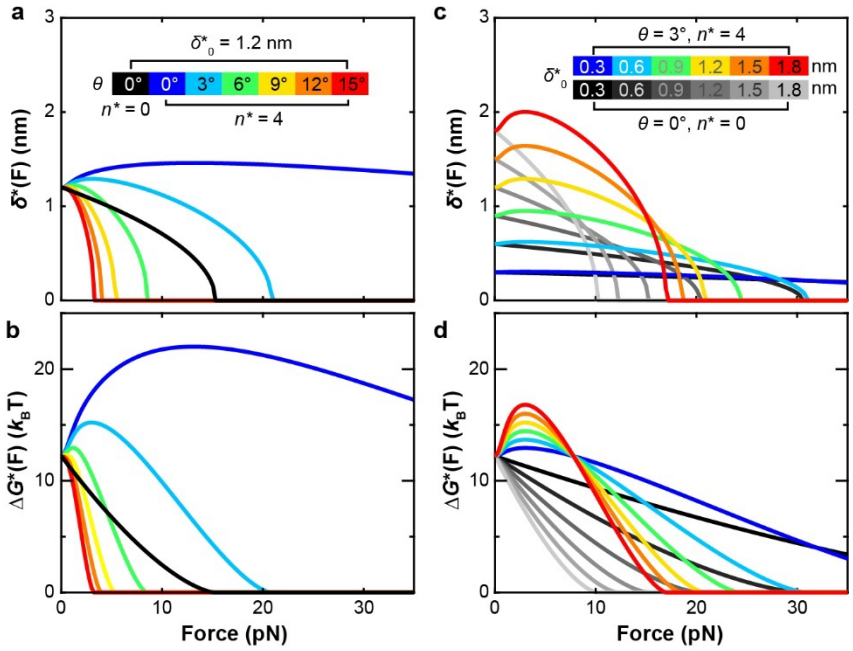

Supplementary Figure 7 | Characterization of the energy landscape of TCR–pMHC-II dissociation. a-d Plots of transition state location $\boldsymbol{\delta}^*$ (**a**, **c**) and height of energy barrier $\Delta\boldsymbol{G}^*$ (**b**, **d**) *vs* force $\boldsymbol{F}$ for changing $\boldsymbol{\theta}$ and $\boldsymbol{n}^*$ (**a**, **b**) or $\boldsymbol{\delta}_{\mathbf{0}}^*$ and $\boldsymbol{n}^*$ (**c**, **d**) while keeping $\boldsymbol{\delta}_{\mathbf{0}}^*$ = 1.2 nm (**a**, **b**) or $\boldsymbol{\theta}$ = 0, 3° (**c**, **d**). Inset color bars indicate parameter values used to plot the color-match theoretical curves.

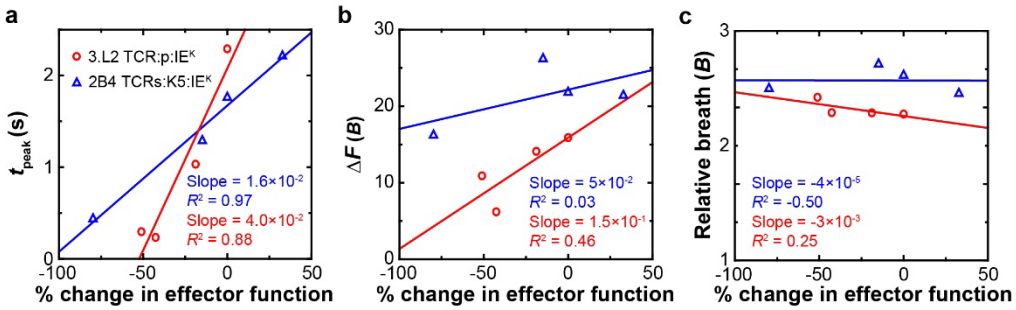

Supplementary Figure 8 | Correlation of metrics of TCR–pMHC-II bond lifetime *vs* force curves with T cell biological activity. a-c Dimensional metrices, $\boldsymbol{t_{peak}}$ (**a**), $\Delta\boldsymbol{F}$ (**b**) and relative breadth of catch-slip bond $\boldsymbol{B}$ (**c**) *vs* reciprocal % change (relative to WT) in T cell effector function, i.e., the peptide dose required for 3.L2 T cells to generate 40% B cell apoptosis ($1/EC_{40}$)[19] (*red*) or the area under the dose response curve (AUC) of 2B4 hybridoma IL-2 production[20] (*blue*) plots.

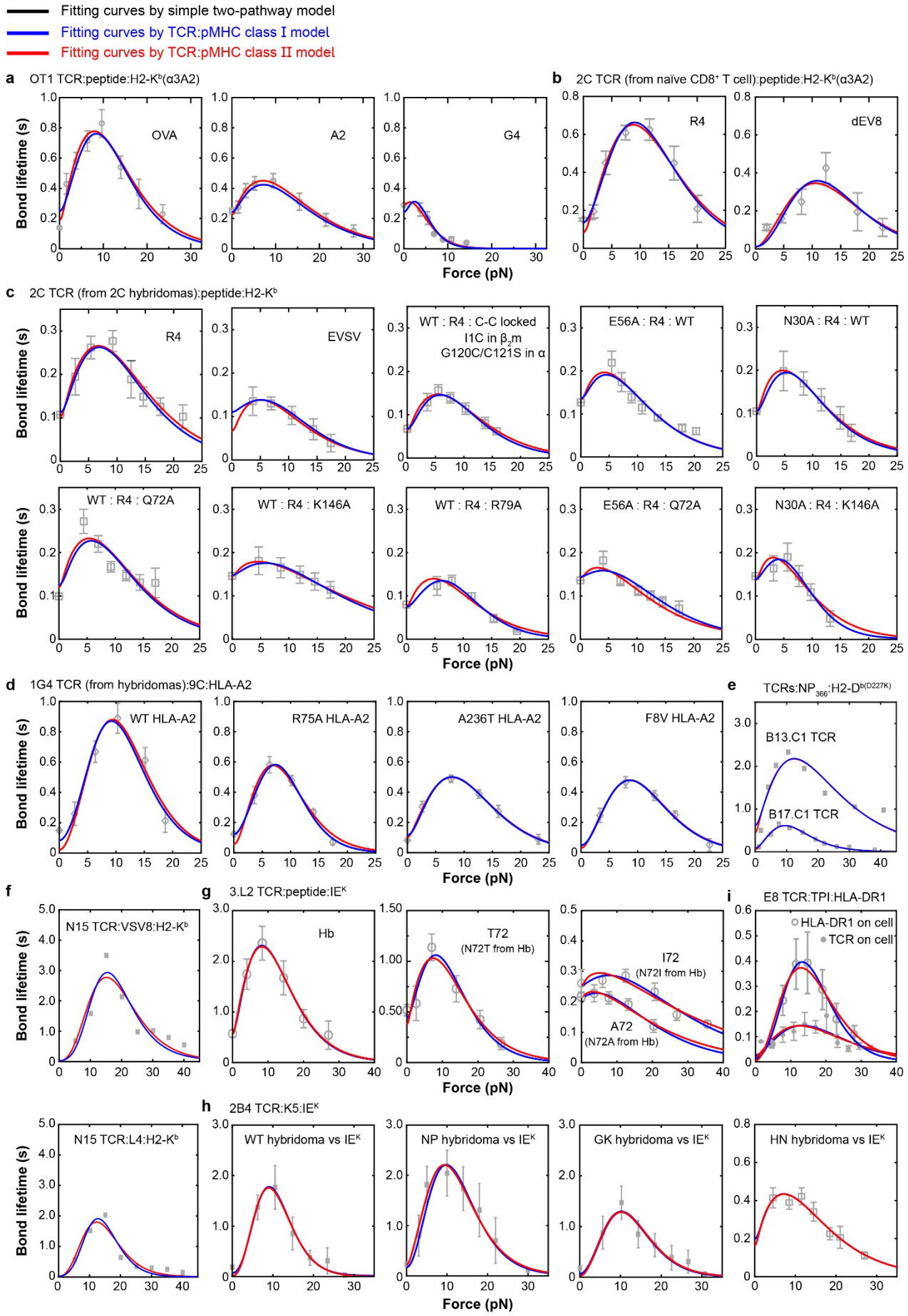
Fitting curves by simple two-pathway model
Fitting curves by TCR:pMHC class I model
Fitting curves by TCR:pMHC class II model
a OT1 TCR:peptide:H2-Kb(α3A2)
OVA
A2
G4
b 2C TCR (from naïve CD8+ T cell):peptide:H2-Kb(α3A2)
R4
dEV8
c 2C TCR (from 2C hybridomas):peptide:H2-Kb
R4
EVSV
WT : R4 : C-C locked
I1C in β2m
G120C/C121S in α
E56A : R4 : WT
N30A : R4 : WT
WT : R4 : Q72A
WT : R4 : K146A
WT : R4 : R79A
E56A : R4 : Q72A
N30A : R4 : K146A
d 1G4 TCR (from hybridomas):9C:HLA-A2
WT HLA-A2
R75A HLA-A2
A236T HLA-A2
F8V HLA-A2
e TCRs:NP366:H2-Db(D227K)
B13.C1 TCR
B17.C1 TCR
f
N15 TCR:VSV8:H2-Kb
g 3.L2 TCR:peptide:IEK
Hb
T72
(N72T from Hb)
I72
(N72I from Hb)
A72
(N72A from Hb)
i E8 TCR:TPI:HLA-DR1
HLA-DR1 on cell
TCR on cell
h 2B4 TCR:K5:IEK
N15 TCR:L4:H2-Kb
WT hybridoma vs IEK
NP hybridoma vs IEK
GK hybridoma vs IEK
HN hybridoma vs IEK
Bond lifetime (s)
Force (pN)

1462

1463 **Supplementary Figure 9 | Comparing fitting curves of class I and class II models to the same**
1464 **data. a-i** Fitting of theoretical $1/k(F)$ curves predicted by the class I (blue) or class II (*red*) model
1465 to experimental lifetime (*points*, mean ± sem) *vs* force data of TCR bonds with pMHC-I (**a-f**) or
1466 pMHC-II (**g-i**) ligands, as described below (partly presented in Supplementary Fig. 1, re-analyzed
1467 from Refs. [4,15,16,17,18,21,22,23]): OT1 (**a**) or 2C (**b**) TCR expressed on $CD8^+$ naïve T cells interacting
1468 with indicated p:H2-K^bα3A2; WT or mutant 2C (**c**) or 1G4 (**d**) TCR expressed on hybridomas
1469 interacting with indicated peptides presented by WT or MT H2-K^b or HLA-A2. B13.C1 and
1470 B17.C1 TCR expressed on hybridomas interacted with NP_{366} bound to the D227K MT of H-$2D^b$
1471 to prevent CD8 binding (**e**). Soluble N15 TCRαβ interacting with indicated p:H2-K^b (**f**). 3.L2
1472 TCR expressed on $CD4^-CD8^+$ T cells interacting with indicated p:I-E^k (**g**). WT or MT 2B4 TCRs
1473 expressed on $CD4^-$ hybridomas interacting with K5:I-E^k (**h**). E8 TCR expressed on $CD4^-$ Jurkat
1474 cells interacting with TPI:HLA-DR1 (**i**). See Supplementary Table 3 and 6 for lists of the
1475 interacting molecules.
1476
1477

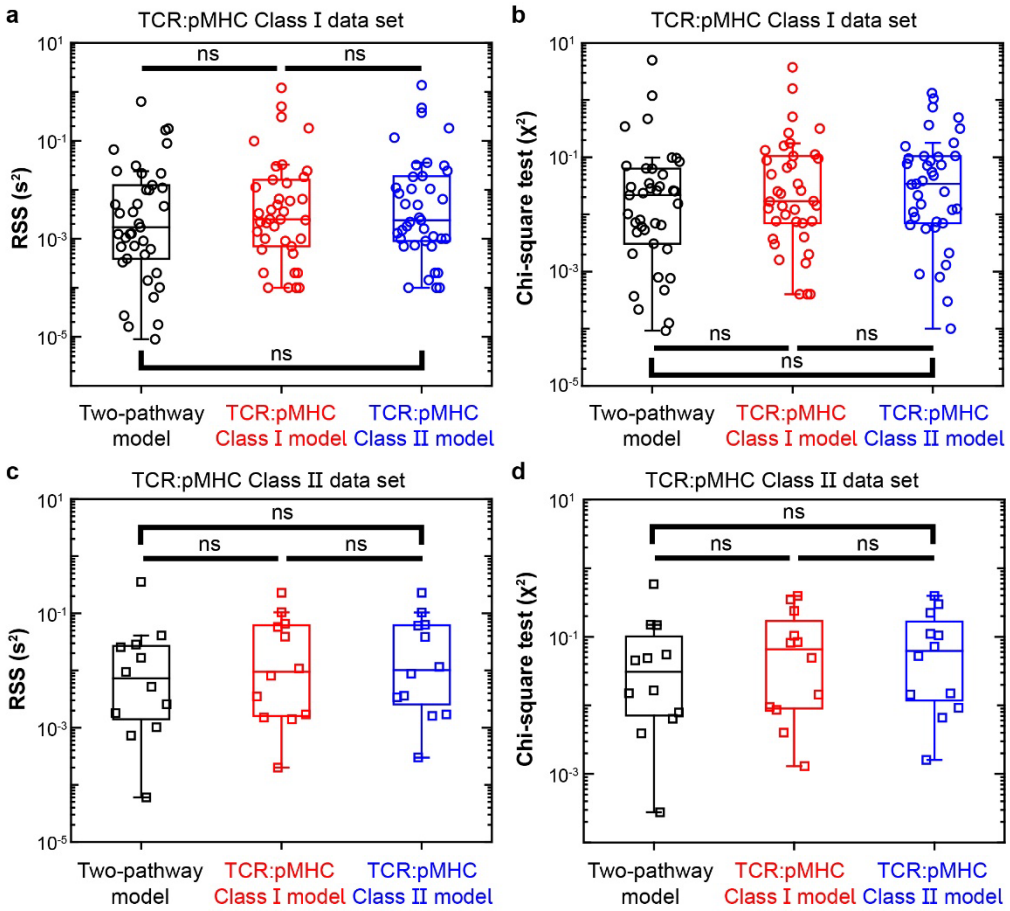

Supplementary Figure 10 | Comparison of goodness-of-fit measures among the class I and II models and the two-pathway model to class I and class II data. a-b Residual sum of squares (RSS, **a**) and Chi-square values (χ^2, **b**) obtained using three models – two-pathway model (*black*), TCR–pMHC-I model (red), and TCR–pMHC-II model (*blue*) – to fit pMHC-I data. **c-d** Residual sum of squares (RSS, **c**) and Chi-square values (χ^2, **d**) obtained using three models – two-pathway model (*black*), TCR-pMHC-I model (red), and TCR-pMHC-II model (*blue*) – to fit pMHC-II data. Individual scattered points, median, 25%, 75% and 5%, 95% whiskers are shown. Statistical tests were done using paired *t* test with two-tail.

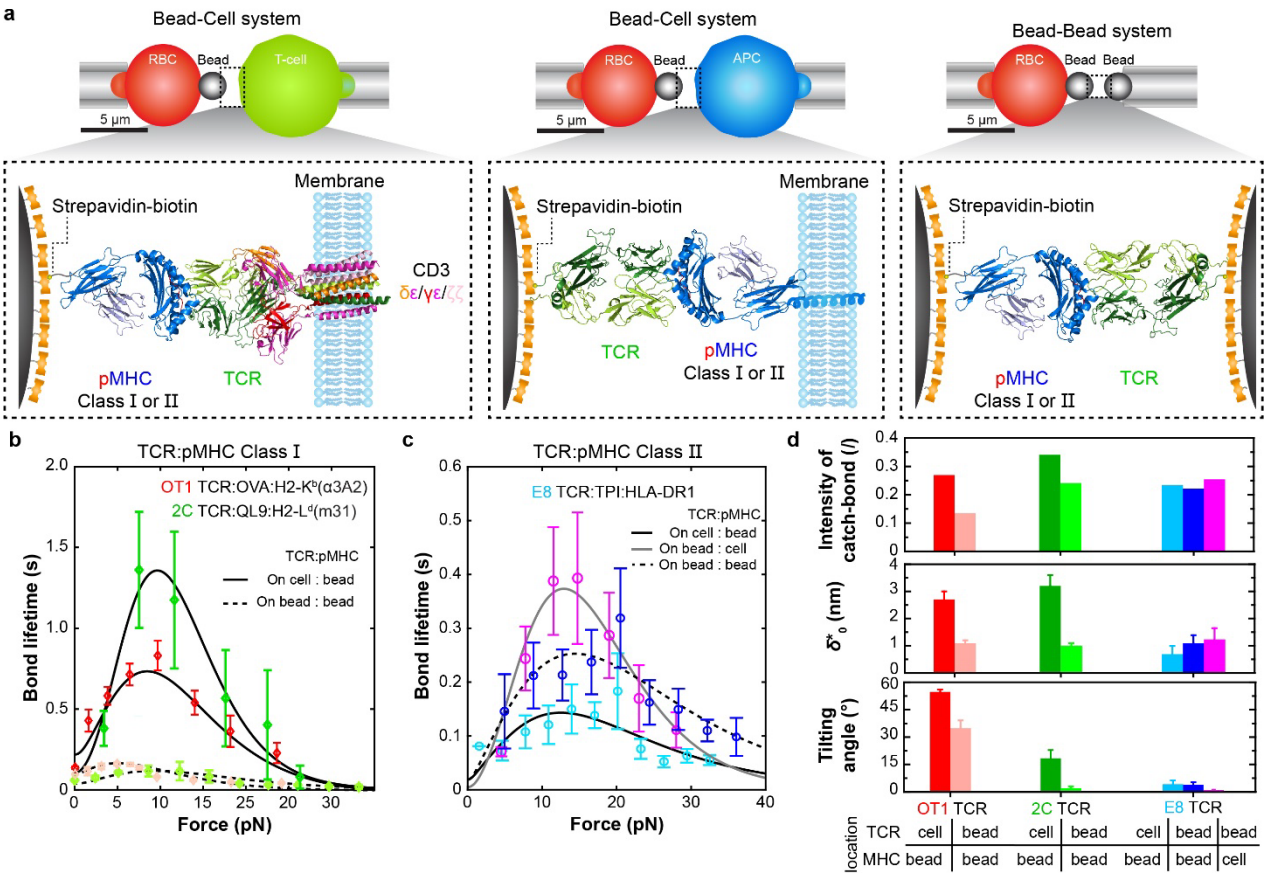

Supplementary Figure 11 | Comparison of pMHC interactions with cell surface and soluble TCRs. a Schematics of three biomembrane force probe (BFP) experiments. The BFP were set up in three configurations (*upper row*) depending on the molecular systems tested (*lower row*). In the first configuration (*left column*), the pMHC was coated on a BFP bead (*left*) and the TCR-CD3 complex was expressed on a T cell (*right*). In the second configuration (*middle column*), the purified TCRαβ was coated on a BFP bead (*left*) and the pMHC was expressed on an APC (*right*). In the third configuration, the pMHC was coated on a BFP bead (*left*) and the purified TCRαβ was coated on a glass bead (*right*). The TCR–pMHC complexes were drawn based on the cryoEM structure with CD3 (6JXR) or crystal structure without CD3 (2CKB). **b-c** Fitting of theoretical $1/k(F)$ (*curves*) to experimental bond lifetime *vs* force data (*points*, mean ± sem) of the following interactions: OT1 or 2C TCR respectively expressed on $CD8^+$ naïve T cells (*red*) or $CD8^-$ hybridomas (*green*) or coated on beads (*pink* for OT1 and *yellow-green* for 2C) respectively interacting with OVA:H2-K^bα3A2 or QL9:H2-L^d(m3), both MHC class I molecules[24] (**b**) or of

1502 E8 TCR expressed on CD8$^-$ Jurkat (*sky-blue*) or coated on beads interacting with TPI:HLA-DR1,

1503 a MHC class II, coated on beads (*blue*) or expressed on THP-1 cells (*purple*)[22] (**c**). **d** Comparison

1504 of the catch bond intensity (*top*) and best-fit parameters $\boldsymbol{\delta_0^*}$ (*middle*) and $\boldsymbol{\theta}$ (*bottom*) evaluated

1505 from data in (**b**) and (**c**) of TCR–pMHC interactions measured using the three configurations

1506 depicted in (**a**). All error bars indicate fitting error. See Supplementary Table 3 and 6 for lists of

1507 the interacting molecules.

1508
1509

1510 **Supplementary Table 1 | Summary of model constants**

Parameters	Symbol	Value	Reference
Elastic modulus of the folded globular domain	E_{d}	100 pN	[2]
Average contour length	l_{c}	0.36 nm	[6,7,8]
Persistence length	l_{p}	0.39 nm	[6,7,8]
Elastic modulus of polypeptides	E_{p}	50 μN	[8]
Force-free extension of bound state	$d_{\mathrm{N,c}}$	10.9 – 12.7 nm	[‡]
Force-free length of TCRαβ constant domain	$d_{\mathrm{C\alpha\beta,c}}$	3.3 – 3.8 nm	[‡]
Angle shown in Fig. 2b and Supplementary Figure 4	φ	5 – 23.5 °	[‡]

1511 [‡]Detailed values for each of the OT1, 2C, 1G4, N15, B13.C1, B17.C1, B17.R1, B17.R2, 3.L2, E8, and 2B4 TCR
1512 structures are described in Supplementary Model Derivations.
1513
1514

1515 **Supplementary Table 2 | An example of finding the best-fit parameters for OT1 TCR–**

1516 **OVA:H2-K^{b}a3A2 bond**

n^*	$d_{\alpha 3}$ (nm)[‡]	θ (°)[‡]	$n^* l_c$ (nm)	δ_1 (nm)	δ_0 (nm)[‡]	k_0 (s^{-1})[‡]
1	5.2	61.9	0.36	-0.8	0.7	4.84
2	5.1	59.7	0.72	-0.5	1.1	4.66
3	4.9	57.3	1.08	0.0	1.4	4.54
4	4.7	55.4	1.44	0.2	1.7	4.44
5	4.5	54.1	1.80	0.6	1.9	4.34
6	4.4	53.5	2.16	1.0	2.1	4.26
7	4.3	53.4	2.52	1.3	2.2	4.20
8	4.2	53.6	2.88	1.7	2.4	4.14
9	4.1	54.1	3.24	2.0	2.5	4.09
10	4.1	54.8	3.60	2.4	2.6	4.04
11	**4.0**	**55.5**	**3.96**	**2.7**	**2.7**	**4.00**
12	4.0	56.4	4.32	3.1	2.8	3.73
13	1.8	25.8	4.68	3.5	3.9	3.76
14	2.4	70.5	5.04	3.9	3.3	3.87

1517 [‡]The fitting parameters derived from model (see Supplementary Model Derivation, Section A.3).

1518 **Supplementary Table 3 | TCR–pMHC-I bond summary and their best-fitting parameters**

TCR	peptide	MHC class I	n^*	$d_{\alpha3}$ ± error (nm)	θ ± error (°)	δ_0 ± error (nm)	k_0 ± error (s^{-1})	$\Delta G_0^{\ddagger}$ ± error (k_BT)
OT1†	OVA	H2-K^b (α3A2)	11	4.0 ± 0.2	55.5 ± 1.5	2.7 ± 0.3	4.0 ± 2.3	12.4 ± 0.5
OT1‡	OVA	H2-K^b (α3A2)	6	4.0 ± 0.2	34.9 ± 4.3	1.1 ± 0.1	9.6 ± 1.6	11.6 ± 0.1
OT1†	A2	H2-K^b (α3A2)	7	3.9 ± 0.2	44.0 ± 3.1	1.1 ± 0.1	4.1± 1.0	12.4 ± 0.2
OT1†	G4	H2-K^b (α3A2)	9	5.0 ± 0.4	35.2 ± 2.2	2.7 ± 0.4	4.2 ± 1.1	12.4 ± 0.2
OT1†	E1	H2-K^b (α3A2)	0	0.0 ± 0.0	1.0 ± 1.2	0.9 ± 0.1	2.4 ± 0.2	13.0 ± 0.1
OT1†	R4	H2-K^b (α3A2)	0	0.0 ± 0.0	0.0 ± 0.9	1.0 ± 0.3	2.0 ± 0.3	13.1 ± 0.1
OT1*	OVA	H2-K^b (α3A2)	6	1.6 ± 0.2	17.5 ± 2.9	1.6 ± 0.2	3.3 ± 0.6	12.6 ± 0.2
OT1*	OVA	H2-K^b	11	1.9 ± 0.3	26.6 ± 4.9	3.1 ± 0.3	3.6 ± 0.3	12.5 ± 0.1
OT1*	Q4H7	H2-K^b (α3A2)	1	0.0 ± 0.0	0.0 ± 0.2	0.4 ± 0.2	4.3 ± 0.8	12.4 ± 0.2
OT1*	Q4R7	H2-K^b (α3A2)	1	0.0 ± 0.0	0.0 ± 0.2	0.4 ± 0.1	3.8 ± 0.8	12.4 ± 0.2
2C†	R4	H2-K^b (α3A2)	7	2.5 ± 0.5	19.3 ± 1.3	2.3 ± 0.2	7.4 ± 4.8	11.8 ± 0.5
2C†	dEV8	H2-K^b (α3A2)	3	2.6 ± 0.5	13.3 ± 1.7	2.0 ± 0.2	75.6 ± 18.7	9.5 ± 0.2
2C†	L4	H2-K^b (α3A2)	0	0.0 ± 0.0	0.0 ± 0.2	0.4 ± 0.1	3.8 ± 1.5	12.5 ± 0.3
2C*	R4	H2-K^b (α3A2)	6	0.9 ± 0.1	7.3 ± 1.6	1.3 ± 0.2	3.7 ± 0.3	12.5 ± 0.1
2C*	R4	H2-K^b	12	1.7 ± 0.3	21.8 ± 2.5	2.8 ± 0.3	5.5 ± 0.6	12.1 ± 0.1
2C	R4	H2-K^b	7	4.0 ± 0.3	28.2 ± 2.0	1.5 ± 0.4	8.9 ± 4.7	11.6 ± 0.4
2C	R4	H2-K^b C-C locked‡	7	4.1 ± 0.2	24.9 ± 2.0	1.6 ± 0.3	14.8 ± 4.4	11.1 ± 0.3
2C	EVSV	H2-K^b	2	0.4 ± 0.2	6.4 ± 1.8	0.9 ± 0.3	9.0 ± 2.8	11.6 ± 0.3
2C	L4	H2-K^b	1	0.1 ± 0.1	2.1 ± 1.5	0.6 ± 0.1	6.8 ± 1.3	11.9 ± 0.1
2C E56A	R4	H2-K^b	9	4.1 ± 0.5	20.7 ± 3.3	1.2 ± 0.2	7.4 ± 3.5	11.8 ± 0.4
2C N30A	R4	H2-K^b	7	4.3 ± 0.1	23.6 ± 2.8	1.4 ± 0.4	9.5 ± 3.6	11.6 ± 0.3
2C	R4	H2-K^b Q72A	7	4.2 ± 0.4	25.3 ± 2.3	1.3 ± 0.3	8.0 ± 4.5	11.7 ± 0.4
2C	R4	H2-K^b K146A	4	0.4 ± 0.2	4.7 ± 1.0	1.1 ± 0.2	6.7 ± 1.3	11.9 ± 0.1
2C	R4	H2-K^b R79A	4	0.6 ± 0.3	9.1 ± 0.5	2.3 ± 0.6	13.2 ± 6.3	11.2 ± 0.4
2C E56A	R4	H2-K^b Q72A	4	0.4 ± 0.3	5.6 ± 1.2	1.1 ± 0.3	6.9 ± 2.7	11.9 ± 0.3
2C N30A	R4	H2-K^b K146A	2	0.4 ± 0.2	6.8 ± 0.9	1.5 ± 0.4	7.2 ± 3.8	11.8 ± 0.4
2C†	QL9	H2-L^d (m31)	6	2.5 ± 0.7	18.4 ± 4.5	3.2 ± 0.4	9.5 ± 7.9	11.6 ± 0.6
2C‡	QL9	H2-L^d (m31)	3	2.0 ± 0.6	2.0 ± 0.9	1.0 ± 0.1	26.9 ± 7.0	10.5 ± 0.2
1G4	9C	HLA-A2	4	1.8 ± 0.7	10.1 ± 0.5	2.7 ± 0.4	13.7 ± 3.5	11.2 ± 0.2

1G4	9C	HLA-A2 R75A	6	1.4 ± 0.2	9.4 ± 0.4	3.7 ± 0.3	8.1 ± 8.0	11.0 ± 0.7
1G4	9C	HLA-A2 A236T	5	4.2 ± 0.2	29.4 ± 2.6	1.8 ± 0.3	8.6 ± 2.0	11.7 ± 0.2
1G4	9C	HLA-A2 F8V	4	4.1 ± 0.4	26.8 ± 1.4	2.0 ± 0.4	19.7 ± 4.5	10.8 ± 0.2
N15¶	VSV8	H2-K^b	9	3.2 ± 0.3	32.0 ± 4.6	4.5 ± 0.5	32.9 ± 10.0	10.3 ± 0.2
N15¶	L4	H2-K^b	5	1.8 ± 0.3	13.7 ± 1.5	4.3 ± 0.5	48.1 ± 21.1	9.9 ± 0.4
N15¶	SEV9	H2-K^b	0	0.0 ± 0.0	0.0 ± 0.0	0.6 ± 0.1	0.6 ± 0.1	14.3 ± 0.2
B13. C1#	NP$_{366}$	H-2D^b (D227K)	8	4.2 ± 0.4	40.0 ± 6.2	1.4 ± 0.3	1.6 ± 0.8	13.3 ± 0.4
B17. C1#	NP$_{366}$	H-2D^b (D227K)	6	4.2 ± 00.5	33.2 ± 4.1	2.2 ± 0.5	11.3 ± 6.6	11.4 ± 0.2
B17. R1#	NP$_{366}$	H-2D^b (D227K)	0	0.0 ± 0.0	0.0 ± 0.0	0.6 ± 0.2	0.3 ± 0.1	14.9 ± 0.3
B17. R2#	NP$_{366}$	H-2D^b (D227K)	3	0.4 ± 0.3	0.4 ± 0.2	1.2 ± 0.2	0.4 ± 0.1	14.9 ± 0.2

⁋Purified recombinant TCRs coated on beads were used in BFP measurement.
*OT1 or 2C TCR expressed on CD4$^+$CD8$^+$ thymocytes were used.
†OT1 or 2C TCR expressed on naïve T cells from transgenic mice were used. In other cases, 2C or 1G4 TCR expressed on 58$\alpha^{-1}\beta^{-1}$ hybridomas and J76 Jurkat cells were used.
¶Soluble mouse N15 TCRαβ was used to measure bond lifetime in optical tweezers[16].
#Mouse TRBV TCRs (B13.C1 and B17.C1 with canonical docking orientation and B17.R1 and B17.R2 with reverse docking orientation) expressed on 5KC hybridomas interacted with NP$_{366}$ bound to the D227K MT of H-2D^b to prevent CD8 binding[18]
‡I1C mutation in β2m domain, G120C and C121S mutations in α domain (H2-K^b) were introduced.
Note that the best-fit parameters were chosen by the procedure shown in Supplementary Table 2 or determined as the parameter set with the closest δ_l value to δ_0^* as well as the smallest RSS. All errors are standard error of mean after optimizing the best-fit parameters. All values were rounded to one decimal place.

1532 **Supplementary Table 4 | Two-pathway model summary and their best-fitting parameters**

TCR-pMHC class I

TCR	peptide	MHC class Ⅰ	$k_{0,p1}$ (s^{-1})	$k_{0,p1}$ error	$\delta^*_{0,p1}$ (nm)	$\delta^*_{0,p1}$ error	$k_{0,p2}$ (s^{-1})	$k_{0,p2}$ error	$\delta^*_{0,p2}$ (nm)	$\delta^*_{0,p2}$ error
OT1†	OVA	H2-Kb(a3A2)	3.99	2.7	-1.36	1.13	0.41	0.49	0.43	0.31
OT1‡	OVA	H2-Kb(a3A2)	7.77	4.54	-1.81	2.16	3.29	2.38	0.44	0.28
OT1†	A2	H2-Kb(a3A2)	3.36	0.57	-1.01	0.41	0.86	0.36	0.35	0.1
OT1†	G4	H2-Kb(a3A2)	1.99	3.05	-3.13	37.34	1.47	3.02	1.04	1.17
OT1†	E1	H2-Kb(a3A2)	0.39	0.41	-2.32	20.95	2.01	17.59	0.95	5.24
OT1†	R4	H2-Kb(a3A2)	N.A	N.A	N.A	N.A	2	0.39	0.91	0.36
OT1*	OVA	H2-Kb(a3A2)	3.02	1.56	-0.84	0.71	0.35	0.44	0.33	0.24
OT1*	OVA	H2-Kb	2.47	0.88	-0.52	0.3	0.05	0.09	0.67	0.35
OT1*	Q4H7	H2-Kb(a3A2)	N.A	N.A	N.A	N.A	4.09	0.53	0.13	0.07
OT1*	Q4R7	H2-Kb(a3A2)	N.A	N.A	N.A	N.A	3.44	0.25	0.16	0.03
2C†	R4	H2-Kb(a3A2)	6.09	3.45	-1.13	0.71	0.28	0.39	0.56	0.35
2C†	dEV8	H2-Kb(a3A2)	15.44	16.59	-0.81	0.73	0.06	0.25	0.99	0.93
2C†	L4	H2-Kb(a3A2)	N.A	N.A	N.A	N.A	3.85	0.45	0.36	0.08
2C*	R4	H2-Kb(a3A2)	3.37	0.65	-0.26	0.31	0.13	0.39	0.75	0.58
2C*	R4	H2-Kb	5.44	5.35	-1.07	1.19	0.67	0.94	0.25	0.27
2C	R4	H2-Kb	8.04	3.69	-1.43	0.94	1.46	1.04	0.4	0.2
2C	R4	H2-Kb(C-C locked ⁑)	12.63	3.35	-1.43	0.64	2.48	1.36	0.49	0.18
2C	EVSV	H2-Kb	7.13	7.6	-0.08	2.73	0.28	6.44	1.02	5.08
2C	L4	H2-Kb	5.62	6.83	0	4.68	0.49	16.21	0.9	7.09
2C E56A	R4	H2-Kb	5.27	2.9e4	-12.7	23.38	2.79	0.9	0.41	0.13
2C N30A	R4	H2-Kb	7.91	4.32	-1.21	1.42	1.63	2.4	0.56	0.46
2C	R4	H2-Kb Q72A	7.52	1e4	-14.21	59.17	2.83	1.49	0.29	0.2
2C	R4	H2-Kb K146A	3.02	1.63	-1.21	1.35	3.83	1.57	0.2	0.11
2C	R4	H2-Kb R79A	12.37	2.24	-0.48	0.26	0.3	0.52	1.12	0.47
2C E56A	R4	H2-Kb Q72A	3.2	5e3	-15	69.15	4.26	1.13	0.29	0.1
2C N30A	R4	H2-Kb K146A	6.76	2.61	-0.39	1.06	0.26	1.57	1.37	2.12
2C†	QL9	H2-Ld (m31)	14.16	22	-2.24	1.3	0.19	0.17	0.53	0.25
2C‡	QL9	H2-Ld (m31)	15.91	5.12	-0.82	0.53	2.02	1.73	0.47	0.18
1G4	9C	HLA-A2	6.25	8.43	-0.98	1.23	0.05	0.27	0.97	1.4
1G4	9C	HLA-A2 R75A	7.3	7.73	-1.36	1.3	0.19	0.48	0.93	0.84
1G4	9C	HLA-A2 A236T	8.6	16.26	-2.01	3.81	0.82	1.29	0.4	0.46
1G4	9C	HLA-A2 F8V	7.72	33.1	-0.92	4.07	0.18	2.08	0.8	3.02
N15¶	VSV8	H2-Kb	33.35	222.82	-1.8	2.86	0.05	0.1	0.43	0.34
N15¶	L4	H2-Kb	7.96	20.51	-1.12	1.22	0.01	0.04	0.98	0.78
N15¶	SEV9	H2-Kb	N.A	N.A	N.A	N.A	0.64	0.47	0.58	0.38
B13.C1#	NP366	H-2Db (D227K)	4.29	6.09	-2.54	1.62	0.32	0.09	0.14	0.06
B17.C1#	NP366	H-2Db (D227K)	14.64	10.72	-1.93	0.66	0.54	0.18	0.41	0.08

B17.R1#	NP366	H-2Db (D227K)	N.A	N.A	N.A	N.A	0.35	0.14	0.61	0.34
B17.R2#	NP366	H-2Db (D227K)	0.29	0.1	0	0.75	0.02	0.14	0.78	1.16

TCR-pMHC class II

TCR	peptide	MHC class II	$k_{0,p1}$ (s^{-1})	$k_{0,p1}$ error	$\delta^*_{0,p1}$ (nm)	$\delta^*_{0,p1}$ error	$k_{0,p2}$ (s^{-1})	$k_{0,p2}$ error	$\delta^*_{0,p2}$ (nm)	$\delta^*_{0,p2}$ error
3.L2	Hb	I-E^k	1.54	1.03	-1.57	0.99	0.16	0.11	0.39	0.17
3.L2	T72	I-E^k	2.11	2.22	-1.01	2	0.24	0.8	0.49	0.8
3.L2	A72	I-E^k	4.25	7.93	-0.08	1.73	0.32	8.55	0.58	4.46
3.L2	I72	I-E^k	2.77	4.91	-0.24	1.15	1.13	5.13	0.23	0.54
E8	TPI	HLA-DR1	17.54	12.47	-0.39	0.45	0.29	1.06	0.58	0.53
E8⁋	TPI	HLA-DR1	10.13	11.77	-0.42	0.73	0.44	1.53	0.38	0.44
E8	TPI	HLA-DR1	53.09	70.85	-1.5	0.78	0.5	0.44	0.44	0.18
2B4 NP	K5	I-Ek	4.26	8.53	-2.12	2.11	0.14	0.13	0.45	0.26
2B4 WT	K5	I-Ek	5.99	10.17	-1.64	1.27	0.06	0.07	0.81	0.33
2B4 GK	K5	I-Ek	9.53	22.44	-1.88	1.89	0.18	0.16	0.51	0.23
2B4 HN	K5	I-Ek	2.53	1.57	-0.29	1.28	0.35	1.67	0.51	0.8

N.A indicates not applicable.

⁋Purified recombinant TCRs coated on beads were used in BFP measurement.

*OT1 or 2C TCR expressed on $CD4^+CD8^+$ thymocytes were used.

†OT1 or 2C TCR expressed on naïve T cells from transgenic mice were used. In other cases, 2C or 1G4 TCR expressed on $58\alpha^{-1}\beta^{-1}$ hybridomas and J76 Jurkat cells were used.

¶Soluble mouse N15 TCRαβ was used to measure bond lifetime in optical tweezers[16].

#Mouse TRBV TCRs (B13.C1 and B17.C1 with canonical docking orientation and B17.R1 and B17.R2 with reverse docking orientation) expressed on 5KC hybridomas interacted with NP_{366} bound to the D227K MT of H-$2D^b$ to prevent CD8 binding[18]

‡I1C mutation in β2m domain, G120C and C121S mutations in α domain (H2-K^b) were introduced.

Note that the best-fit parameters were extracted from equation (4) (two-pathway model) in the main text. Fitting errors are indicated.

1546 **Supplementary Table 5 | An example of finding the best-fit parameters for the 3.L2 TCR–**

1547 **Hb:I-E^k bond**

n^*_{MHC}†	$d_{\mathrm{B.I}}$ (nm)‡	θ (°)‡	$n^* l_c$ (nm)	δ_I (nm)	δ_0 (nm)‡	k_0 (s^{-1})‡
1	8.9	0.0	0.4	0.6	0.7	2.0
2	8.8	0.0	0.7	0.9	1.2	1.9
3	8.6	0.5	1.1	1.3	1.5	1.8
4	**7.9**	**3.1**	**1.4**	**1.6**	**1.6**	**1.8**
5	7.9	2.6	1.8	2.0	1.7	1.7
6	7.8	2.1	2.2	2.4	1.9	1.7
7	8.0	1.5	2.5	2.7	2.1	1.6
8	7.8	0.6	2.9	3.1	2.2	1.6

1548 †n^* can be estimated from n^*_{pMHC}.

1549 ‡ See Supplementary Model Derivations, Section B.

1550

1551 **Supplementary Table 6 | TCR–pMHC-II bond summary and their best-fit parameters**

TCR	peptide	MHC class II	n^*	$d_{B.I}$ ± error (nm)	θ ± error (°)	δ_0 ± error (nm)	k_0 ± error (s^{-1})	$\Delta G_0^{\ddagger}$ ± error (k_BT)
3.L2	Hb	I-E^k	4	8.0 ± 0.6	3.2 ± 0.6	1.6 ± 0.5	1.8 ± 0.3	13.2 ± 0.2
3.L2	T72	I-E^k	3	8.7 ± 0.1	0.1 ± 0.1	1.2 ± 0.3	2.6 ± 0.6	12.9 ± 0.3
3.L2	A72	I-E^k	2	9.3 ± 0.2	0.0 ± 0.3	0.2 ± 0.0	4.7 ± 0.5	12.3 ± 0.1
3.L2	I72	I-E^k	1	9.1 ± 0.1	0.0 ± 0.3	0.1 ± 0.0	3.9 ± 0.6	12.4 ± 0.2
E8	TPI	HLA-DR1	2	8.6 ± 0.1	4.1 ± 0.4	0.7 ± 0.3	78.3 ± 2.7	9.5 ± 0.1
E8[P]	TPI	HLA-DR1	3	8.5 ± 0.1	4.0 ± 0.5	1.1 ± 0.3	41.4 ± 9.4	10.1 ± 0.2
E8*	TPI	HLA-DR1	4	8.8 ± 0.2	1.0 ± 0.3	1.2 ± 0.4	131.7 ± 40.5	8.9 ± 0.3
2B4 (NP)	K5	I-E^k	6	7.9 ± 0.3	7.3 ± 1.3	2.0 ± 0.2	4.5 ± 2.4	12.3 ± 0.4
2B4 (WT)	K5	I-E^k	4	8.8 ± 0.3	2.3 ± 0.7	1.8 ± 0.4	64.0 ± 9.1	9.7 ± 0.1
2B4 (GK)	K5	I-E^k	3	8.9 ± 0.2	1.9 ± 1.2	1.4 ± 0.5	40.1 ± 9.8	10.1 ± 0.2
2B4 (HN)	K5	I-E^k	2	8.9 ± 0.2	0.3 ± 0.1	0.5 ± 0.2	6.1 ± 0.8	12.0 ± 0.1
2B4 (NH)	K5	I-E^k	0	0.0 ± 0.0	0.0 ± 0.0	0.3 ± 0.1	2.6 ± 1.1	12.9 ± 0.1

1552 [P]The recombinant TCR coated to the bead was tested against pMHC on the BFP bead.

1553 *The recombinant TCR coated to the BFP bead was tested against pMHC expressed on a THP-1 cell.
1554 Note that the best-fit parameters were chosen using the procedure shown in Supplementary Table 5 or
1555 determined as the parameter set with the $\delta_z(n^*)$ value closest to δ_0^* as well as the smallest RSS. All errors
1556 are standard error of mean after optimizing the best-fit parameters. All values were rounded to one decimal
1557 place.
1558

Supplementary References

1. Smith, S. B., Finzi, L. & Bustamante, C. Direct mechanical measurements of the elasticity of single DNA molecules by using magnetic beads. *Science* **258**, 1122-1126, (1992).
2 Guo, S., Tang, Q., Yao, M., You, H., Le, S., Chen, H. & Yan, J. Structural-elastic determination of the force-dependent transition rate of biomolecules. *Chem Sci* **9**, 5871-5882, (2018).
3 Rossjohn, J., Gras, S., Miles, J. J., Turner, S. J., Godfrey, D. I. & McCluskey, J. T cell antigen receptor recognition of antigen-presenting molecules. *Annual review of immunology* **33**, 169-200, (2015).
4 Wu, P., Zhang, T., Liu, B., Fei, P., Cui, L., Qin, R., Zhu, H., Yao, D., Martinez, R. J., Hu, W., An, C., Zhang, Y., Liu, J., Shi, J., Fan, J., Yin, W., Sun, J., Zhou, C., Zeng, X., Xu, C., Wang, J., Evavold, B. D., Zhu, C., Chen, W. & Lou, J. Mechano-regulation of Peptide-MHC Class I Conformations Determines TCR Antigen Recognition. *Mol Cell* **73**, 1015-1027 e1017, (2019).
5 Bouchiat, C., Wang, M. D., Allemand, J., Strick, T., Block, S. M. & Croquette, V. Estimating the persistence length of a worm-like chain molecule from force-extension measurements. *Biophysical journal* **76**, 409-413, (1999).
6 Gebhardt, J. C., Bornschlogl, T. & Rief, M. Full distance-resolved folding energy landscape of one single protein molecule. *Proceedings of the National Academy of Sciences of the United States of America* **107**, 2013-2018, (2010).
7 Seol, Y., Li, J., Nelson, P. C., Perkins, T. T. & Betterton, M. D. Elasticity of short DNA molecules: theory and experiment for contour lengths of 0.6-7 microm. *Biophysical journal* **93**, 4360-4373, (2007).
8 Choi, H. K., Min, D., Kang, H., Shon, M. J., Rah, S. H., Kim, H. C., Jeong, H., Choi, H. J., Bowie, J. U. & Yoon, T. Y. Watching helical membrane proteins fold reveals a common N-to-C-terminal folding pathway. *Science* **366**, 1150-1156, (2019).
9 Schuler, B., Lipman, E. A. & Eaton, W. A. Probing the free-energy surface for protein folding with single-molecule fluorescence spectroscopy. *Nature* **419**, 743-747, (2002).
10 Yang, W. Y. & Gruebele, M. Folding at the speed limit. *Nature* **423**, 193-197, (2003).
11 Kubelka, J., Hofrichter, J. & Eaton, W. A. The protein folding 'speed limit'. *Curr Opin Struct Biol* **14**, 76-88, (2004).
12 Chung, H. S., Louis, J. M. & Eaton, W. A. Experimental determination of upper bound for transition path times in protein folding from single-molecule photon-by-photon trajectories. *Proceedings of the National Academy of Sciences of the United States of America* **106**, 11837-11844, (2009).
13 Guo, S., Efremov, A. K. & Yan, J. Understanding the catch-bond kinetics of biomolecules on a one-dimensional energy landscape. *Communications Chemistry* **2**, 30, (2019).
14 Lapidus, L. J., Steinbach, P. J., Eaton, W. A., Szabo, A. & Hofrichter, J. Effects of Chain Stiffness on the Dynamics of Loop Formation in Polypeptides. Appendix: Testing a 1-Dimensional Diffusion Model for Peptide Dynamics. *J. Phys. Chem. B* **106**, 11628-11640, (2002).
15 Liu, B., Chen, W., Evavold, B. D. & Zhu, C. Accumulation of dynamic catch bonds between TCR and agonist peptide-MHC triggers T cell signaling. *Cell* **157**, 357-368, (2014).
16 Das, D. K., Feng, Y., Mallis, R. J., Li, X., Keskin, D. B., Hussey, R. E., Brady, S. K., Wang, J. H., Wagner, G., Reinherz, E. L. & Lang, M. J. Force-dependent transition in the T-cell receptor beta-subunit allosterically regulates peptide discrimination and pMHC bond lifetime. *Proceedings of the National Academy of Sciences of the United States of America* **112**, 1517-1522, (2015).
17 Hong, J., Ge, C., Jothikumar, P., Yuan, Z., Liu, B., Bai, K., Li, K., Rittase, W., Shinzawa, M., Zhang, Y., Palin, A., Love, P., Yu, X., Salaita, K., Evavold, B. D., Singer, A. & Zhu, C. A TCR

1608 mechanotransduction signaling loop induces negative selection in the thymus. *Nat Immunol* **19**,
1609 1379-1390, (2018).
1610 18 Zareie, P., Szeto, C., Farenc, C., Gunasinghe, S. D., Kolawole, E. M., Nguyen, A., Blyth, C.,
1611 Sng, X. Y. X., Li, J., Jones, C. M., Fulcher, A. J., Jacobs, J. R., Wei, Q., Wojciech, L., Petersen,
1612 J., Gascoigne, N. R. J., Evavold, B. D., Gaus, K., Gras, S., Rossjohn, J. & La Gruta, N. L.
1613 Canonical T cell receptor docking on peptide-MHC is essential for T cell signaling. *Science*
1614 **372**, (2021).
1615 19 Kersh, G. J. & Allen, P. M. Structural basis for T cell recognition of altered peptide ligands: a
1616 single T cell receptor can productively recognize a large continuum of related ligands. *J Exp*
1617 *Med* **184**, 1259-1268, (1996).
1618 20 Natarajan, A., Nadarajah, V., Felsovalyi, K., Wang, W., Jeyachandran, V. R., Wasson, R. A.,
1619 Cardozo, T., Bracken, C. & Krogsgaard, M. Structural Model of the Extracellular Assembly of
1620 the TCR-CD3 Complex. *Cell Rep* **14**, 2833-2845, (2016).
1621 21 Hong, J., Persaud, S. P., Horvath, S., Allen, P. M., Evavold, B. D. & Zhu, C. Force-regulated
1622 In situ TCR-peptide-bound MHC class II kinetics determine functions of CD4+ T cells. *Journal*
1623 *of immunology* **195**, 3557-3564, (2015).
1624 22 Rushdi, M. N., Pan, V., Li, K., Travaglino, S., Choi, H.-K., Hong, J., Griffitts, F., Agnihotri, P.,
1625 Mariuzza, R. A., Ke, Y. & Zhu, C. Cooperative binding of TCR and CD4 to pMHC enhances
1626 TCR sensitivity. *Nature Communications*, in press.
1627 23 Yuan, Z., Cong, P., Natarajan, Ge, C., Travaglino, S., Beesam, S., Grazette, D., Krogsgaard, M.
1628 & Zhu, C. Cooperative ectodomain interaction among TCRαβ, CD3γε, and CD3δε enhances
1629 TCR mechanotransduction. *bioRxiv*,
1630 https://www.biorxiv.org/content/10.1101/2022.1104.1114.488403v488401, (2022).
1631 24 Liu, B., Chen, W., Natarajan, K., Li, Z., Margulies, D. H. & Zhu, C. The cellular environment
1632 regulates in situ kinetics of T-cell receptor interaction with peptide major histocompatibility
1633 complex. *European journal of immunology* **45**, 2099-2110, (2015).
1634
1635
1636